Advances in Multiscale Methods with Applications in Optimization, Uncertainty Quantification and Biomechanics

Nan Hu

Submitted in Partial Fulfillment of the
Requirements for the Degree of
Doctor of Philosophy
in the Graduate School of Arts and Sciences

COLUMBIA UNIVERSITY

2016

ABSTRACT

Advances in Multiscale Methods with Applications in Optimization, Uncertainty Quantification and Biomechanics

Nan Hu

Advances in multiscale methods are presented from two perspectives which address the issue of computational complexity of optimizing and inverse analyzing nonlinear composite materials and structures at multiple scales. The optimization algorithm provides several solutions to meet the enormous computational challenge of optimizing nonlinear structures at multiple scales including: (i) enhanced sampling procedure that provides superior performance of the well-known ant colony optimization algorithm, (ii) a mapping-based meshing of a representative volume element that unlike unstructured meshing permits sensitivity analysis on coarse meshes, and (iii) a multilevel optimization procedure that takes advantage of possible weak coupling of certain scales. We demonstrate the proposed optimization procedure on elastic and inelastic laminated plates involving three scales. We also present an adaptive variant of the measure-theoretic approach (MTA) for stochastic characterization of micromechanical properties based on the observations of quantities of interest at the coarse (macro) scale. The salient features of the proposed nonintrusive stochastic inverse solver are: identification of a nearly optimal sampling domain using enhanced ant colony optimization algorithm for multiscale problems, incremental Latin-hypercube sampling method, adaptive discretization of the parameter and observation spaces, and adaptive selection of number of samples. A complete test data of the TORAY T700GC-12K-31E and epoxy #2510 material system from the NIAR report

is employed to characterize and validate the proposed adaptive nonintrusive stochastic inverse algorithm for various unnotched and open-hole laminates. Advances in Multiscale methods also provides us a unique tool to study and analyze human bones, which can be seen as a composite material, too. We used two multiscale approaches for fracture analysis of full scale femur. The two approaches are the reduced order homogenization (ROH) and the novel accelerated reduced order homogenization (AROH). The AROH is based on utilizing ROH calibrated to limited data as a training tool to calibrate a simpler, single-scale anisotropic damage model. For bone tissue orientation, we take advantage of so-called Wolff's law. The meso-phase properties are identified from the least square minimization of error between the overall cortical and trabecular bone properties and those predicted from the homogenization. The overall elastic and inelastic properties of the cortical and trabecular bone microstructure are derived from bone density that can be estimated from the Hounsfield units (HU). For model validation, we conduct ROH and AROH simulations of full scale finite element model of femur created from the QCT and compare the simulation results with available experimental data.

Contents

List of Figures

List of Tables

Acknowledgements

Foremost, I would like to thank my Ph.D. advisor Professor Jacob Fish who offered me a chance to study from and work with him for the past six years. He has been supportive since the very first day we met over Skype. It is his skillful guidance and encouragement, with which I was able to conduct my researches and finish this dissertation. Since English is my second language, I really appreciate the efforts he spent correcting my language in our papers over and over again.

I also want to express my sincere gratitude to my dissertation defense committee: Professor Jacob Fish, Professor Xiang-Dong Edward Guo, Professor Ioannis A. Kougioumtzoglou, Professor Steve WaiChing Sun and Professor Haim Waisman. Their suggestions, comments and remarks added great value to my papers and this dissertation.

My sincere thanks also goes to my friends at Columbia. Thank you to Zifeng Yuan, Zheng Yuan, Hao Sun, Yang Liu, Yang Jiao, Yongxiang Wang, Dongming Feng, Mahesh Bailakanavar, David Tal and Dimitrios Fafalis. They were always there when I needed a person to talk with or to turn to for help. Because of those listed and more that were not mentioned here, my life at Columbia was not only easier but more fascinating and memorable.

Last but not least, I want to thank my family. Thank you Yanhua Hu and Hongxia Zhao for bringing me to this wonderful world and support my life since then. I have also received a lot help from my aunts, uncles and cousins. Yan Ge, Hongyan Liu and Jing Shen, without you, I cannot finish this. Especially, I want to thank my grandparents: Deyi Hu and

Xiuying Ge who brought me up and gave me the most selfless love when my parents had to work when I was a child. I will always miss you both.

I would like to dedicate my thesis

to my beloved grandparents

Chapter 1
Introduction

Because of its tremendous features including durability, corrosion resistance and customization, this past decade has seen an accelerated deployment of composite materials in various fields, ranging from aerospace and automotive industry to energy sector and consumer goods. In fact, organs in human body could also be deemed as composite material. The most obvious case is human bones.

Methods for analyzing composite materials and structures ranging from mathematical homogenization methods pioneered by Babuska [1], Bensoussan [2] and Sanchez-Palencia [3], to computational variants of homogenization often coined as multiscale methods [4-9] are reaching a level of maturity. And while challenges remain primarily due to enormous computational complexity of repeatedly solving nonlinear representative volume element (RVE) at all quadrature points and at every load increment, recent developments of various reduced order homogenization methods [10] and their utilization in practice [11] have been very promising.

One of the key advantages offered by composites stems from their flexibility in tailoring composite microstructure to a problem at hand. This, however, poses added computational complexity that goes beyond analysis of these materials. The research on optimization of composite materials dates back to mid-seventies and has been accelerating since then [12-26]. Various optimization methods have been utilized for composites, including integer programming, genetic algorithms, ant colony optimization (ACO), artificial bee colony and Tabu search [12, 13, 17, 18, 24, 27-29]. In particular, the ACO

has been shown to perform extremely well in comparison to competing approaches [30] and has been utilized in various fields [31-38]. Hybrid optimization methods that blend several optimization algorithms, have been shown not only to overcome the shortcomings of their comprising components but also improve the overall solution efficiency [39-47].

In optimization of composite materials and structures, most of the research focused on optimization of a macrostructure (macroscale) as well as on stacking sequence (mesoscale) [12, 13, 16, 27, 48-54]. Optimization of microstructural and sub-microstructural scales has been rarely pursued due to tremendous computational complexity involved. The dramatic increase in computational complexity stems not only from consideration of more than two scales but also from necessity of continuous regeneration of the RVE geometry and its remeshing. Furthermore, sensitivity analysis requiring small changes in RVE geometry has been very challenging due to degree of randomness in unstructured meshing [55].

The focus of the present dissertation is partially on developing an enhanced ant colony optimization (EACO) algorithm and adapting it to composite materials and structures involving multiple scales. In the remaining of this section, we briefly review the relevant literature on the ant colony optimization (ACO), point out to current limitations and suggest remedies that conceptualize the proposed variant of the ACO, hereafter referred to as EACO.

To better understand composite materials, we also need to face the challenges they brought up. One of the challenges of composite materials is that, unlike conventional materials, composite materials usually demonstrates variety between different manufacturing batches. Such uncertainty would lead to various performance of the material.

Because of this reason, propagation of uncertainty from the scale of microconstituents in composites to the structural level has been a subject of considerable interest in academia, government and industry. Noteworthy are the stochastic finite element method (SFEM) [56-62], first order reliability method (FORM) [63], second order reliability method (SORM) in combination with Monte Carlo simulation (MC) [64, 65], perturbation methods [66, 67], homogenization methods combined with extended finite element method [68], and Mori-Tanaka Mean-Field theory [69].

Reliable stochastic inverse analysis of composite materials enables us to understand the composite material on a finer level. Various sources of uncertainty in composites are commonly categorized based on their spatial scale resolution [70]. A number of forward stochastic multiscale methods have been proposed. Stochastic multiscale finite element method (SFEM) in combination with MC has been employed to investigate microscopic stresses in fiber reinforced composites [71]. A probabilistic thermo-mechanical fatigue problem at multiple scales has been studied by Chamis [72]. Tootkaboni and Graham-Brady developed a multiscale spectral stochastic method for problems at multiple scales [73]. Chen and Soares analyzed laminated composite plates with spectral stochastic finite element method [74]. Fish and Wu [75, 76] developed an efficient uncertainty quantification solver for predicting elastic and inelastic response of composite materials using sparse grid collocation approach in combination with the reduced order homogenization [4, 5, 7, 77, 78].

The inverse multiscale problem is concerned with quantifying uncertainty at a fine (micro) scale, given variability of experimental data typically at the coarse (macro) scale. The goal is to infer the probability distribution of material constitutive model parameters

at the microscale from the macroscale level experiments by solving a stochastic inverse multiscale problem. There are several challenges associated with the stochastic inverse problem. First, the parameter space is multi-dimensional, while there are very few observations. So, the inverse problem is often ill-posed in the sense that the inverse solution of the deterministic model is set-valued. Secondly, forward multiscale simulation models are rather complex and expensive to evaluate. Sakata and colleagues studied the elastic properties of particle-reinforced composite material using MC [79]. A Bayesian statistical approach in combination with Markov Chain Monte Carlo (MCMC) method has been employed to calibrate microconstituent material properties from the coarse-scale experiments [80-82]. Microscale material constitutive parameters of a phenomenological multiscale model have been calibrated to hybrid experimental-digital database developed by high fidelity multiscale model in [83].

Herein this dissertation, we developed an adaptive nonintrusive inverse multiscale solver based on the measure-theoretic approach (MTA) recently developed by Estep and Butler [84, 85]. The MTA takes advantage of the fact that the likelihood function, which relates the model parameters to observations, is a deterministic map defined by the mathematical and computational model. This permits the MTA to compute the inverse problem with relative ease. On the other hand, in the Bayesian approach, the likelihood function is not deterministic and its construction may not be trivial [84, 85].

Since a single forward realization in multiscale problems might be extremely costly, the goal is to device a nonintrusive solver aimed at minimizing the number of realizations while controlling solution accuracy. The MTA has been enhanced with: (i) an incremental Latin-hypercube sampling method (iLHS) [86], (ii) adaptive selection of number of

samples, and (iii) identification of a nearly optimal sampling domain using the enhanced ant colony optimization algorithm for multiscale problems [87].

For model verification we will employ, the largest database for composites formed through the Advanced General Aviation Transport Experiments (AGATE), formed by NASA in 1995 and led by National Institute for Aviation Research (NIAR) at Wichita State University (WSU). This shared databases created using the AGATE process allowed a manufacturer to select a pre-approved composite material system to fabricate parts through a smaller subset of testing for a specific application [88]. The AGATE database uses a normal distribution to analyze the data.

Except for those man-made composite materials, bones in human bodies can naturally be seen as composite materials. Hence, the multiscale methods can also be adopted to analyze human's skeleton. Here, we focus our study on the human femurs.

The risk for hip fracture increases with age due to natural increase in fall rates [89] and decreased bone strength [90]. Osteoporosis, an age-related disease affecting bone density, is one of the major causes of loss of hip strength [91]. The cost of treating fractures associated with low bone mineral density (BMD) exceeds $50 billion per year in the United States and Europe. To gain an insight into the causes of bone fracture it is necessary to understand the remarkable hierarchical structure of bones spanning multiple spatial scales. Long bones consist of the cortical (compact) bone forming the outer core and trabecular (spongy or cancellous) bone filling inner space of the bone as shown in Figure 1. Cancellous bone is found in the Epiphyses of long bones. It is made of struts and plates of lamellar bone approximately 200 um in diameter and has a large surface area. Cortical bone is made of Haversian (Osteonal) bone, which are concentric circles of lamellar bone

approximately 200-300 μm in diameter. These Haversion bone circles are formed side by side and create the diaphyseal shaft of long bones. Cortical bone is dense with low porosity. It is stiffer than trabecular bone but is less ductile. For more details on various spatial scales in femur we refer to [92].

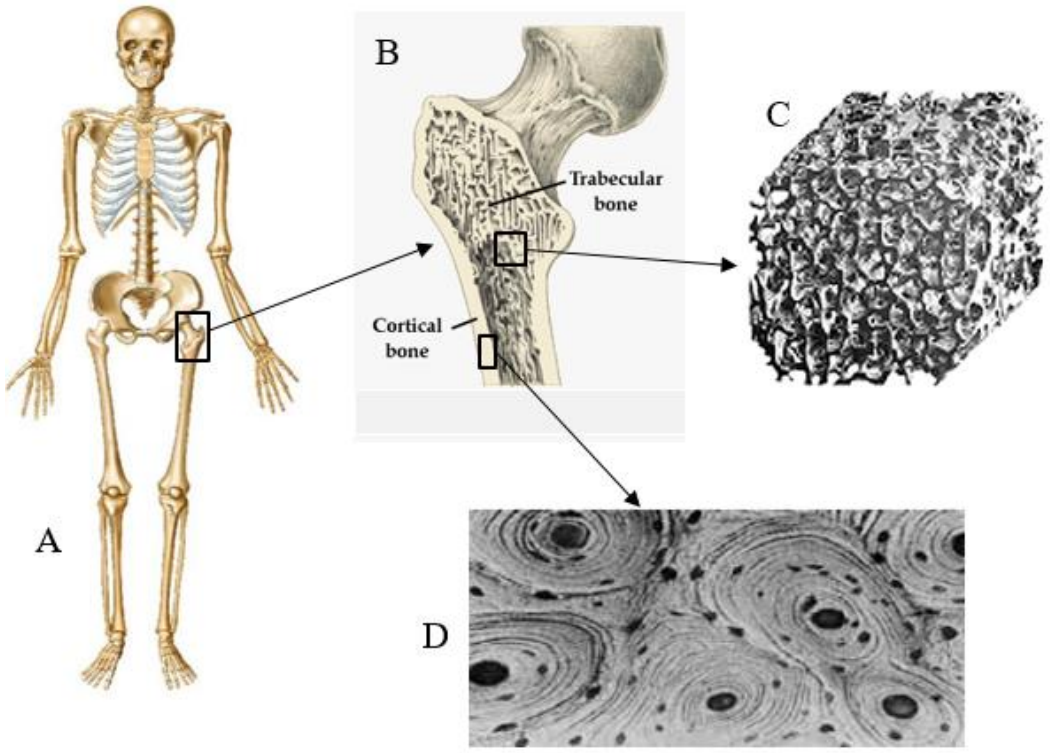

Figure 1 Schematic of the multiscale skeleton model, comprising of: (A) body-level skeleton model, (B) femur head and neck model, (C) micro-CT reconstruction of trabecular bone and (D) magnification of cortical osteonal structure of the cortical bone

In the present thesis we focus on the scale of trabecular and cortical bone (resolution of several hundred microns to several millimeters), which contains struts and plates of lamellar and osteons embedded in the interstitial lamella, respectively. Various analytical and computational models have been proposed to predict linear mechanical properties of a bone at this scale scales ranging from Mori–Tanaka to computational homogenization.

Mori–Tanaka scheme [92, 93] has been employed to predict overall elastic properties of cortical bone where the interstitial lamella being the matrix and the osteons with some resorption cavities being two inclusion phases. Patient-specific computational homogenization models of the human femur have been widely used to predict its linear elastic mechanical properties and response [94-96]. In [97], bone fracture was determined based on linear analysis when at least one solid element had exceeded a minimum principal strain of 1%.

Inelastic modeling femur is of great importance to predict mortality of femur fractures in aging populations. Noninvasive measurements of femur strength are not yet available clinically [98]. Current standard for clinical fracture risk is based on measurement areal bone mineral density (aBMD), which does not account for precise bone geometry [99]. The quantitative computed tomography (QCT) can account for the three-dimensional femur geometry and bone density distribution [100], but cannot resolve the details of trabecular and cortical bone microstructure.

Multiscale modeling of full scale femur fracture are practically nonexistent for variate of reason including lack of detailed patient-specific microstructural information and tremendous computational complexity involved. For linear problems, the unit cell representing trabecular or cortical bone has to be solved once, whereas for nonlinear problems, it has to be continuously solved at very load increment and each iteration at the femur (macro) scale. For instance, with typical one million full integration macro-elements at a femur level and 100 load increments with an average of 10 iterations per increment, a one-million degree-of-freedom nonlinear unit nonlinear cell problem representing trabecular or cortical bone microstructure has to be solved more than 10^{10} times!

This is why it is not surprising that femur fracture has been mostly modeled using single-scale phenomenological models employing either continuum damage, plasticity or fracture mechanics. Human femur can experience brittle behavior to quasi-brittle failure behavior depending mainly on bone organ geometry and intrinsic properties, viscosity, specimen preparation (fresh frozen, embalmed), aging (decrease in the bone toughness) and the load testing speed. In general, at a low load rate (quasi-static regime), the proximal femur behaves as a quasi-brittle material with a non-linear behavior till complete fracture [101]. A high-resolution finite element models of trabecular bone incorporating bilinear constitutive model with asymmetric tissue yield strains in tension and compression was employed in [102]. A single-scale, high-resolution, voxel-based finite element model with geometrical and material nonlinearity based on rate-independent isotropic elasto-plasticity model of tissue material properties was employed in [103]. The role of tissue-level post-yield fully brittle versus fully ductile failure behavior on the overall strength of trabecular bone has been studied in [104].

One of the most successful single-scale femur models aimed at predicting overall femoral strength is based on the combination of quantitative computer tomography (QCT) and patient-specific finite element analysis (FEA) [105-108]. This so called QCT/FEA procedure consists of: (1) obtaining a 3D finite element mesh based on a QCT-scan of the femur, (2) determining the Young's modulus and failure strain for each element based on the CT grayscale numbers of the voxels in the elements, and (3) simulating the inelastic response under specific loading conditions. 3D FE meshes from the reconstructed QCT images can be generated using Mimics [109], Simpleware [110] or one of the open source codes such as Seg3D [111] in combination with Cleaver [112]. Bone density can be

estimated from Hounsfield units (HU) which represent the measured grey levels in the QCT scans. Young's modulus (E) and compressive strength (σ_y) have been correlated to bone density by the following empirical relation [113]

$$\begin{aligned} E &= a_E \rho^{b_E} \\ \sigma_y &= a_\sigma \rho^{b_\sigma} \end{aligned} \tag{1}$$

where the coefficients $a_E, b_E, a_\sigma, b_\sigma$ have been determined by a trial and error optimization procedure to improve the agreement between predicted and experimental fracture forces. In [107, 108], a simplified damage model was employed by which elements with the von Mises strain exceeding the yield strain ε_y were failed by assigning a very small Young's modulus. The model stiffness was then updated, the load was increased, and the model was solved again until the QCT/FEA load–displacement curve reached a plateau.

There have been, however, a number of attempts for nonlinear multiscale modeling of femur. In [114], damage and energy dissipation mechanisms at three length scales including mineralized collagen fibrils, lamellar and osteonal levels were discussed. In [115], a two-dimensional multiscale approach that linked mesoscale finite element model of the cortical bone with full trabecular architecture in human proximal femur. Hambli et al [116]combined the finite element analysis in 2D at the macroscale with neural network computations in 3D to link mesoscopic scale (trabecular network level) and macroscopic (whole bone). The input data for the artificial neural network are a set of bone material parameters and the applied overall stress. The output data are the instantaneous overall bone properties.

In the present dissertation we present multiscale approaches for fracture analysis of full scale femur. The first approach, is based on the reduced order homogenization [5, 10,

77, 78, 117-119] where trabecular and cortical bone unit cells having arbitrary number of degrees of freedom are systematically reduced to a handful of modes representing key deformational modes. The second approach is based on utilizing reduced order homogenization calibrated to limited experimental as a training tool to calibrate a simpler, anisotropic phenomenological model of damage. We will refer to the two multiscale approaches as reduced order homogenization (ROH) approach and accelerated reduced order homogenization (AROH). For model validation, we consider finite element model created from the quantitative computer tomography (QCT) in [108]. Since the QCT resolution is typically not sufficient to resolve the fine-scale details of the bone structure, in this study we position a generic trabecular and cortical bone microstructure bone consistent with its ability to adapt the internal structure at various scales with changes in the load environment [120-122]. The cortical bone unit cell has been positioned based on the combination of the morphological and mechanical (elasticity) information. The osteon in the cortical bone unit cell has been aligned to coincide with the principal direction of strain during walking. The trabecular bone unit cell has been positioned based purely on mechanical information. The elastic constitutive tensor will be rotated so that the overall Young's modulus of the cortical bone unit cell coincide with the direction of the maximum principal strain at the stance position.

This dissertation is organized in the following manner. Chapter 2 presents an enhanced ant colony algorithm aiming to optimize composite structure in multiple scales. Chapter 3 introduces an adaptive nonintrusive stochastic inverse solver which provides a new perspective to understand and predict the uncertainty of composite materials. In

Chapter 4, an innovative accelerated multiscale analysis of the fracture of human femur was presented. Chapter 5 finishes the dissertation with conclusions.

Chapter 2
Enhanced Ant Colony Optimization for Multiscale Problems

The present chapter addresses the issue of computational complexity of optimizing nonlinear composite materials and structures at multiple scales. Several solutions are detailed to meet the enormous computational challenge of optimizing nonlinear structures at multiple scales including: (i) enhanced sampling procedure that provides superior performance of the well-known ant colony optimization algorithm, (ii) a mapping-based meshing of a representative volume element that unlike unstructured meshing permits sensitivity analysis on coarse meshes, and (iii) a multilevel optimization procedure that takes advantage of possible weak coupling of certain scales. The proposed optimization procedure was demonstrated on elastic and inelastic laminated plates involving three scales.

2.1 Classic ACO

The Ant System (AS) algorithm is one implementation of a larger concept called swarm intelligence (SI), which is collective behavior of self-organized natural or artificial system. SI includes some other applications, such as particle swarm optimization [123], artificial bee colony optimization [124] and artificial swarm intelligence [125].

AS was first proposed by Marco Dorigo in 1992 [126]. The method was inspired by the collective behavior of real ants being able to find the shortest route to food by detecting the concentration of pheromone left by other ants. As in Figure 2, each member of the colony is searching for food, they deposit a chemical factor known as pheromone on the route back and forth between nest and food source, the deposited pheromone triggers a

social response in members of the same species (ants) and which evaporates over time. As a result, the shorter some specific routes are, the denser the pheromone concentration is. When selecting which route to take, ants have a higher probability to choose the routes with higher pheromone concentration, obviously to some extent of randomness. The randomness enables ants to discover new food sources. Eventually, for the simple example in Figure 2, route 2 would be identified as the optimal (shortest) one.

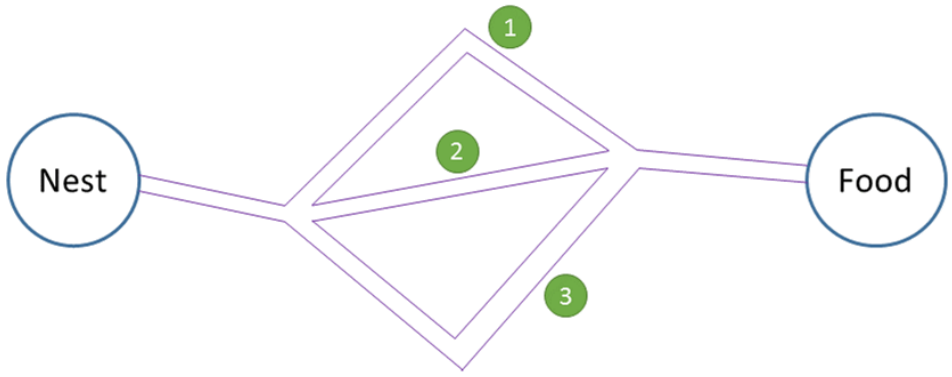

Figure 2 Ant food searching in nature

In 1997, Dorigo and Gambardella presented the algorithm for solving the traveling salesman problem (TSP) [127]. Since then, the ACO has been formalized into a combinatorial optimization metaheuristic [128] and has been used to solve many combinatorial optimization problems.

While successfully being used to solve discrete optimization problems, ACO has been extended to solve optimization problems in continuous spaces (ACO_R) [129] and mixed spaces [130, 131].

Socha and Dorigo expanded the algorithm into the continuous domain [129] by introducing a Gaussian kernel probability density function (PDF). The kernel PDF, denoted

as $G^i(x)$, is a weighted sum of several one-dimensional Gaussian functions $g_l^i(x)$. Then the kernel PDF for parameter *i* can be written as

$$G^i(x) = \sum_{l=1}^{k} w_l g_l^i(x) = \sum_{l=1}^{k} w_l \frac{1}{s_l^i \sqrt{2p}} e^{-\frac{(x-m_l^i)^2}{2s_l^{i2}}} \tag{2}$$

where w_l is the weight of the l^{th} archived solution, m_l^i is the mean value of parameter *i* for the l^{th} archived solution and s_l^i is the corresponding standard deviation.

s_1^1	s_1^2	⋯	s_1^i	⋯	s_1^n	$f(\boldsymbol{s_1})$	w_1
s_2^1	s_2^2	⋯	s_2^i	⋯	s_2^n	$f(\boldsymbol{s_2})$	w_2
⋮	⋮	⋱	⋮	⋱	⋮	⋮	⋮
s_l^1	s_l^2	⋯	s_l^i	⋯	s_l^n	$f(\boldsymbol{s_l})$	w_l
⋮	⋮	⋱	⋮	⋱	⋮	⋮	⋮
s_k^1	s_k^2	⋯	s_k^i	⋯	s_k^n	$f(\boldsymbol{s_k})$	w_k
G^1	G^2		G^i		G^n		

Figure 3 Archived solutions

Figure 3 schematically illustrates a typical solution archive. s_l^i is the i^{th} parameter for the l^{th} solution, $f(\boldsymbol{s}_l)$ is the value of objective function with parameter $\boldsymbol{s}_l = \{s_l^1, s_l^2, \text{L}, s_l^n\}$ and w_l is the weight of the l^{th} solution. Solutions archived are ordered according to their quality. For an optimization problem: $f(\boldsymbol{s}_1) \le f(\boldsymbol{s}_2) \le \text{L} \le f(\boldsymbol{s}_k)$. The associated weight is proportional to the solution quality, so that $w_1 \ge w_2 \ge \text{L} \ge w_k$.

In practice, when constructing G^i, the following equations are used

$$m_l^i = s_l^i \tag{3}$$

$$s_l^i = x\sum_{e=1}^{k} \frac{\left|s_e^i - s_l^i\right|}{k - 1} \tag{4}$$

$$w_l = \frac{1}{qk\sqrt{2p}} e^{-\frac{(l-1)^2}{2q^2k^2}} \tag{5}$$

where ξ and q are algorithm parameters. q; when q is small, the top-ranked solutions are preferred. And higher ξ acts similarly with the evaporation of pheromone of the real ants and is associated with lower convergence speed.

The sampling process is accomplished as follows. First, the algorithm has to construct the kernel PDF, the probability of l^{th} Gaussian function is chosen is computed as

$$p_l = \frac{w_l}{\sum_{m=1}^{k} w_m} \tag{6}$$

With the constructed kernel PDF, each ant would randomly pick a sample and evaluate the objective function.

After each ant finishes evaluating the sample, the solution archive is updated by appending the newly evaluated samples and sorting the expanded archive. Then the archive would drop those with bad quality. For example, if n ants are employed, then the archive would be appended with n new solutions and after sorting, the last n solutions would be discarded.

The general algorithm of ACO metaheuristic is depicted in Algorithm 1 below. The algorithm consists of three phases. Initially, it evaluates certain number of random solutions and then in the Construct Solutions phase, each ant generates a new solution. The new solution is then appended to the initial solution list and the appended solution list is sorted according to the objective function value, such that the worst solutions is discarded after sorting. In the optional Daemon Actions phase, which is also regarded as a Local

Search phase, some local search algorithms could be implemented to more efficiently explore the local space. The Update Pheromone phase mimics the evaporation of ant pheromone. The purpose of the Update Pheromone phase is to increase the probability of new ants to choose promising solutions and decrease the chance of choosing the bad ones. A detailed discussion of the algorithm can be found in various papers and books [129, 132, 133].

Algorithm 1: Classic ACO

```
Initialize solution parameters
while termination condition is not met do
    Construct Solutions from Ants
    Daemon Actions                (optional)
    Update Pheromone
end while
```

Applying a local search algorithm to solutions generated by ACO usually improves the performance of ACO [134-137]. Gradient-based optimization algorithms have been widely utilized as local search algorithms in combination with multiple swarm intelligence algorithms by a number of investigators [138-140].

The classic ACO is not without deficiencies. Since it only allows the best ant to update the trails at every cycle, the algorithm may stagnate too early, preventing further improvement (Stutzle and Hoos 1997, Gambardella, Martinoli et al. 2006). Studies suggest that adding a restarting feature or adopting parallel searches adds ACO to more efficiently find the global optimal solution [141, 142]. While premature stagnation can be eventually

overcome by repeatedly restarting the ACO, it often leads to suboptimal performance since newly added samples might be exploring nearly the same space of design variables.

2.2 Random Sphere Packing

For complex multiscale problems, the overhead that resulting from an elaborate sampling algorithm is negligible in comparison to the computational cost of a single realization. Thus, the ultimate goal is to devise an intelligent sampling algorithm that finds an optimal global solution with minimal number of searches. In the present section, we show that by uniformly sampling the design space using a variant of random sphere packing (Figure 4) the performance of ACO can be considerably improved. Random sphere packing (RSP) algorithm constructs non-overlapping spheres that fill the domain of choice. The RSP algorithm with identical spheres has been utilized in various fields of physics, engineering, biology and chemistry [143-145]. Further improvement can be obtained by taking advantage of weak (or one-way) coupling of design variables represented by often weakly coupled scales.

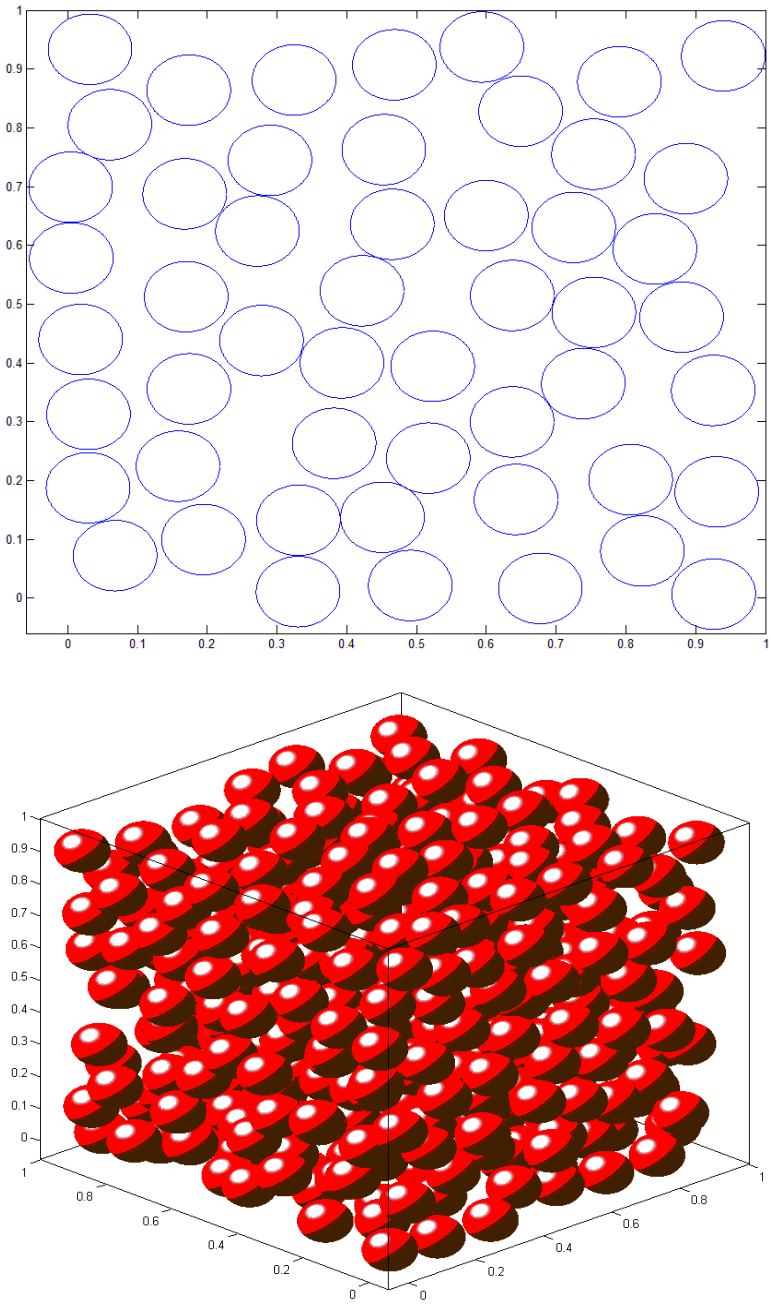

Figure 4 Examples of a 2D RSP and a 3D RSP

2.3 Enhanced ACO

In this section, we describe the principal elements of the enhanced ACO (EACO) and schematically illustrate it on a model problem. The EACO is designed to explore the design variable subspace that has not been sufficiently explored by placing new samples in

so-called “fresh” subspace. The sampling process of EACO is designed to exclude the regions that have been heavily sampled.

2.3.1 Adaptive Random Sphere Sampling (RSS)

The ACO utilizes classic random sampling (CRS) to obtain initial samples. For the ACO with restarting feature, the use of CRS often results in certain parts of the search space being repetitively explored, since the newly added samples may land close to those previously sampled while a certain portion of the space might be under-sampled.

Compared with the CRS, random sphere sampling (RSS) with properly selected sphere size is intended to provide more uniform sampling. To illustrate the advantage of RSS over CRS, consider the n-dimensional space Ω. The space Ω can be subdivided into M intervals in n dimensions, each interval in each dimension corresponding to a subspace $\Omega_{k,d}$ where $k \in [1, M]$ and $d \in [1, n]$. Let $W_{k,d}$ be the union of all (hyper) spheres in $W_{k,d}$. Figure 5.a and Figure 5.b depict an example of CRS and RSS sampling for a two-dimensional space subdivided into 20 intervals (n = 2, M = 20) with the same number of samples for both RSS and CRS. Figure 5.b and Figure 5.c illustrate the distribution of $W_{k,d}$ for the CRS, whereas Figure 6.b and Figure 6.c depict the distribution of $W_{k,d}$ for the RSS. It can be clearly seen that the RSS gives rise to much more uniform distribution of samples than the CRS.

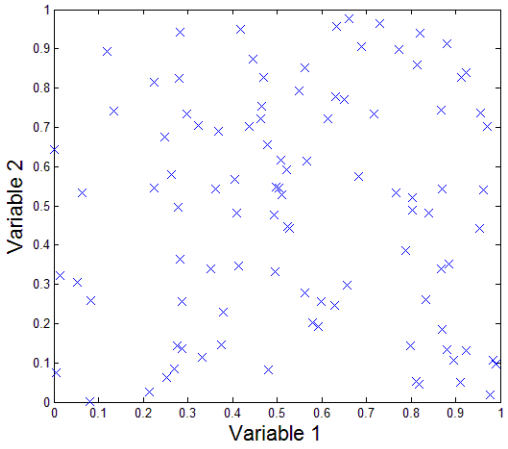

(a) Sample distribution

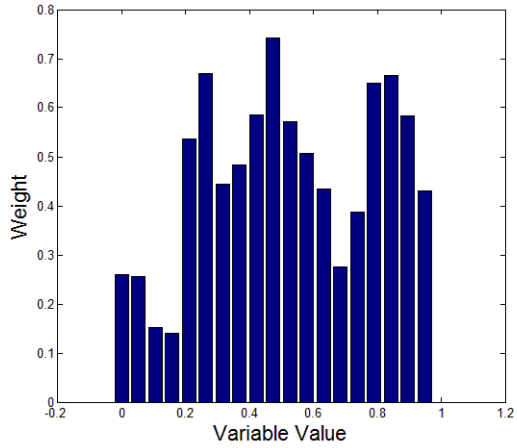

(b) $W_{k,1}$

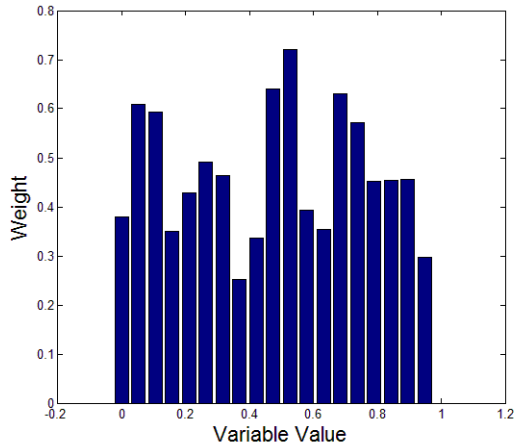

(e) $W_{k,2}$

Figure 5 CRS sampling

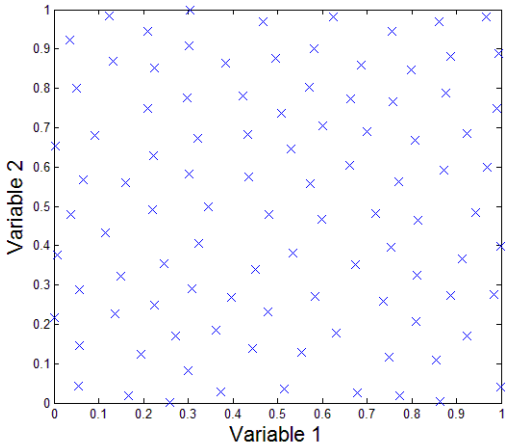

(a) Sample distribution

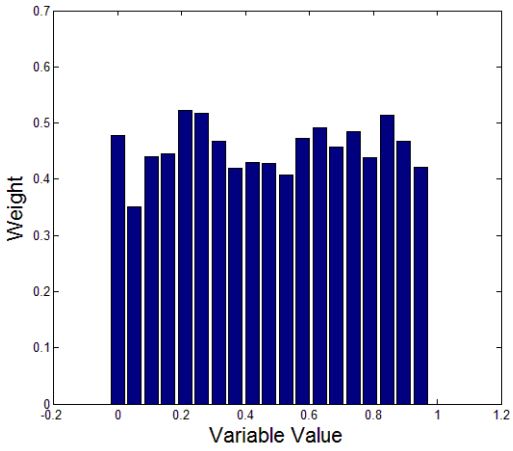

(b) $W_{k,1}$

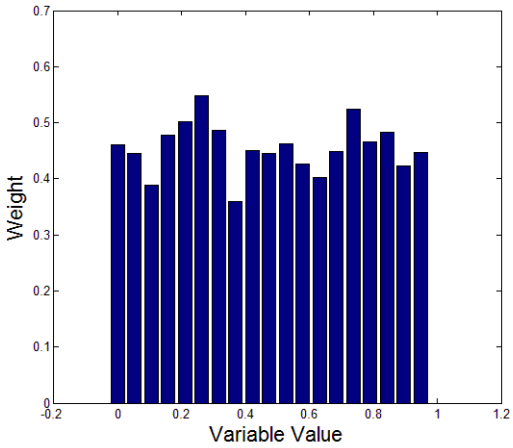

(c) $W_{k,2}$

Figure 6 RSS sampling

The RSS, however, has a number of shortcomings. Figure 7 illustrates the performance of RSS in terms of CPU time as the number of samples increases. It can be seen that stagnation starts after 400 samples at which time the CPU time grows exponentially.

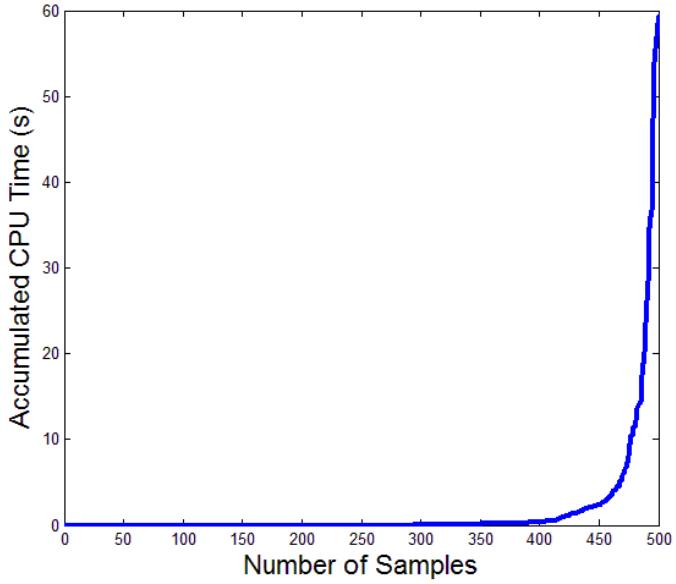

Figure 7 The CPU time versus number of samples using RSS for three-dimensional spaces

To overcome the stagnation, instead of equal-diameter spheres, smaller spheres are introduced, if and when the stagnation is detected. This approach improves the packing efficiency without significantly affecting the sampling uniformness.

Figure 8 and Figure 9 compare the CRS and the adaptive RSS for three-dimensional sampling space. It can be seen that the adaptive RSS retains the uniformness of sampling along each dimension in comparison to CRS.

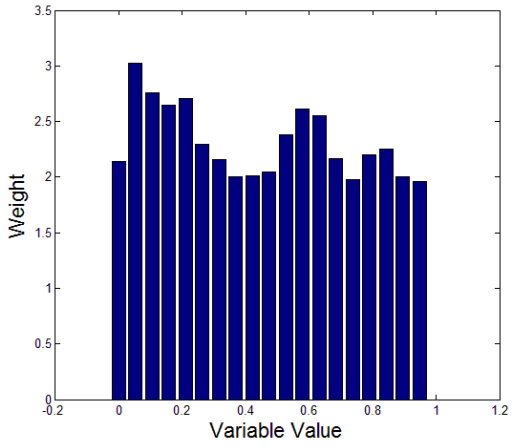

(a) Dimension 1

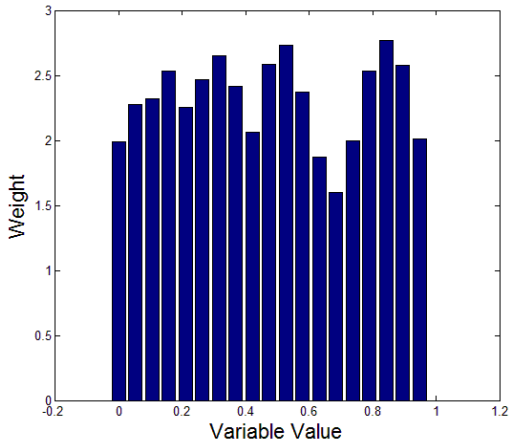

(b) Dimension 2

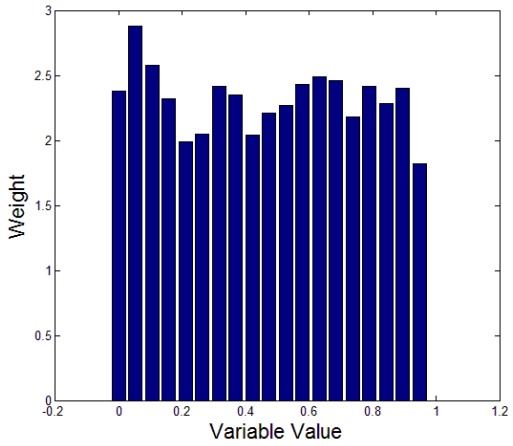

(c) Dimension 3

Figure 8 Classic random sampling

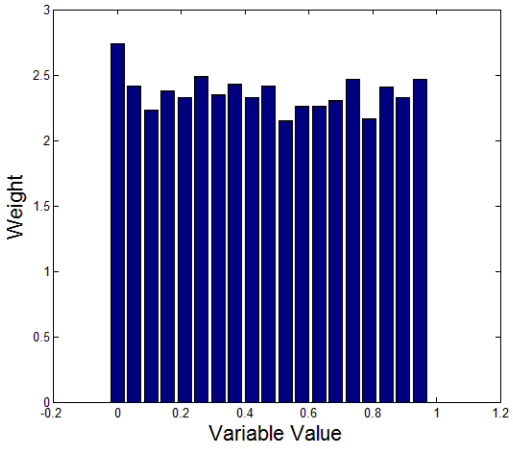

(a) Dimension 1

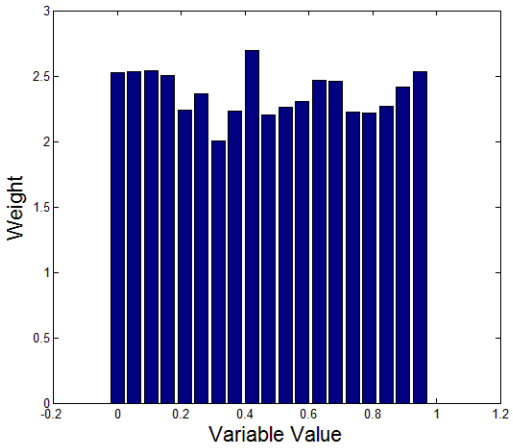

(b) Dimension 2

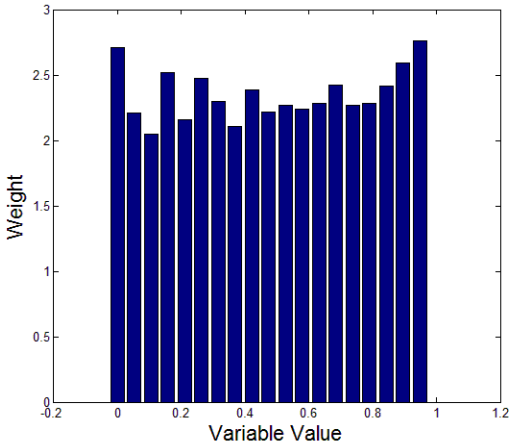

(c) Dimension 3

Figure 9 Adaptive RSS with dual-sized spheres

2.3.2 Local Subspaces Identification

In addition to keeping newly added samples away from the previous samples each time the ACO restarts, it is desirable to keep sampling away from portions of space that have been already extensively explored by ACO due to stagnation resulting in accumulation of sampling points in local subspaces $\Omega_{LS} \subset \Omega$. To illustrate how local subspaces are identified consider a two-dimensional space in Figure 10. With completion of a single ACO cycle, the current best solution x_{CBS} is identified. In the vicinity of $x_{CBS} \in \Omega_{LS}$, the local subspace Ω_{LS} contains considerable number of sampling points $x_i \in \Omega_{LS}$. Ω_{LS} is defined to encompass K sampling points specified as a certain fraction of the total number of samples. In other words, it is the smallest subspace that contains *K* sampling points. Let $\|x_{CBS} - x_i\|_1$ denote the distance between x_{CBS} and any other sample *i* in L_1 norm. Ω_{LS} is thus defined as an *n*-dimensional box that contains *K* sampling points that are closest to x_{CBS} in L_1 norm.

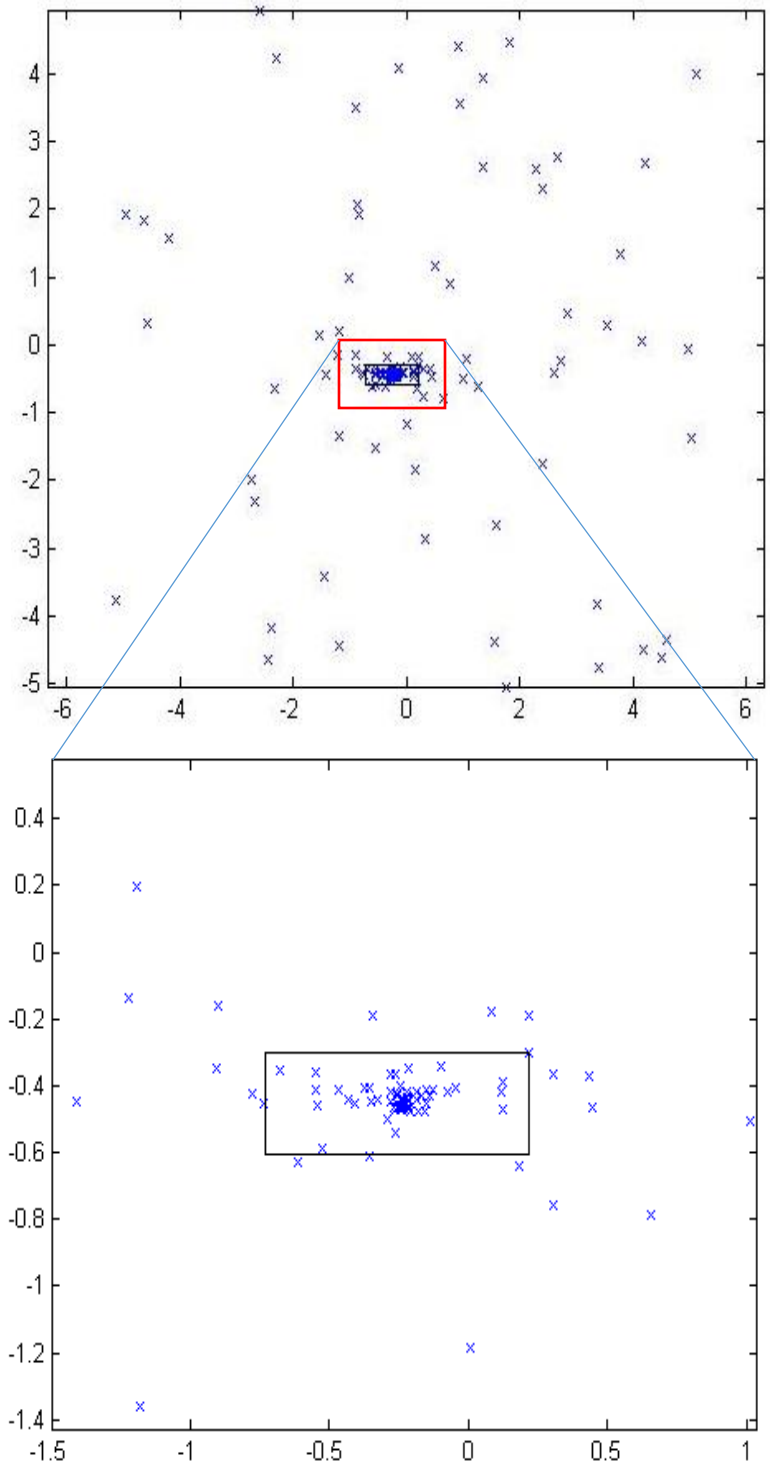

Figure 10 Identified $\Omega_{LS} \subset \Omega$ (top) and zoomed view (bottom)

Once the Ω_{LS} is defined, the ACO sampling process will prevent the new sampling points to land in Ω_{LS}. Consequently, the ACO is forced to sample in the subspaces that have not been explored so far.

Let $d_{\min}^{0}$ above be the user-specified initial minimal distance between two samples. Clearly, if $d_{\min}^{0}$ is infinitesimal, adaptive RSS will behave like CRS; if on the other hand $d_{\min}^{0}$ is too large, some local/global minima might be unexplored. In the adaptive RSS, the allowable minimal distance is adaptively selected based on the number of unsuccessful tries of adding a new sample. The initial value can be estimated by using the volume of *n*-dimensional sphere (*n*-ball)

$$R = \sqrt[n]{\frac{V_n \Gamma\left(\frac{n}{2}+1\right)}{\pi^{\frac{n}{2}}}} \tag{7}$$

where R is the radius of the *n*-dimensional sphere, which is equal to $d_{\min}^{0}/2$, and Γ is the gamma function. V_n can be estimated based on the parameters of the EACO algorithm as

$$V_n = \frac{V}{k \cdot m \cdot l} \tag{8}$$

where $V \equiv 1$ is the volume of the *n*-dimensional parametric domain; *k* the archive size, *m* the number of ants and *l* the maximal number of restarts.

The minimal distance is adaptively selected using the following heuristics

$$d_{\min}^{\text{new}} = \frac{1}{\sqrt[3]{a}} d_{\min}^{\text{present}} \tag{9}$$

where $d_{\min}^{\text{present}}$ is the present minimal distance, $d_{\min}^{\text{new}}$ denotes the new minimal distance and a is a number of attempts required to add a new sample. Note that initially, $d_{\min}^{\text{present}} = d_{\min}^{0}$, and as long as *a = 1* the initial minimal distance remains the same.

2.3.3 Illustration of the EACO

For the illustration of the algorithm, consider a two-dimensional Holder Table function (Figure 11), which is defined as

$$f(x) = -\left| e^{\left|1-\frac{\sqrt{x_1^2+x_2^2}}{\pi}\right|} \sin(x_1)\cos(x_2) \right| \quad x_i \in [-10,10] \text{ for } i = 1,2 \tag{10}$$

The function has four global optima at $x_i = \pm 9.664590028909654$ *for* $i = 1,2$ with the function value of -19.20850256788675.

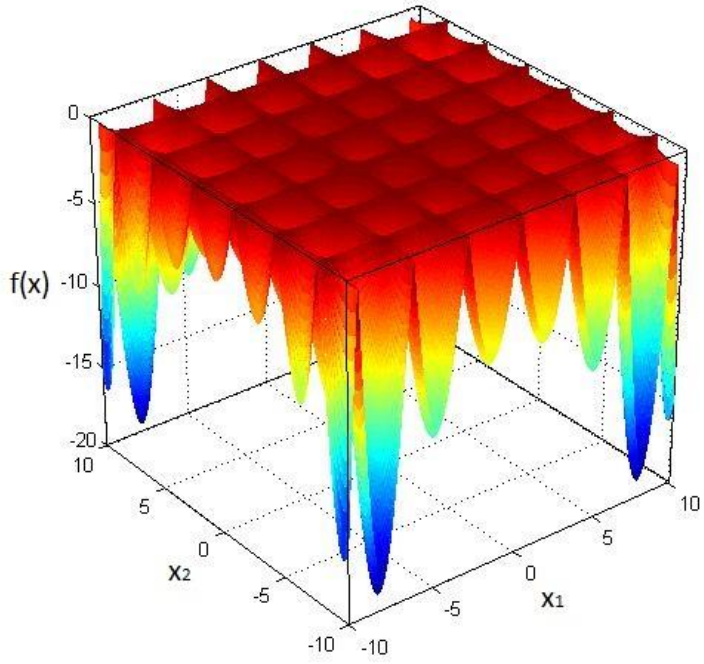

Figure 11 Holder Table function

Solution parameters considered here are summarized as Table 1.

Table 1 Solution parameters

Number of Ants	5
Archive Size	10
Speed of Convergence (ξ)	0.85
Locality of the Search Process	0.1
Maximum Number of Restarts	4
Maximum Number of Iterations	100

Figure 12.a - Figure 12.d depict the samples being added in each restart. It can be seen that each time ACO restarts, new samples avoid the local subspaces Ω_{LS} identified

in the previous restarts. Figure 12.e illustrates that samples added in each new restart are kept away from those being added previously.

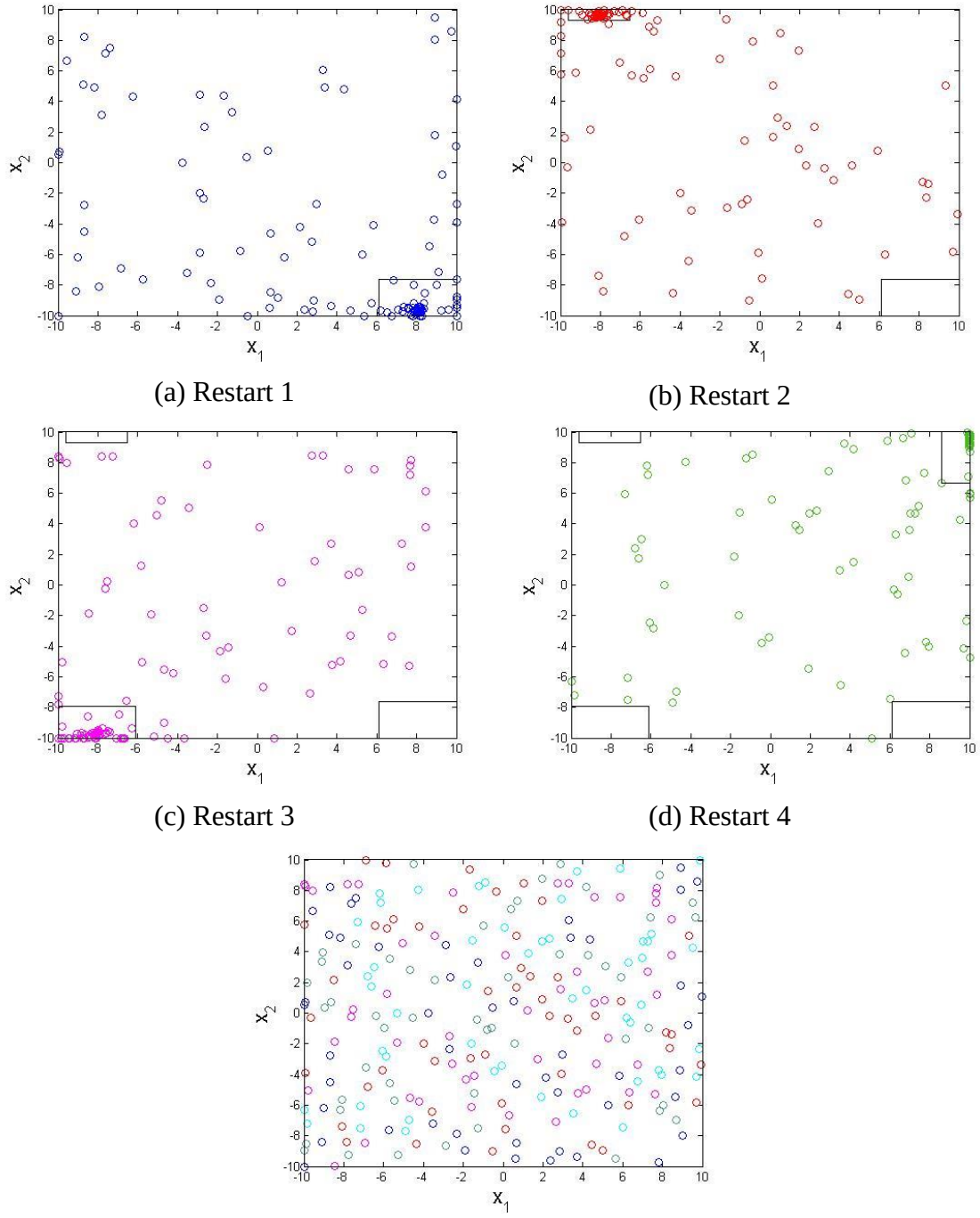

(a) Restart 1

(b) Restart 2

(c) Restart 3

(d) Restart 4

(e) Final sample distribution. Colors depict sampling points obtained in different restarts

Figure 12 Sampling process for the two-dimensional Holder Table function

2.4 Specificities for multiscale problems

Consider a typical three-scale problem depicted in Figure 13 where Ω, Λ and Θ denote the spaces of design variables at a macroscale, mesoscale and microscale, respectively.

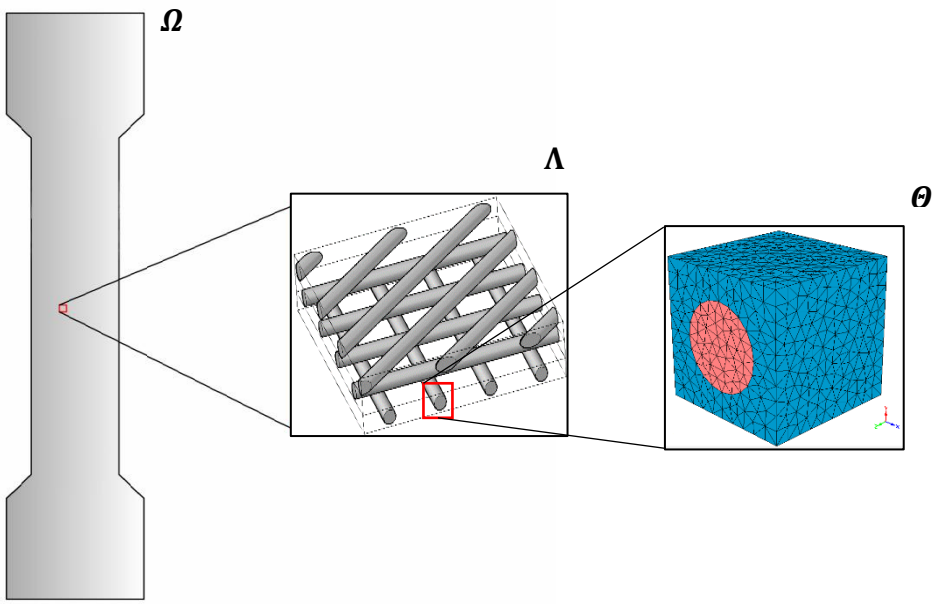

Figure 13 Schematic illustration of triple-scale optimization

The three-scale optimization problem is defined as

$$\begin{aligned} &\min\ f(\boldsymbol{x},\boldsymbol{y},\boldsymbol{z}), \quad \boldsymbol{x}\in\Omega,\boldsymbol{y}\in\Lambda,\boldsymbol{z}\in\Theta \\ &\text{subject to } g_i(\boldsymbol{x},\boldsymbol{y},\boldsymbol{z})\geq 0, \quad i=1,...,m \quad (\text{optional}) \\ &\qquad \boldsymbol{x}_{lb}\leq\boldsymbol{x}\leq\boldsymbol{x}_{ub} \\ &\qquad \boldsymbol{y}_{\text{lb}}\leq\boldsymbol{y}\leq\boldsymbol{y}_{ub} \\ &\qquad \boldsymbol{z}_{\text{lb}}\leq\boldsymbol{z}\leq\boldsymbol{z}_{ub} \end{aligned} \tag{11}$$

where $f(\boldsymbol{x},\boldsymbol{y},\boldsymbol{z})$ is an objective function defined on $[\Omega\otimes\Lambda\otimes\Theta]$.

2.4.1 Representative Volume Element (RVE) Generation

One of the challenges in optimization of the discretized fine-scale geometry is that at each realization, the RVE has to be regenerated. The difficulty stems from the fact that

for sensitivity analysis employed in local searches, random unstructured finite meshes cannot precisely reflect perturbations in RVE geometry in particular when the meshes are coarse.

Here we propose an alternative approach illustrated on the non-crimp fabric (NCF) composite microstructure that is the most commonly employed composite material system in automotive industry. The RVE geometry can be represented by three parameters: the volume fraction of a fabric ϕ, the ratio between the major and minor axis of an elliptical fabric cross-section ρ and the angle of fabric orientation α as shown in Figure 9. Typically, to keep the composite cost fixed and to optimize for performance, the volume fraction is kept fixed, and thus $\boldsymbol{z} = (\rho, \alpha)$ are the only two active microstructural parameters. For complex textile architectures, considerably more parameters would be required to parametrically define the RVE geometry. Prior to optimization process, we construct an auxiliary base RVE mesh with $\rho = 1$ as shown in Figure 14.

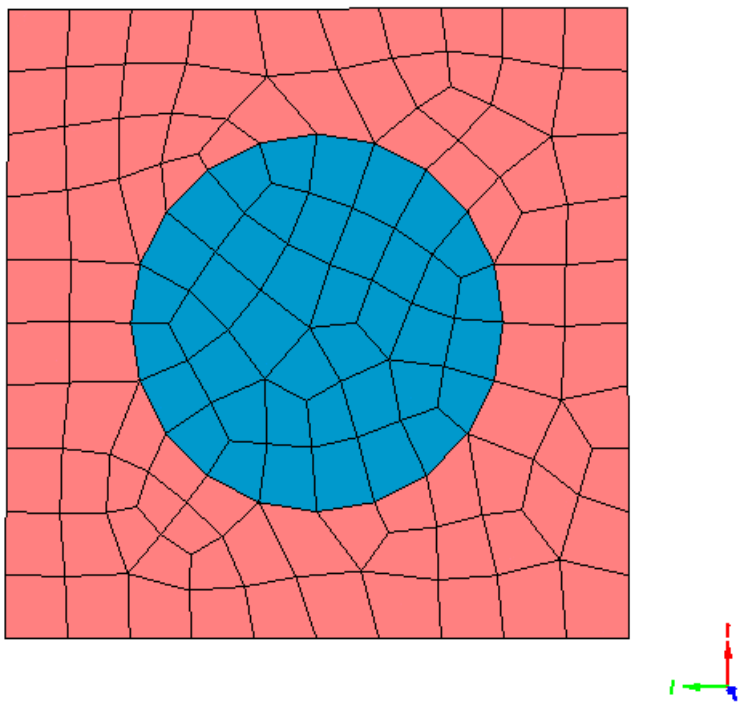

Figure 14 The base RVE microstructure and mesh

Figure 15 depicts a finite element mesh of an RVE that has the same number of nodes, elements and connectivity of elements as the base RVE mesh in Figure 9 with only difference that r = 1.2 and $\alpha = 45^0$. The microstructure is assumed to remain locally periodic for all possible values of parameters $\boldsymbol{z}$. The finite element mesh in Figure 10 is constructed by linear mapping $\boldsymbol{T}(\boldsymbol{c},\boldsymbol{z})$ of the base RVE mesh in Figure 9 as

$$\boldsymbol{c}' = \boldsymbol{T}(\boldsymbol{c},\boldsymbol{z})\boldsymbol{c} \tag{12}$$

where $\boldsymbol{c} = [\chi_1, \chi_2, \chi_3]^T$ are the coordinates of nodes in the base mesh and $\boldsymbol{c}'$ are the nodal coordinates of the NCF composite mesh in Figure 10.

For the NCF composite considered in Figures 10, in which the fabric is aligned along χ_1 direction, $\boldsymbol{T}(\boldsymbol{c},\boldsymbol{z})$ is defined as

$$\boldsymbol{T}(\boldsymbol{c},\boldsymbol{z}) = \begin{cases} \boldsymbol{R}(\alpha)\boldsymbol{S}_F(\rho)\boldsymbol{R}'(\alpha) & \text{fabric phase} \\ \boldsymbol{R}(\alpha)\boldsymbol{S}_M(\boldsymbol{c},\rho)\boldsymbol{R}'(\alpha) & \text{matrix phase} \end{cases} \tag{13}$$

where $\boldsymbol{S}$ and $\boldsymbol{R}$ are stretch and rotation matrices, respectively.

The rotation matrix $\boldsymbol{R}(\alpha)$ is defined as

$$\boldsymbol{R}(\alpha) = \begin{bmatrix} 1 & 0 & 0 \\ 0 & \cos(\alpha) & -\sin(\alpha) \\ 0 & \sin(\alpha) & \cos(\alpha) \end{bmatrix} \tag{14}$$

The stretch operator for fabric phase $\boldsymbol{S}_F(\rho)$ is given as

$$\boldsymbol{S}_F(\rho) = \begin{bmatrix} 1 & 0 & 0 \\ 0 & \rho & 0 \\ 0 & 0 & 1/\rho \end{bmatrix} \tag{15}$$

The matrix phase has to satisfy two conditions: (i) nodes on RVE boundary have to remain in their original positions and (ii) nodes at the fabric-matrix interface should coincide with nodes on the mapped fabric. We construct a scalar blending function $m(\boldsymbol{c})$ so that it equals to 1 at the RVE boundary and 0 at the interface with fabric. Consequently, the stretch operator for the matrix phase $\boldsymbol{S}_M(\boldsymbol{c},\rho)$ is defined as

$$\boldsymbol{S}_M(\boldsymbol{c},\rho) = m(\boldsymbol{c})\boldsymbol{I} + (1 - m(\boldsymbol{c}))\boldsymbol{S}_F(\rho) \tag{16}$$

where $\boldsymbol{I}$ is a 3 by 3 identity matrix.

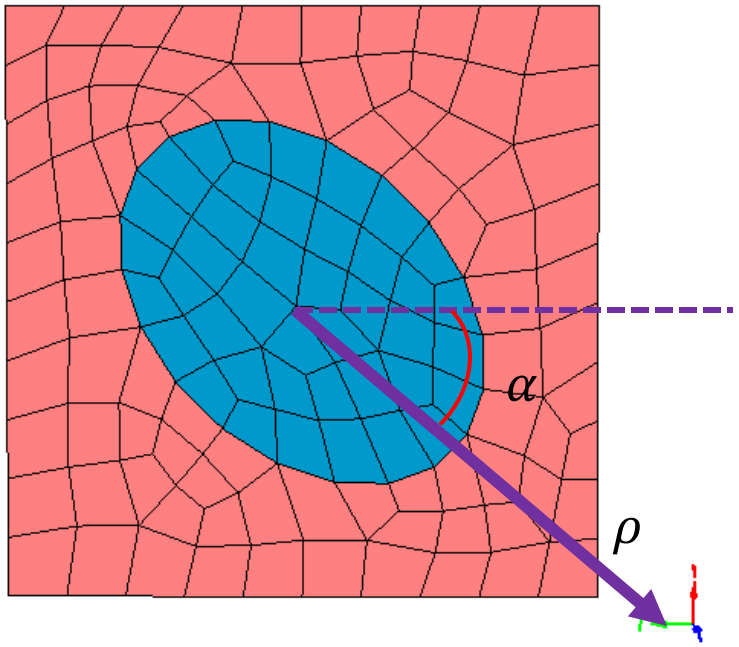

Figure 15 Non-crimp fabric composite (NCF) RVE with $r = 1.2, a = 45^{o}$

Figure 16 and Figure 17 depict how the homogenized properties (with fabric along χ_1 direction) change with the stretch ratio and direction. Here we assume that both fabric and matrix are isotropic materials with properties depicted in Table 2. The fabric volume fraction is 30%.

Table 2 RVE material properties

Phase	Young's Modulus (GPa)	Poisson's Ratio
Matrix	1	0.1
Fabric	10	0.1

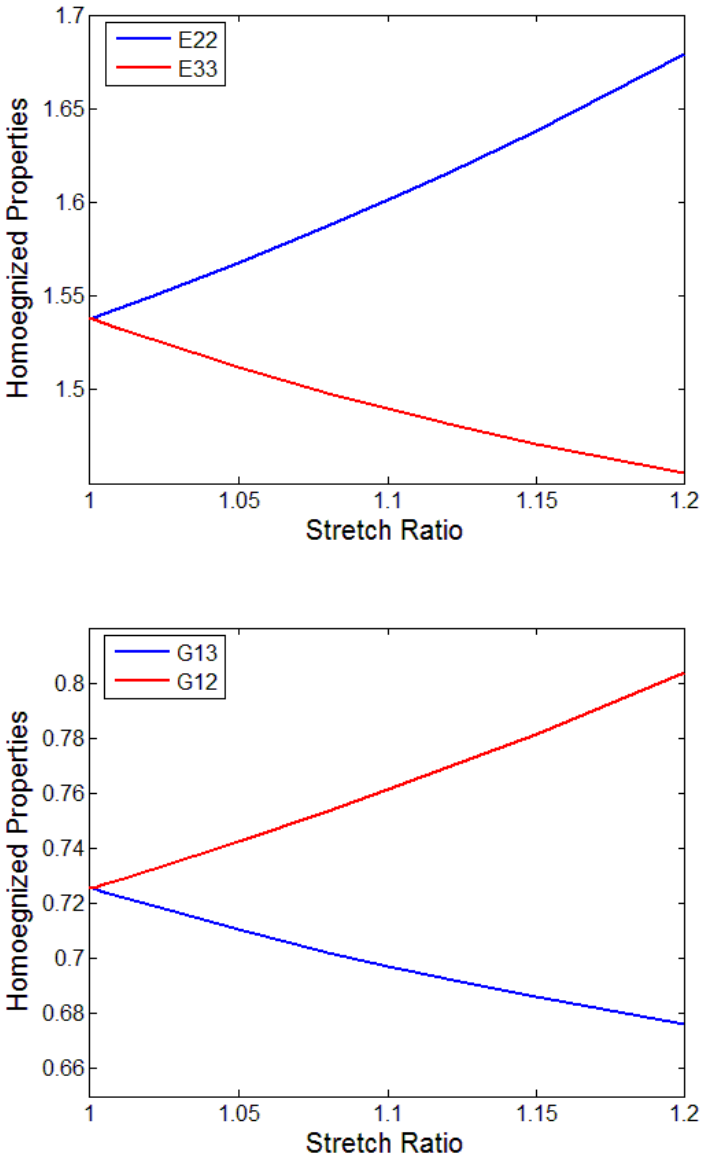

Figure 16 Homogenized properties vs. stretch ratio ρ

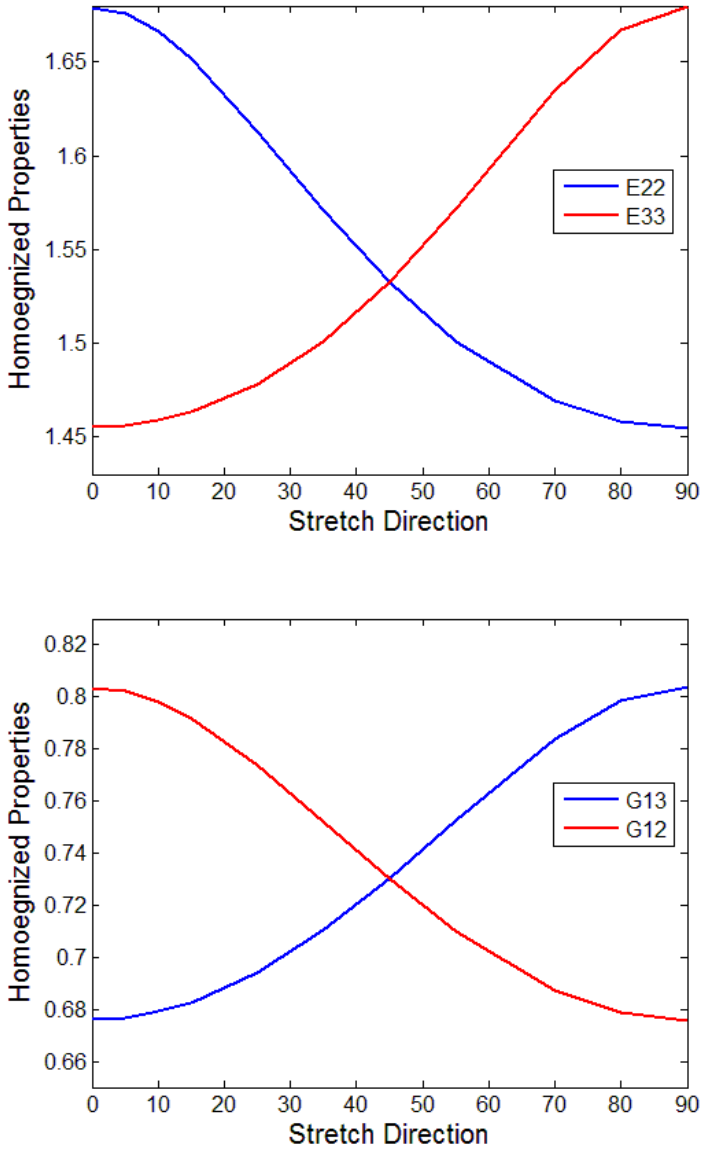

Figure 17 Homogenized properties vs. stretch direction α

2.4.2 Multiscale Optimization with Weak Coupling of Scales

Multiscale optimization naturally falls into the category of multilevel optimization methods [146]. By this approach, a large optimization problem is decomposed into a hierarchy of subproblems. At the top level, a subproblem optimizes a simplified model that describes the overall behavior of the system. At the lower levels, subproblems optimize

increasingly detailed representations of subsystems. The effectiveness of multilevel optimization depends on the strength of coupling between various subproblems that necessitate iterative process. In the limit, if a problem is decomposed into a number of subproblems that are totally uncoupled, there is no need to iterate through the optimization of the various subproblems to obtain the optimum design of the system and it is very likely that the multilevel optimization approach will require less computer time than a monolithic scheme that simultaneously considers all design variables. This is often the case in multiscale problems schematically illustrated in Figure 12. In Section 5, we show that a coupled macro-meso scale subproblem is weakly couple to the microscale subproblem.

2.5 Validation for Classical Objective Functions

In this section, we compare the proposed EACO algorithm with the ACO_R. For comparison, we consider the classical optimization test functions summarized in Table 4. Each function is optimized 100 times by the EACO and ACO_R using the same number of ants, same size of archive and same maximum number of restarts depicted in Table 3.

Table 3 ACO parameters

Number of Ants	2
Archive Size	50
Speed of Convergence (ξ)	0.85
Locality of the Search Process	0.1
Maximum Number of Restarts	500

Table 4 Test functions

Rosenbrock Func. (n=20)	$f(x)=\sum_{i=1}^{n-1}\left[100\left(x_{i+1}-x_i^2\right)^2+\left(x_i-1\right)^2\right]$	$x_i\in[-\infty,\infty]$ *for* $i=1,...,n$
Schwefel Func. (n=20)	$f(x)=418.9829n-\sum_{i=1}^{n}x_i\sin\left(\sqrt{\lvert x_i\rvert}\right)$	$x_i\in[-500,500]$ *for* $i=1,...,n$
Rastrigin Func. (n=20)	$f(x)=10n\sum_{i=1}^{n}\left[x_i^2-10\cos\left(2\pi x_i\right)\right]$	$x_i\in[-5.12,5.12]$ *for* $i=1,...,n$
Salomon Func. (n=20)	$f(x)=1-\cos\left(2\pi\sqrt{\sum_{i=1}^{n}x_i^2}\right)+0.1\sqrt{\sum_{i=1}^{n}x_i^2}$	$x_i\in[-100,100]$ *for* $i=1,...,n$

Table 5 Comparison of the results for various test functions. Note that lower values of mean obtained by the EACO in comparison to the ACO_R

Function	Algorithm	Evaluation Limit	Mean	STD
Rosenbrock	EACO	1×10^6	1.02853×10^2	0.896259×10^2
	ACO_R	1×10^6	1.19408×10^2	2.77244×10^2
Schwefel	EACO	1×10^6	2.74620×10^3	8.99055×10^2
	ACO_R	1×10^6	2.97164×10^3	1.00924×10^3
Rastrigin	EACO	1×10^6	1.07019×10^2	0.433414×10^2
	ACO_R	1×10^6	1.13407×10^2	0.485771×10^2
Salomon	EACO	1×10^6	0.65158	0.15693
	ACO_R	1×10^6	0.65595	0.17475

We take a closer look at the Rosenbrock function and compare the average number of function evaluations using EACO and ACO_R with the same parameters. In both cases, the solution converges when the difference between the current objective function value and the optimum solution is less than 1×10^{-4}. It can be seen from

Table 6 that the EACO reduces the average number of function evaluations by 34.1% in comparison to the ACO_R.

Table 6 Average number of evaluations for the Rosenbrock function

EACO	4.49695×10^5
ACO_R	6.82147×10^5

2.6 Validation for Multiscale Problems

2.6.1 Elastic Semi-circular Laminated Composite Plate

We consider a semi-circular composite laminated plate with radius of 5.0 meters and thickness of 0.025 meters as shown in Figure 18. The plate is fixed along the straight edge and is subjected to pressure of 1.0 kN/m^2 at its top surface. Material properties of the laminated plate are listed in Table 7.

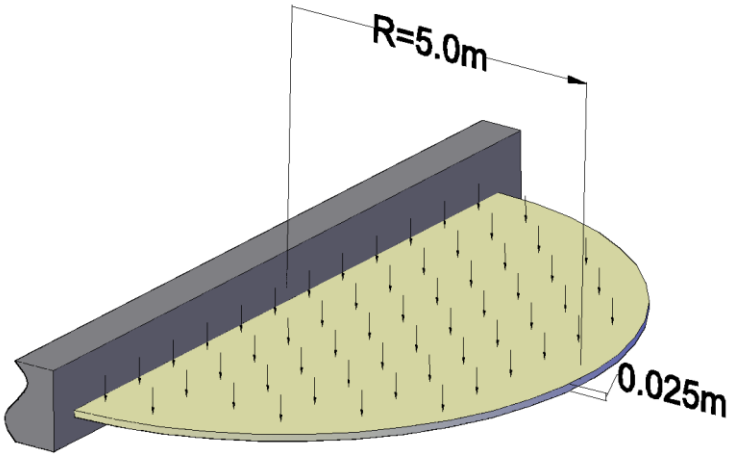

Figure 18 Geometry, loading and boundary conditions of a semi-circular laminated plate subjected to pressure

Table 7 Composite Material Properties

Phase	E (GPa)	ν
Matrix	3.14	0.18
Fabric	233.0	0.1

The objective is to maximize the stiffness of the plate, which in turn is accomplished by minimizing the total strain energy of the plate.

We employ a two-phase optimization procedure that takes advantage of weak coupling between macro- and meso- scale on one hand, and microscale on the other. In

Phase 1, we conduct a simultaneous macroscale-mesoscale optimization using EACO algorithm assuming the base RVE microstructure (see

Figure 19). In Phase 2, the microscale optimization is performed keeping the macro- and meso- scale design variables obtained from Phase 1 as fixed. We iterate back to Phase 1, but find no further solution improvement suggesting weak coupling between the scales.

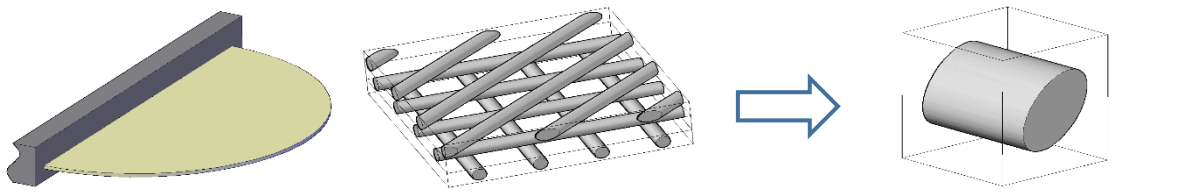

Figure 19 Two-phase optimization of the elastic semi-circular laminated composite plate

2.4.1.1 Phase 1: Simultaneous macroscale-mesoscale optimization

The design variables at the macroscale are 10 control points along the radius of the plate as shown in Figure 20. The control points can only move in the out-of-plane direction and are connected by spline. The geometry of the plate is obtained by 180° revolution of its radius. The lower and upper bounds of control points is selected as [-0.3, 0.3].

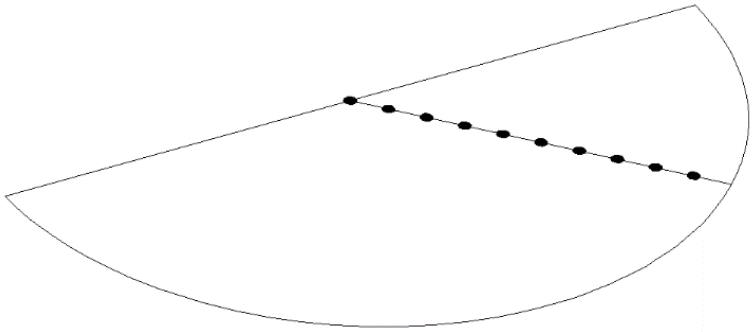

Figure 20 Macroscale design variables (control points) for the elastic semi-circular laminated composite plate

At the mesoscale, the design variables are the laminate stacking sequence. It is assumed that the laminate is: (i) symmetric to avoid moment - axial force coupling, (ii) balanced, i.e., layers in the opposite directions $\pm\alpha$ appear as pairs, and (iii) there are 40 layers.

Based on the above restrictions, there are 10 independent mesoscale design variables in the range of [-90, 90].

2.4.1.2 Phase 2: Microscale optimization

We consider the NCF microstructure described in Section 3.1. The two microscale design variables are the stretch ratio and stretch direction bounded by [0.7, 1.3] and [-90, 90], respectively.

2.4.1.3 Optimization Results

The evolution of the objective function with number of samples is summarized in Figure 19. Optimization starts with plate being flat (Figure 22) and lamination parameters of [45, 45, 45, 45, 45, 45, 45, 45, 45, 45]. In the optimization process, the strain energy of the plate decreases from 4.79×10^{4} N m to 1.39×10^{1} N m. The optimal macroscale design

is illustrated in Figure 23 with values of control points equal to [-0.3, -0.3, -0.3, 0.1, 0.291, 0.3, 0.3, -0.276, -0.3, -0.3]. The optimal layup is given by [10.81, -21.27, -89.07, 41.66, -51.08, -57.85, -39.13, -17.29, -6.95, 12.83, 33.39].

For the microscale optimization in Phase 2, the RVE is initially assumed to have circular fabric cross-section. The optimal solution results in stretch ratio of 0.7 and the stretch angle of 0 as shown as Figure 21. The microscale optimization reduces strain energy by 5.9% from 1.47×10^{1} N m to 1.39×10^{1} N m. The low fabric volume fraction, 30%, is the main reason for relatively low contribution resulting from microscale optimization. Iterating back to Phase 1 optimization, does not yield any improvement.

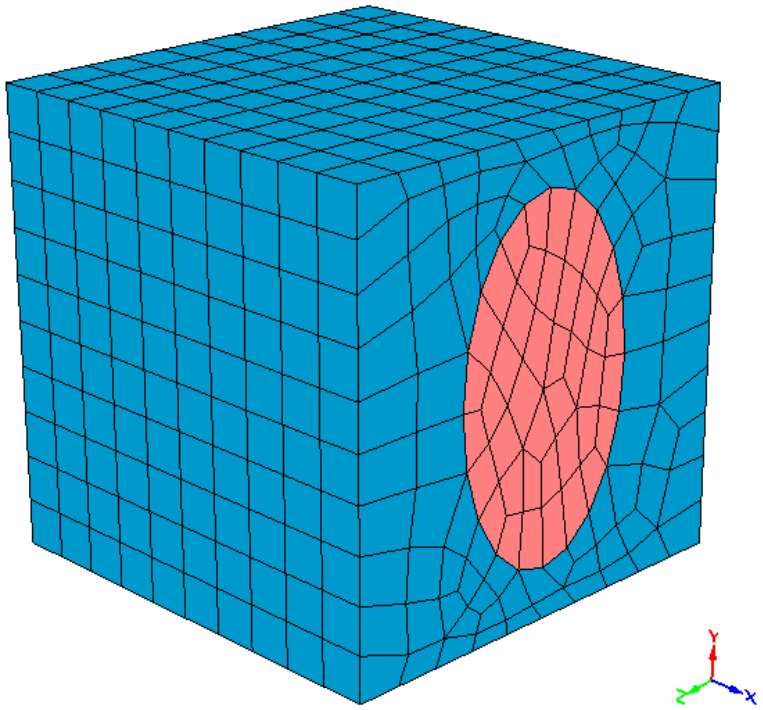

Figure 21 Microscale optimal solution

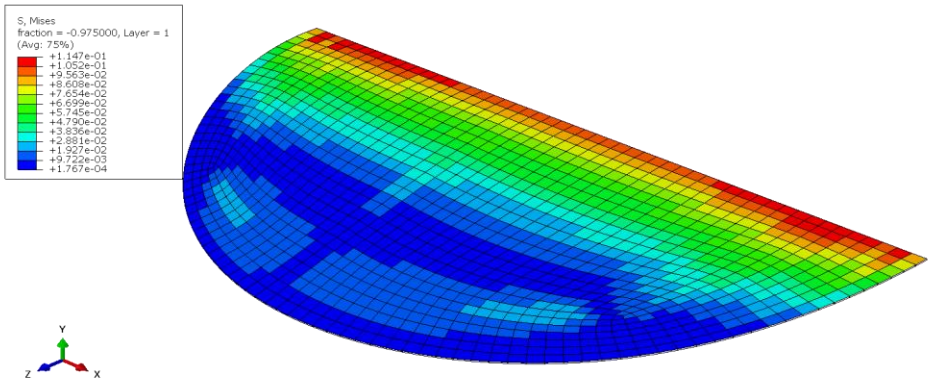

Figure 22 Initial shape and Von Mises stress in layer 1 prior to optimization

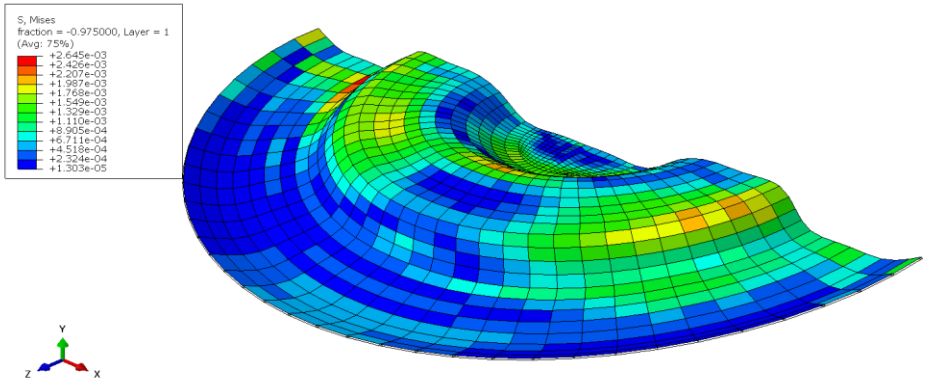

Figure 23 Optimized shape and Von Mises stress in layer 1

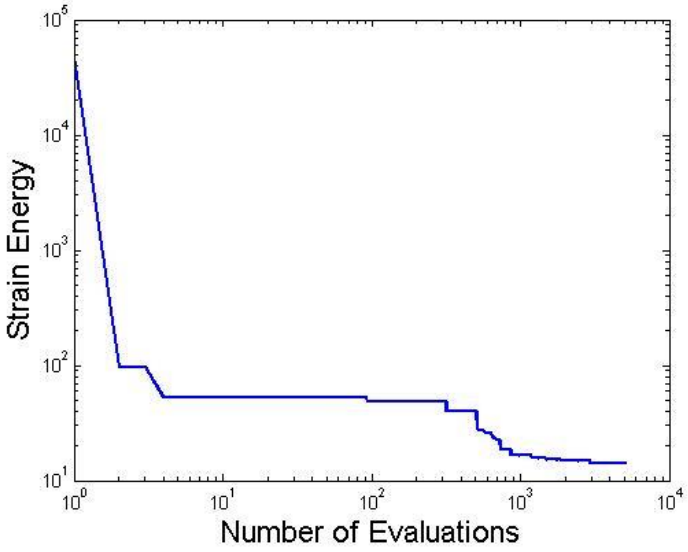

Figure 24 Evolution of objective function with number of samples for semi-circular laminated composite plate

2.6.2 Inelastic Rectangular Laminated Composite Plate

Consider an inelastic rectangular laminated composite plate of length of 100.0mm, width 40.0mm, and thickness 0.4mm depicted in Figure 25. The two ends of the plate are fixed and pressure of 20 kN/m^2 is applied on its top surface.

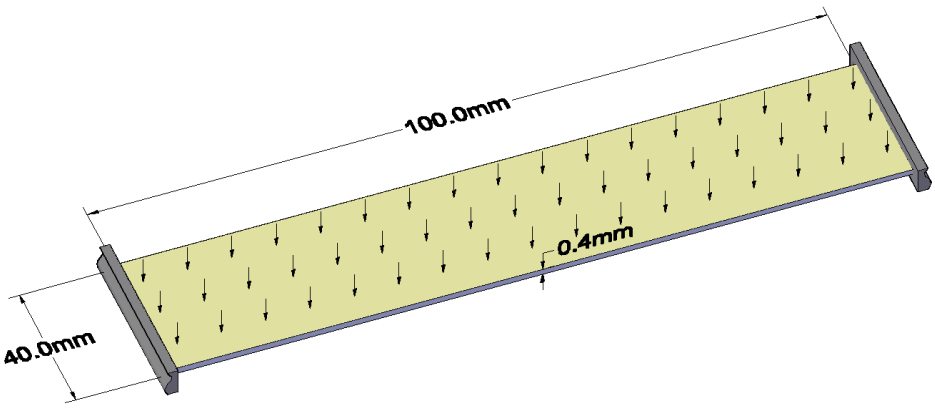

Figure 25 Geometry, loading and boundary conditions of the rectangular laminated plate

The objective is to minimize the average deflection d_{avg} of the plate.

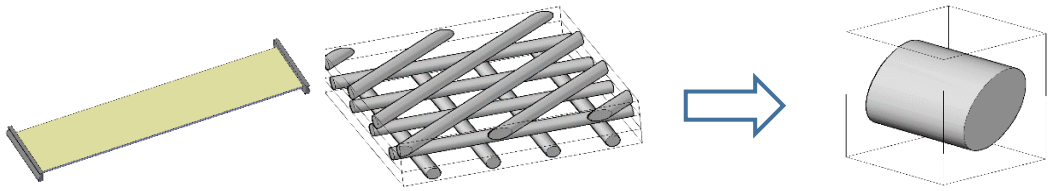

Phase 1: Macroscale-mesoscale Phase 2: Microscale

Figure 26 Two-phase optimization of the inelastic rectangular laminated composite plate

Both matrix and fabric are assumed to obey bilinear form of isotropic damage evolution law. The stress-strain relationship is expressed as

$$\sigma_{ij} = (1-w) L_{ijkl} \varepsilon_{kl} \tag{17}$$

where w is damage state variable in the range of [0, 1]. $w = 0$ represents the state without damage while $w = 1.0$ corresponds to total damaged. For numerical stability, the upper bound of w is chosen to be 0.9999.

The bilinear damage state variable is defined as

$$w = \begin{cases} 0 & \hat{\varepsilon} \le \hat{\varepsilon}^0 \\ G(\hat{\varepsilon}) w_{\max} & \hat{\varepsilon}^0 < \hat{\varepsilon} \le \hat{\varepsilon}^1 \\ w_{\max} & \hat{\varepsilon} > \hat{\varepsilon}^1 \end{cases} \tag{18}$$

where $\hat{\varepsilon}^0$ and $\hat{\varepsilon}^1$ represent the strains at which damage initiates and totally damaged, respectively. $G(\hat{\varepsilon})$ is given by

$$G(\hat{\varepsilon}) = \frac{a}{\hat{\varepsilon}} + b \tag{19}$$

where

$$a = \frac{1}{\frac{1}{\hat{\varepsilon}^1} - \frac{1}{\hat{\varepsilon}^0}}; b = \frac{-a}{\hat{\varepsilon}^0} \tag{20}$$

$\hat{\varepsilon}$ is the equivalent strain defined as

$$\hat{\varepsilon} = \sqrt{\sum_{I=1}^{3} \langle \varepsilon_I \rangle^2} \tag{21}$$

where

$$\langle x \rangle = \begin{cases} x & x \ge 0 \\ Cx & x < 0 \end{cases} \tag{22}$$

e_I is the principle strain and $C \in [0,1]$ is compression factor describing different behavior in tension and compression. A nonlinear three-scale analysis has been conducted using reduced order homogenization [4, 5, 7, 10, 77].

Table 8 summarizes the damage model parameters.

Table 8 Material property for Plate 2

Phase	E (GPa)	ν	ε^0	ε^1	C
Matrix	3.14	0.18	0.01	0.02	1.0
Fiber	233.0	0.1	0.01	0.02	1.0

As in the previous composite plate problem, we employ a two-phase optimization procedure described in the previous example.

The geometry of the plate is defined by 11 control points along its shorter cross-section as shown in Figure 27. The control points are limited to move in the out-of-plane direction and are connected by spline. By extruding the cross-section, the geometry of the plate is fully defined. The control points are bounded by [-3.0, 3.0]. At the mesoscale and microscale the design variables are the same as for the semi-circular plate considered in Section 5.1.

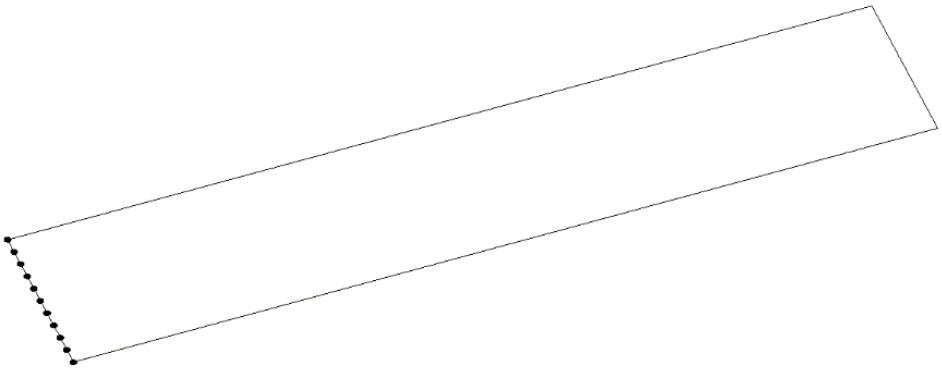

Figure 27 Macroscale design variables (control points) for the inelastic rectangular laminated composite plate

The evolution of the objective function with number of samples is illustrated in Figure 30. The initial shape of the plate is assumed to be flat with initial layup of

[45,45,45,45,45,45,45,45,45,45]. Figure 28 and Figure 29 depict the deflection prior and after the optimization, respectively. The optimal values of control points is [3.0, 3.0, -3.0, -3.0, 3.0, 3.0, -3.0, -2.91, 3.0, -2.75, -2.75] and the optimal layup is [-72.97, 79.38, 58.85, -57.67, 72.89, -89.13, 73.32, 90.0, 79.76, 32.80]. The optimal value of the stretch ratio is 0.7 and the stretch angle is 0. The microstructure optimization provides 7% decrease in the value of objective function. The average deflection decreases from 14.4 m from the initial value to 0.0251 m as a result of optimization.

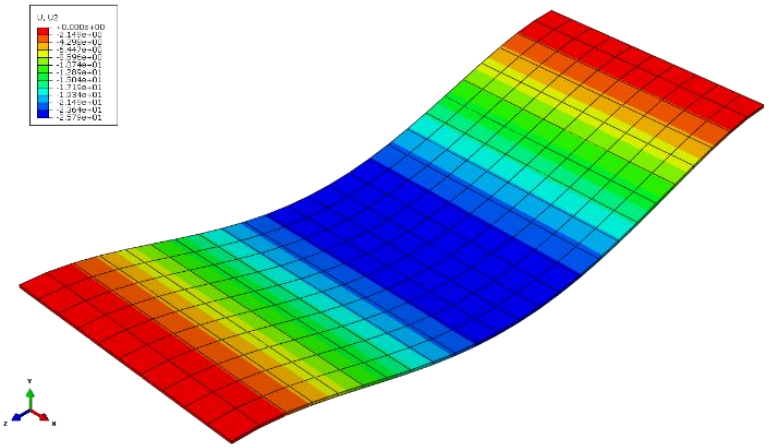

Figure 28 Shape and deflection contours for the rectangular laminated composite plate prior to optimization

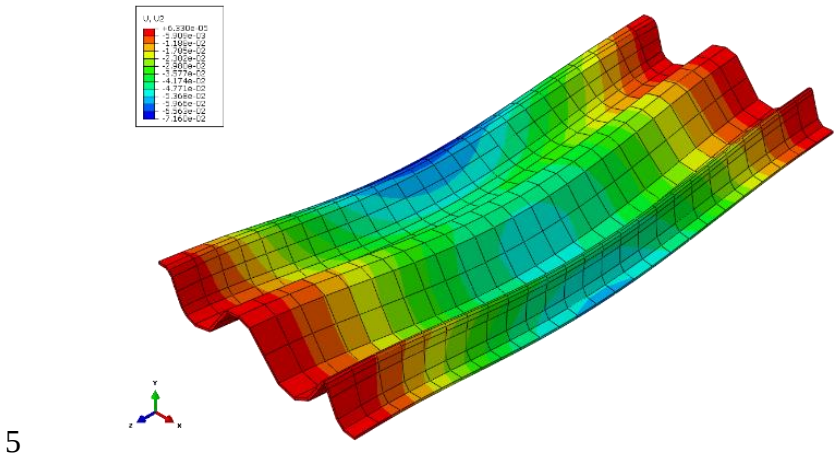

5

Figure 29 Shape and deflection contours for the optimized rectangular laminated composite plate

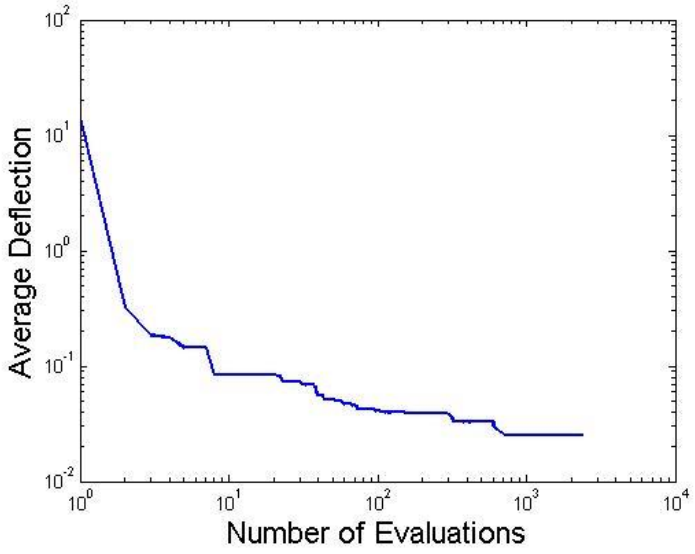

Figure 30 Evolution of objective function with number of samples for rectangular laminated composite plate

Chapter 3

An Adaptive Nonintrusive Stochastic Inverse Solver for Multiscale Characterization of Composite Materials

In this chapter, we present an adaptive variant of the measure-theoretic approach (MTA) for stochastic characterization of micromechanical properties based on the observations of quantities of interest at the coarse (macro) scale. The salient features of the proposed nonintrusive stochastic inverse solver are: identification of a nearly optimal sampling domain using enhanced ant colony optimization algorithm for multiscale problems, incremental Latin-hypercube sampling method, adaptive discretization of the parameter and observation spaces, and adaptive selection of number of samples. A complete test data of the TORAY T700GC-12K-31E and epoxy #2510 material system from the NIAR report is employed to characterize and validate the proposed adaptive nonintrusive stochastic inverse algorithm for various unnotched and open-hole laminates.

3.1 Problem Definition

A typical two-scale problem is depicted in Figure 31 where x and y denote the macroscale and microscale coordinate systems, respectively. Making the usual assumption of scale separation, the two coordinates satisfy the following relationship: $x = y / z$, and $0 < z = 1$.

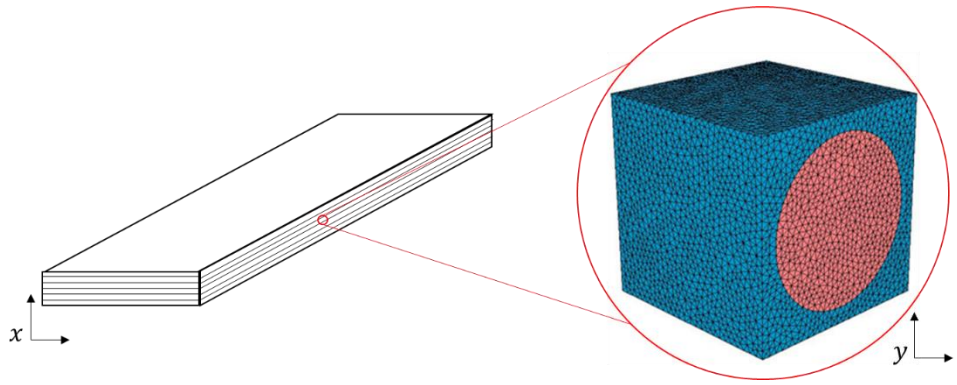

Figure 31 Two-scale problem

Let $\boldsymbol{\lambda}$ be model parameters in the parameter space $\Lambda \subset \mathbb{R}^d$, typically describing microstructural geometry and material parameters of microconstituents. The quantities of interest (QoI) denoted by $\boldsymbol{q}$ in the observation space D are typically defined at the macroscale. $\boldsymbol{q}(\boldsymbol{\lambda})$ is assumed to be a smooth implicit function of $\boldsymbol{\lambda}$. In a deterministic two-scale inverse problem, we seek for the microscale model parameters $\boldsymbol{\lambda}$ given the macroscale observables $\boldsymbol{q}(\boldsymbol{\lambda})$.

We now consider the forward and inverse stochastic problems. Due to the natural variability of composite material properties at the scale of microconstituents, the macroscopic response may vary considerably. Hence, both $\boldsymbol{\lambda}$ and $\boldsymbol{q}$ may be considered random variables. Let $s_{\mathrm{L}}(\boldsymbol{\lambda})$ be the (joint) probability density function of $\boldsymbol{\lambda}$, and $P_D(\boldsymbol{q})$ the (joint) probability distribution of $\boldsymbol{q}$. Using the so called the *Law of Total Probability*, we have

$$P_D(\boldsymbol{q}) = \int_{\Lambda} L(\boldsymbol{q}\,|\,\boldsymbol{\lambda})\,\sigma_{\Lambda}(\boldsymbol{\lambda})\,d\mu_{\Lambda}(\boldsymbol{\lambda}) \tag{23}$$

where $L(\boldsymbol{q}\,|\,\boldsymbol{\lambda})$ is the likelihood function of the observables $\boldsymbol{q}$ given the microscopic parameters $\boldsymbol{\lambda}$; $L(\boldsymbol{q}\,|\,\boldsymbol{\lambda})$ is the unit mass distribution at $\boldsymbol{q} = \boldsymbol{q}(\boldsymbol{\lambda})$; $\mu_\Lambda(\boldsymbol{\lambda})$ is the parameter volume measure on Λ. For an *n*-dimensional parameter space, $d\mu_\Lambda(\boldsymbol{\lambda})$ is given by

$$d\mu_\Lambda(\boldsymbol{\lambda}) = d\lambda_1 \cdot d\lambda_2 \cdots d\lambda_n \tag{24}$$

Eq.(23) defines the forward stochastic problem. This forward problem is often solved using a Monte Carlo approach where: (i) random parameter sample values $\boldsymbol{\lambda}$ are drawn from the distribution $s_{\mathrm{L}}(\boldsymbol{\lambda})$ on the parameter space; (ii) corresponding values of $\boldsymbol{q}(\boldsymbol{\lambda})$ are computed; and (iii) these values are binned to produce an approximate probability distribution in the observation space.

The inverse stochastic problem, i.e. inversion of Eq.(23), consists of finding probability distribution $\sigma_\Lambda(\boldsymbol{\lambda})$ given the probability distribution $P_D(\boldsymbol{q})$.

3.2 Measure-theoretic Method for Stochastic Inverse Problem

Consider a general deterministic inverse problem depicted in Figure 32. We denote the union of solutions in the parameter space as a *general contour* (solid circle in the parameter space). Note that each observation in the observation space has a general contour in the parameter space and that no two general contours intersect. Thus, it is feasible to transform the probabilistic information from the observation space D to the parameter space Λ (Figure 33a). Qualitatively, given the probability distribution of observations, we could find the corresponding density of the general contours. Higher probability of observations gives rise to denser general contours. For instance, the blue region in parameter space depicted in Figure 33b, corresponds to the highest probability in the observation space.

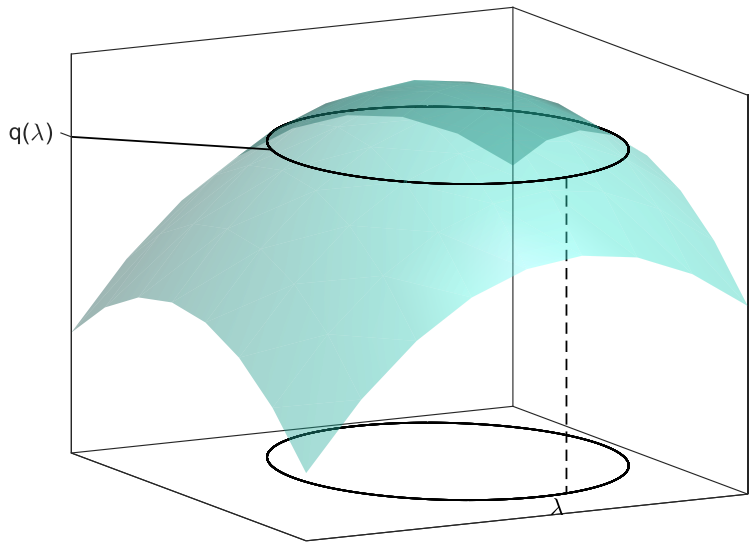

Figure 32 A general inverse problem with multiple solutions

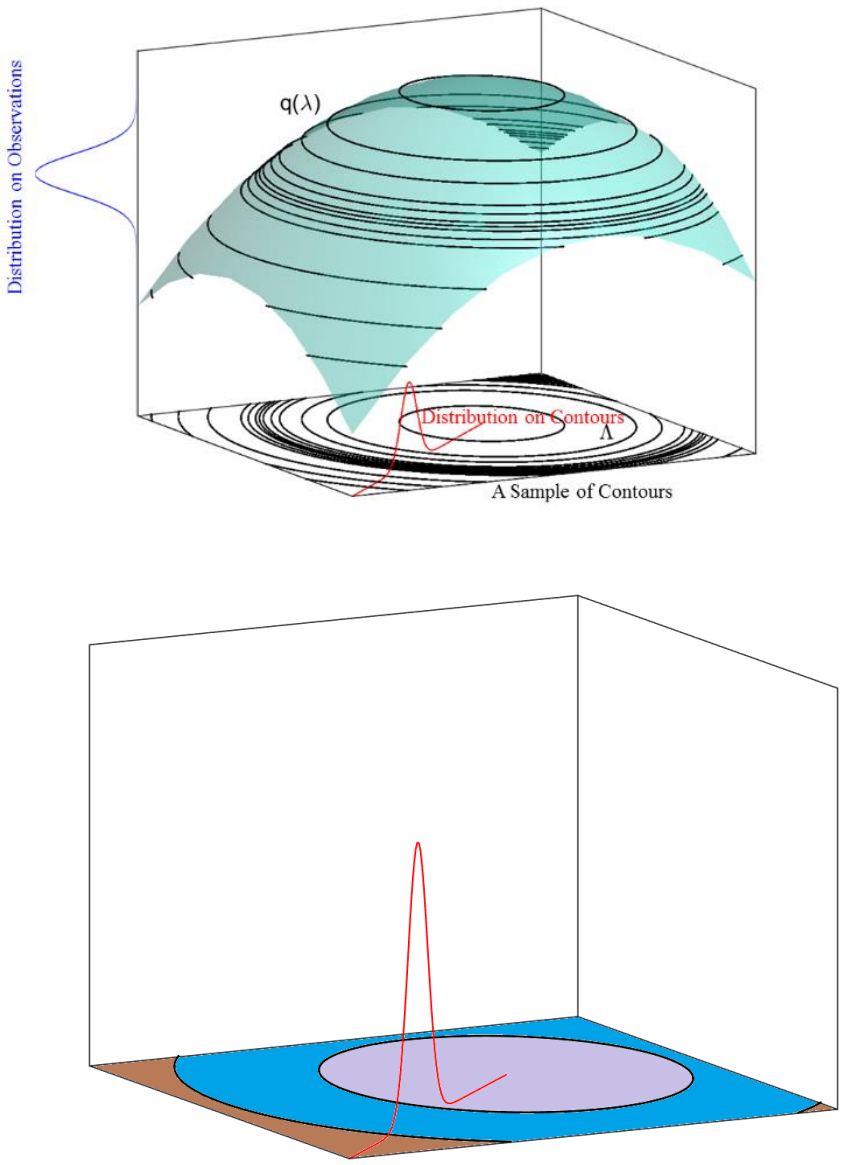

Figure 33 Transformation of statistical information from the observation space to parameter space

To quantify the probability transformation from the observation space to the parameter space, it is necessary to discretize the two spaces. Figure 34 illustrates how the statistical information is transferred from the one-dimensional observation space to the

two-dimensional parameter space, which is uniformly discretized into 81 cells. Colors in Figure 4 in the two spaces denote corresponding solution map. For instance, model parameters corresponding to the blue region give rise to the observations corresponding to the blue region in the observation space. Thus the probability corresponding to the blue interval in the observations space should be divided among all blue cells in the parameter space. For problems with multiple dimensions in the observation space, the observation space is partitioned in multiple dimensions. In the limit, as the cell size in both spaces is reduced, the numerical solution converges to the exact solution [84, 85].

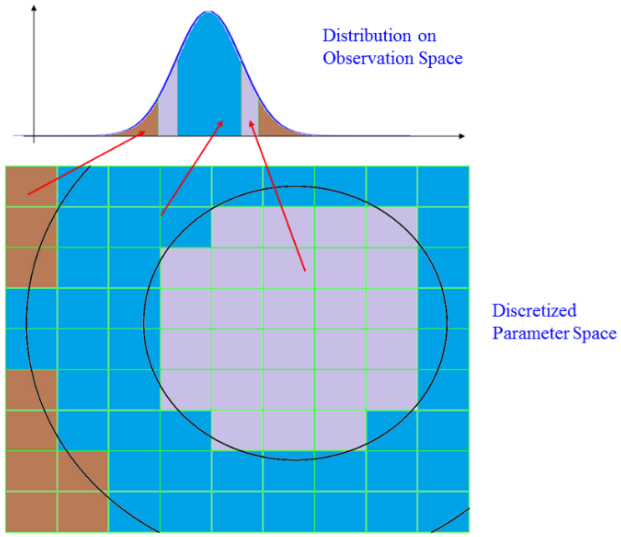

Figure 34 Transfer statistical information from the discretized observation space to the uniformly discretized parameter space

The discretization of the parameter space is defined by the Voronoi tessellation of the parameter samples into M cells, denoted as b_i for $i = 1, M$. The observation space is likewise discretized (typically uniformly) into cells Q_i with $i = 1, N$ where N is the total number of cells in discrete observation space. The measure-theoretic method approximates

the inverse of Eq. (23) with a piecewise constant probability $P(b_i)$ computed for each cell in $\mathbf{L}$ as

$$P(b_i) = P_D(Q_k) \frac{\mu_{\mathbf{L}}(b_i)}{\sum_{j=1}^{M} \mu_{\mathbf{L}}(b_j) \delta_{Q_k}(b_j)} \tag{25}$$

where $\mu_{\mathbf{L}}(b_i)$ is the parameter volume measure. The observation space cell Q_k associated with parameter space cell b_i is given by solving the forward problem $\boldsymbol{q}(b_i)$ and locating the cell Q_k such that $q(b_i) \in Q_k$. Further, $\delta_{Q_k}(b_j)$ is defined as

$$\delta_{Q_k} = \begin{cases} 1 & \text{if } q(b_j) \in Q_k \\ 0 & \text{otherwise} \end{cases} \tag{26}$$

Since the forward problem is unique, $\boldsymbol{q}(b_i)$ can only map to one observation space cell Q_k . However since the inverse problem is generally set valued, there may be many parameter space cells b_i which map to the same observation space cell. In (25), the term $\mu_{\mathbf{L}}(b_i) \Big/ \sum_{j=1}^{M} \mu_{\mathbf{L}}(b_j) \delta_{Q_k}(b_j)$ represents the ratio of the volume of parameter space cell b_i to the total volume of all the parameter space cells which also map to observation space cell Q_k . Therefore, (25) distributes the probability of cell Q_k its associated parameter space cells in accordance with their volume. This requires explicit computation of Voronoi tessellation of the parameter space so that the volumes of each cell can be computed. This step may be circumvented if it is assumed that all of the parameter space cells have the same volume. Equation (3) becomes

$$P(b_i) = \frac{P_D(Q_k)}{\sum_{j=1}^{M} \delta_{Q_k}(b_j)} \tag{27}$$

This equation simply divides the probability of cell Q_k equally amongst all the parameter space cells that map to it.

While providing a significant algorithmic simplification, this assumption may lead to errors for nonuniform sampling methods where the volumes of parameter space cells are not necessarily the same. Criteria are proposed in the next section to ensure that the discretized parameter and observation spaces lead to the converged probability distributions.

The Algorithm 1 describes the measure-theoretic method with uniform partitions.

Algorithm 2 Measure-theoretic inverse solution algorithm with uniform discretization

---

i. Discretize the *n*-dimension observation space into *N* cells

$$I_j = \left[q_j^1, q_{j+1}^1\right] \times \left[q_j^2, q_{j+1}^2\right] \times \cdots \times \left[q_j^n, q_{j+1}^n\right] \quad j = 1, \ldots, N$$

ii. Compute the probability of each cell I_j, $p_j = p_D\left(I_j\right)$

iii. Partition the parameter space into *M* equal-size cells ($b_i, i = 1, \ldots, M$)

iv. Sample over all cells ($\boldsymbol{l}_i$, $i = 1, \ldots, M$) with $\boldsymbol{l}_i$ denoting the centroid of the cell

v. Evaluate $\boldsymbol{q}\left(\lambda_i\right)$ for each cell b_i

vi. Identify W_j samples that map to each interval I_j in observation space

vii. Use Eq.(27) to compute the probability of each cell $P\left(b_i\right)$ in the parameter space

---

3.3 An Adaptive Nonintrusive Stochastic Inverse Multiscale Solver

There are two challenges in effective realization of the measure-theoretic algorithm. The first, is the ability to ensure solution accuracy. What is the necessary discretization that satisfies the user-defined accuracy needs? The second challenges, is choosing a nearly optimal parameter space rather than sampling in the infinite space.

To address the aforementioned challenges, we propose an adaptive nonintrusive stochastic inverse multiscale solver incorporating the measure-theoretic algorithm with incremental Latin-hypercube sampling (iLHS) and optimal parameter subspace identification. Figure 35 summarizes the major steps in the adaptive MTA algorithm. Various elements of the algorithm are detailed in the following subsections.

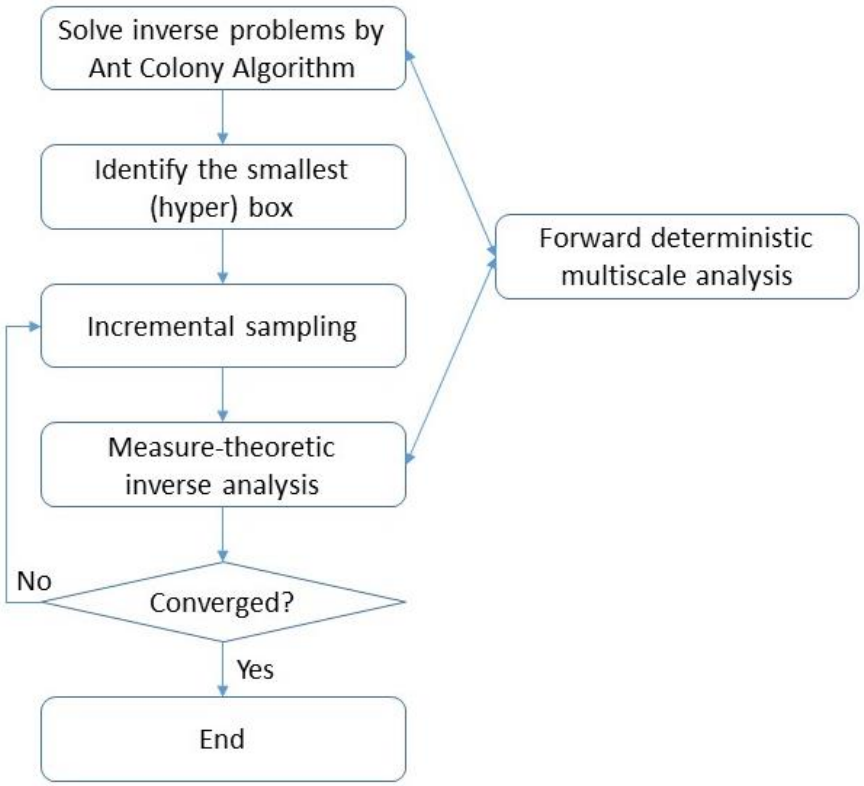

Figure 35 Adaptive Nonintrusive Stochastic Inverse Algorithm

3.3.1 Latin-hypercube Sampling

Latin-hypercube sampling (LHS) was proposed by McKay [147], Eglājs [148] and Iman [149]. To get N samples, LHS creates sampling grid by dividing each parameter dimension into N intervals. In each interval, a random value would be picked. Then samples are obtained by combing the values in a way that there is only one sample in each parameter interval. Figure 36 schematically illustrates LHS with 3 and 4 samples for a 2-dimensional domain.

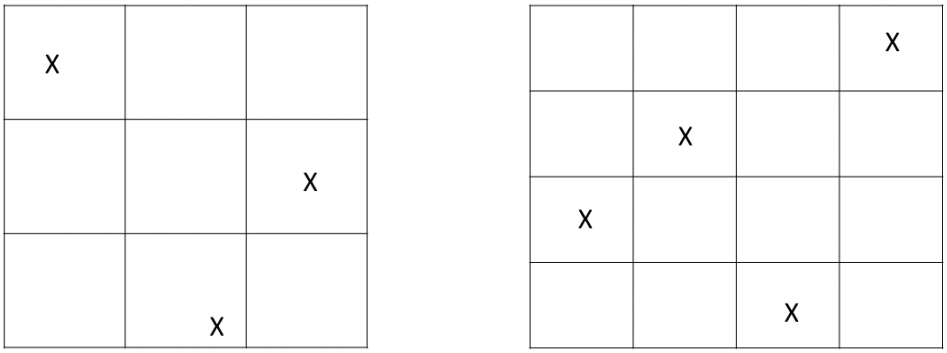

Figure 36 Latin-hypercube sampling

3.3.2 Incremental Sampling with LHS

When analyzing a problem with large number of parameters, it is necessary to keep the population of samples as small as possible without sacrificing on solution accuracy. This can be accomplished with incremental sampling that reuses previous samples. One of the obvious choices is to use Monte Carlo Sampling (MCS) [150]. However, MCS may encounter the situation where samples cluster, which may lead to the measure-theoretic algorithm providing biased solutions. We propose to employ the incremental Latin Hypercube Sampling (iLHS) method [151], which is a derivative of the Latin Hypercube Sampling proposed by Conover [147, 152], that reuses previous samples. The iLHS doubles the number of samples each sampling iteration until the convergence criteria are met.

To construct n samples in the d-dimension parameter space $\mathbf{L}$, the iLHS divides each dimension in parameter space into n intervals which do not overlap. This process is referred to as "stratification". One sample is randomly selected in each stratification. The cumulative probability P_i for sample i is computed as [86]

$$P_i = \frac{r+i-1}{n} \tag{28}$$

where r is uniformly distributed random number ranging between 0 and 1. Given P_i, the value of λ is computed using the inverse of the distribution function

$$\lambda = f_P^{-1}(P_i) \tag{29}$$

where $f_P(x)$ is the cumulative probability function.

Then the n samples are selected as a combination of values from each dimension in a random manner with the condition that there is only one sample in each interval in each dimension. Figure 37 depicts an example of 64 samples being incrementally added in a 1 by 1 two-dimensional space with 6 iterations.

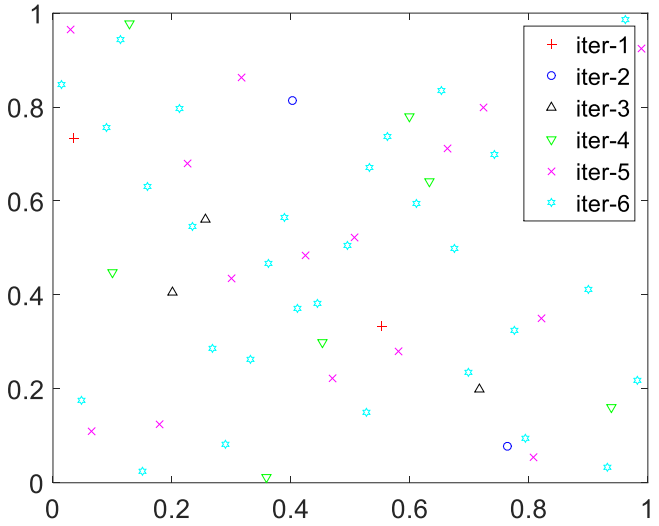

Figure 37 iLHS sampling with 64 samples over a 1 by 1 space

3.3.3 Nearly Optimal Parameter Subspace

Identifying a nearly optimal subspace Λ_{opt} that would contain all the necessary cells in the parameter space, is of outmost importance to minimize computational cost.

To illustrate the process, consider a model problem having one-dimensional observation space and two-dimensional parameter space as shown in Figure 38. Assume

the observation q follows normal distribution with the mean value μ and the standard deviation σ as shown in Figure 38a. Assuming truncated normal distribution, the bounds in the observation space, q_1 and q_2, are defined as $\mu-3\sigma$ and $\mu+3\sigma$, respectively. For other distributions, such as lognormal or Weibull, the bounds could be defined as $q_1=\mu-\alpha\sigma$ and $q_2=\mu+\beta\sigma$ where $\alpha>0$ and $\beta>0$ depend on the type of distribution.

Given the values of q_1 and q_2, we carry out a deterministic inverse analysis using a variant of the Ant Colony algorithm [34]. The multiplicity of inverse solutions (two in the present model problem) are summarized in .

Table 9 and Figure 38. The nearly optimal sampling space, Λ_{opt}, highlighted as a red box in Figure 38(b), is defined as

$$\Lambda_{\text{opt}}=\left[\lambda_1^1,\lambda_1^4\right]\otimes\left[\lambda_2^1,\lambda_2^4\right] \tag{30}$$

In more than two-dimensional parameter space, Λ_{opt} is defined by

$$\Lambda_{\text{opt}}=\left[\lambda_1^L,\lambda_1^U\right]\otimes\left[\lambda_2^L,\lambda_2^U\right]\otimes\cdots\otimes\left[\lambda_n^L,\lambda_n^U\right] \tag{31}$$

where *n* is the number of independent model parameters and λ_n^L,λ_n^U are the lower and upper bounds of the solutions on a parameter dimension *n*.

Table 9 Deterministic solutions

Observations	Solution 1	Solution 2
q_1	$(\lambda_1^1,\lambda_2^2)$	$(\lambda_1^2,\lambda_2^3)$
q_2	$(\lambda_1^3,\lambda_2^1)$	$(\lambda_1^4,\lambda_2^4)$

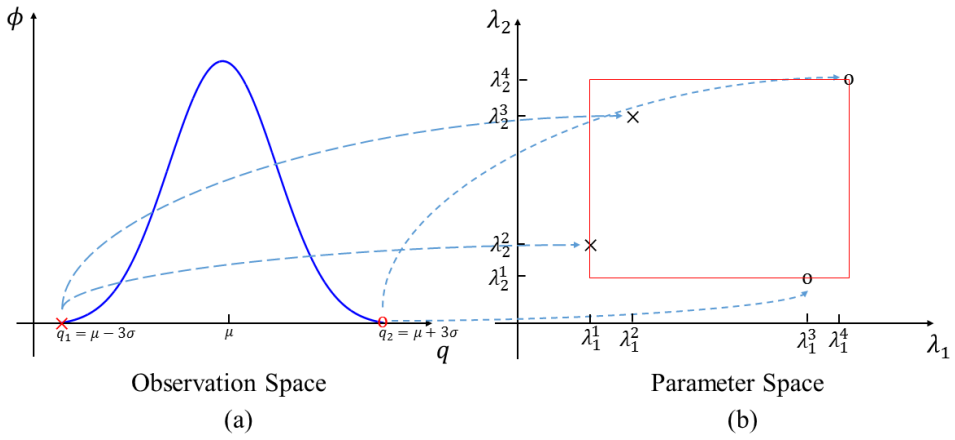

Figure 38 Identification of nearly optimal parameter space Λ_{opt} shown in red box. Truncated normal distribution is considered in this study

3.3.4 Convergence Criteria

The measure-theoretic inverse algorithm is deemed to converge when the following criteria are met. First, the cumulative probability function should be equal or close to 1

$$1-\sum_{i=1}^{M_k} P_k\left(b_i\right) \le tol_1 \tag{32}$$

where M_k is number of cells in the parameter space for sampling iteration k, b_i is a cell in the parameter space, $P_k\left(b_i\right)$ is the probability of cell b_i in the k^{th} iteration and tol_1 is a user-defined tolerance.

The second criterion is aimed at ensuring that the ratio between the number of samples and the number of observation cells is sufficiently large. With a piecewise constant discretization of probability distribution in the parameter space, as samples are added the change in probability density in each cell should be controlled by the user-defined tolerance tol_2

$$\sqrt{\sum_{i=1}^{n}\sum_{j=1}^{m_i}\left|P_k\left(B_j^i\right)-P_{k-1}\left(B_j^i\right)\right|^2} \le tol_2 \tag{33}$$

where n is the number of dimensions in the parameter space, m_i is the number of intervals of i^{th} parameter dimension; B_j^i is the j^{th} interval on i^{th} parameter dimension; $P_k\left(B_j^i\right)$ is the probability of B_j^i in the k^{th} iteration of iLHS.

The final criterion is aimed at testing the discretization of the observation space. This is accomplished by using the following predictor-corrector algorithm. At the end of each sampling iteration, the MTA is performed twice and the difference in the mean and the standard deviation of each parameter is evaluated. The difference should be smaller than the user-specified tolerance as described in Eq. (34) and Eq. (35) below

$$\left|\mu_i' - \mu_i\right| < tol_3 \tag{34}$$

$$\left|\sigma_i' - \sigma_i\right| < tol_4 \tag{35}$$

where μ_i and σ_i are the mean and standard deviation of parameter i in the observation space in the predictor step; μ_i' and σ_i' are the corresponding measures in the corrector step when the number of observation cells is doubled.

3.4 Numerical Studies

In this section, we evaluate the performance of the adaptive nonintrusive inverse stochastic multiscale solver using the data reported by Tomblin et al. [88], hereafter referred as the NIAR report. A nonlinear two-scale analysis has been conducted using the reduced order homogenization method [4, 5, 7, 10, 77]. For validation, a nonintrusive stochastic multiscale solver [75] based on the sparse grid collocation approach [76, 153] is employed.

3.4.1 Composite Material Micro Geometry

The NIAR report describes the nominal ply thickness as 0.1524 mm and the fiber volume fraction to be proportionally varying with the thickness of the laminate from 0.45 to 0.65. For simplicity, we neglect the uncertainty introduced by the fiber volume fraction and ply thickness; both are assumed to be deterministic, 0.55 and 0.1524 mm, respectively. Figure 39 depicts the finite element mesh of the representative volume element (RVE) with fiber volume fraction of 0.55.

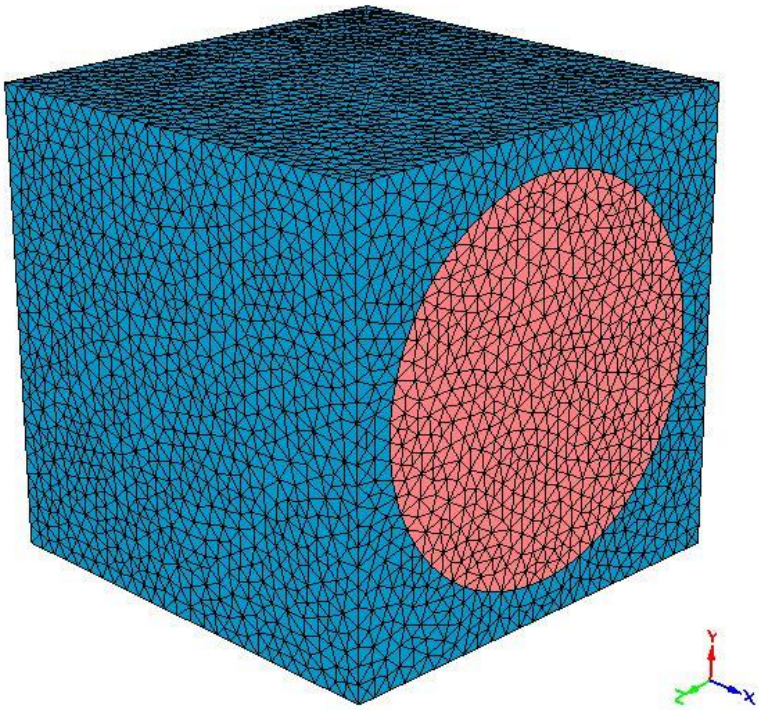

Figure 39 Representative volume element

3.4.2 Deterministic Inverse Analysis of Linear Properties

Fibers considered in this study are that of TORAY T700GC-12K-31E whereas the matrix is Epoxy #2510. The composite physical properties are listed in Table 10. Table 10 lists also the standard deviation (SD) of the linear properties, which is considerably smaller than that of nonlinear properties given in Table 15.

Table 15. Consequently, uncertainty in the elastic properties is neglected in the present study. The matrix and fiber phases are assumed to be isotropic and transversely isotropic, respectively. The elastic properties of microconstituents have been deterministically calibrated to yield the overall elastic properties listed in Table 2 with an error of less than 0.1%. Using the published microconstituent properties in [154] as an initial guess, elastic properties of microconstituents have been deterministically calibrated to yield the overall elastic properties listed in Table 2 with an error of less than 0.1%. The calibrated elastic properties of microconstituents are summarized in Table 11 and Table 12.

Table 10 Composite elastic properties

Direction	Modulus (GPa)	Standard Deviation (GPa)
11	126.0	1.943
22	8.0	0.191
12	4.0	0.231

Table 11 Matrix elastic properties

Young's Modulus	Poisson's Ratio
2.764	0.169

Table 12 Fiber elastic properties

Young's Modulus (Transverse)	Young's Modulus (Axial)	Poisson's ratio (Transverse)	Poisson's ratio (Axial)	Shear modulus (Axial)
34.465	225.987	0.1	0.1	34.885

3.4.3 Nonlinear Deterministic Inverse Analysis

We assume bilinear form of continuum damage mechanics model for both matrix and fiber phases at the microscale [155] . The isotropic bilinear damage model, which is used for matrix phase, has four independent material constants including two deterministic elastic parameters listed in Table 13.

Table 13 Isotropic bilinear damage model parameters

E	Young's Modulus
ν	Poisson's Ratio
σ^0	stress at damage initiation
ε^1	failure strain

For the fiber phase, the orthotropic damage mechanics model is employed [155].

Table 14 lists nine independent material parameters for the orthotropic bilinear damage model including five deterministic elastic material parameters that have been identified in Table 12.

Table 14 Orthotropic bilinear damage model parameters

E_T	Young's Modulus in transverse direction
E_A	Young's Modulus in axial direction
ν_T	Poisson's Ratio in transverse direction
ν_A	Poisson's Ratio in axial direction
G_A	Shear Modulus in axial direction
σ_T^0	stress at damage initiation in transverse direction
ϵ_T^1	failure strain in transverse direction
σ_A^0	stress at damage initiation in axial direction
ϵ_A^1	failure strain in axial direction

The inelastic deterministic analysis was performed with FOOF [155, 156] as a macro-solver and Multiscale Designer[1] [11, 157] as micro-solver.

The NIAR report [88] provides the mean and standard deviation of strength in different directions, which are summarized in Table 15.

Table 15 Composite inelastic properties

Direction	Strength (MPa)	
	Mean	Standard Deviation
11	2172.443	165.844
22	48.857	4.101

[1] Formerly, Multiscale Design Systems (MDS, http://multiscale.biz/)

Given the composite inelastic properties, a deterministic inverse solver is employed to identify inelastic microconstituent parameters, which are summarized in Table 16.

Table 16 Calibrated matrix and fiber properties

Matrix Parameter	σ^0	0.031
	ϵ^1	0.015
Fiber Parameter	σ_T^0	0.65
	ϵ_T^1	0.02
	σ_A^0	3.93
	ϵ_A^1	0.022

3.4.4 Stochastic Inverse Analysis

Based on the sensitivity analysis, it has been observed that two inelastic parameters, σ_A^0 and σ^0, are the main parameters contributing to the uncertainty. Thus, we only consider uncertainty in the axial strength of the fiber σ_A^0 and the matrix strength σ^0, while remaining material parameters are assumed to be deterministic. We will demonstrate that this assumption produces reasonable predictions in the quantities of interest at the macroscale.

We start by determining Λ_{opt} as described in the previous section.

Table 17 lists the lower and upper bounds of the strengths at a coupon level along the fiber and transverse directions.

Table 17 Bounds in the observation space at a coupon level

Direction	Lower Bound (MPa)	Upper Bound (MPa)
11	1674.91	2669.96
22	36.55	61.16

By solving four deterministic inverse problems, the corresponding bounds in the parameter space are summarized in Table 18.

Table 18 Calibrated bounds in the parameter space

Parameter	Lower Bound (MPa)	Upper Bound (MPa)
σ_A^0	3015.0	4815.0
σ^0	23.6	39.6

Next, we carry out the measure-theoretic inverse analysis with 400 observation cells with samples added incrementally in the parameter space defined by $[3015.0, 4815.0] \otimes [23.6, 39.6]$. Realizations are generated using the iLHS. The probability distributions of σ^0 and σ_A^0 as obtained with 12800 samples in 12 intervals in each parameter dimension are given in Figure 40. Similarly, with 51200 samples in 15 intervals in each parameter dimension, the probability distributions are listed in Figure 41. Figure 42 shows that the error in the cumulative probability decreases with increase in the number of samples. Figure 43 shows that the solution stabilizes with increase in the number of samples. The convergence criterion 3 was verified by increasing the number of observation cells from 400 to 841; the mean and standard deviation for both parameters changed by less than 2.5%, which was deemed to be acceptable.

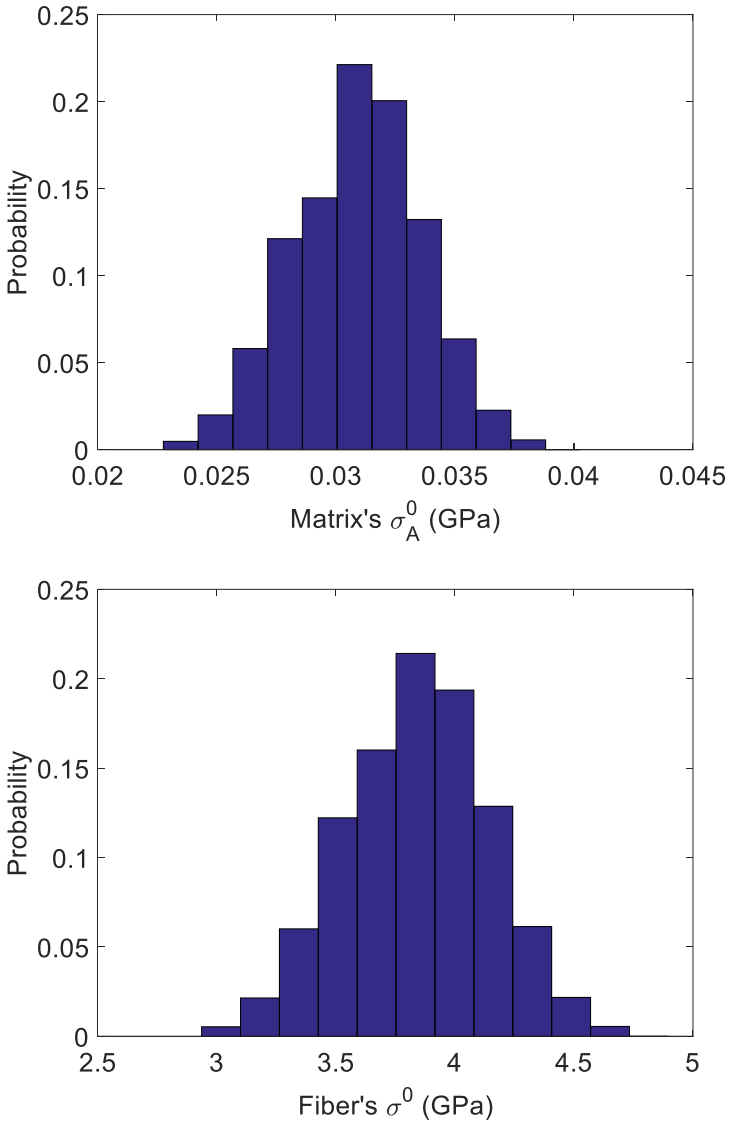

Figure 40 Probability distribution of material parameters with 12800 samples in 12 intervals

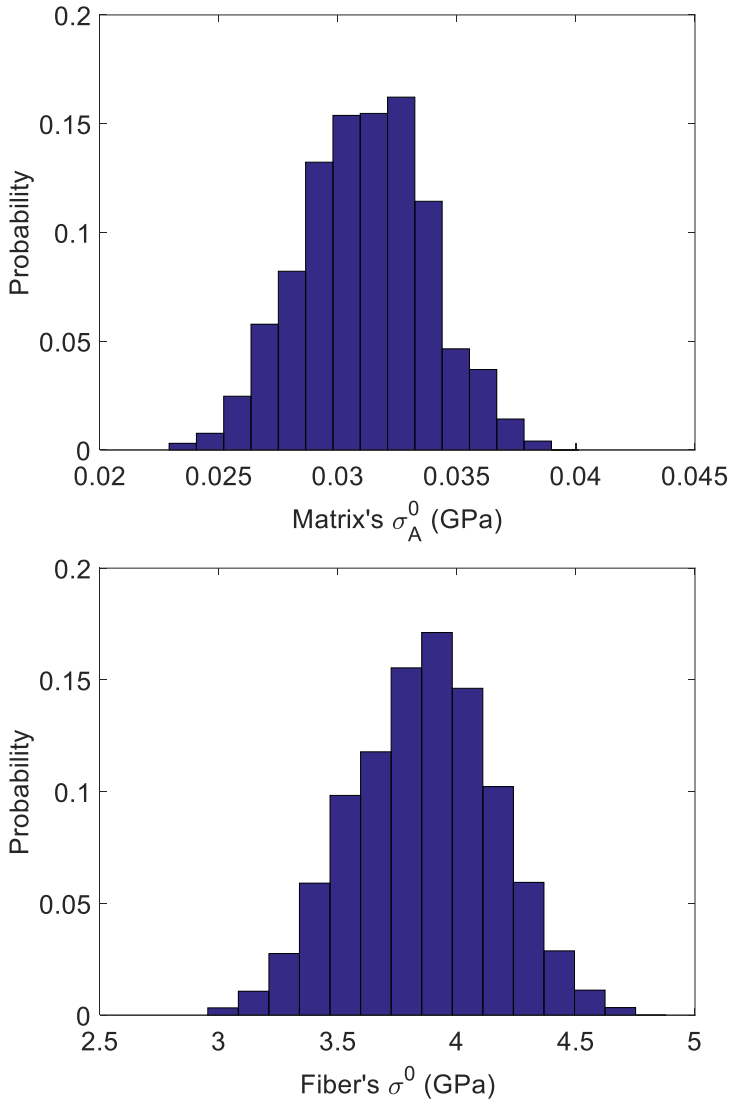

Figure 41 Probability distribution of material parameters with 51200 samples in 15 intervals

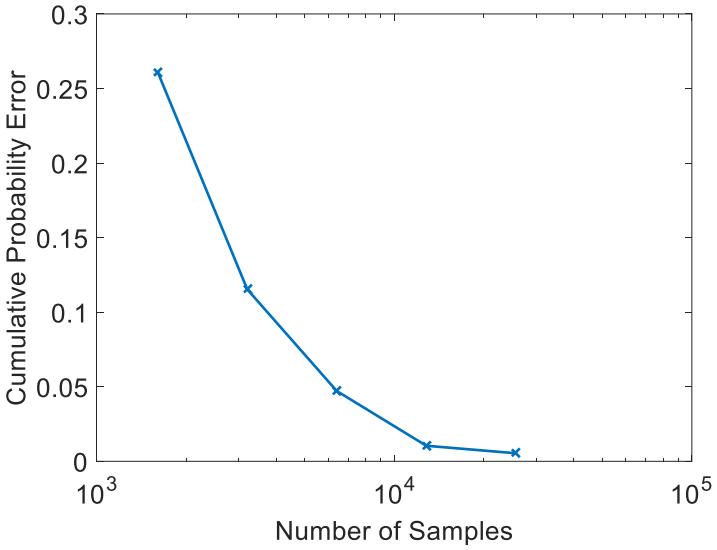

Figure 42 Cumulative probability error

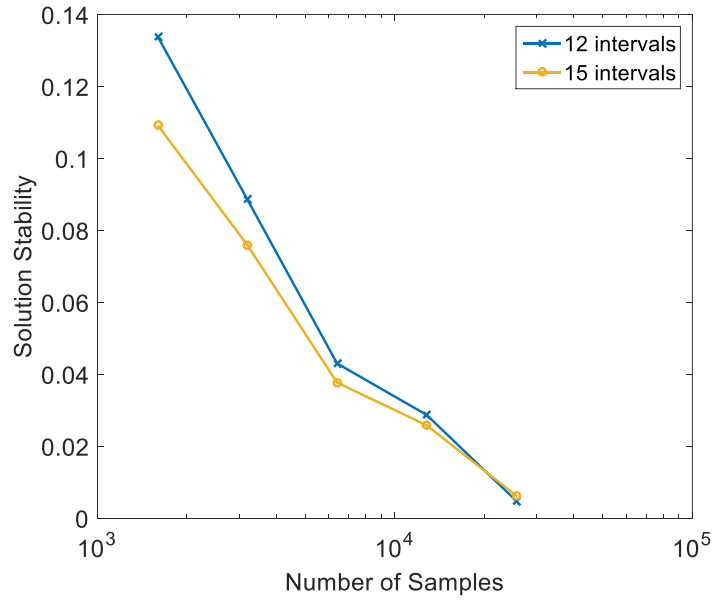

Figure 43 Solution stability index

3.4.5 Model Validation

To validate the model, we consider the unnotched tension test (UNT) and open hole tensile test (OHT) and compare the model predictions against experimental results from

the NIAR report [88]. We employ the nonintrusive stochastic multiscale solver [75] based on the sparse grid collocation approach [76, 153] with model parameters identified in the previous sections to predict the probability distribution of the strength in the unnotched tension test (UNT) and the open hole tensile test (OHT).

3.4.5.1 Lamina Test

705 realizations were performed with the forward stochastic multiscale solver [75]. The results are summarized in Table 19 and compared to the experiment results [88]. A good agreement has been observed.

Table 19 Lamina test results

Direction		Simulation	Experiment
11	Mean (MPa)	2.0947×10^3	2.1676×10^3
	CV (%)	7.666	7.634
22	Mean (MPa)	47.347	48.857
	CV (%)	8.612	8.394

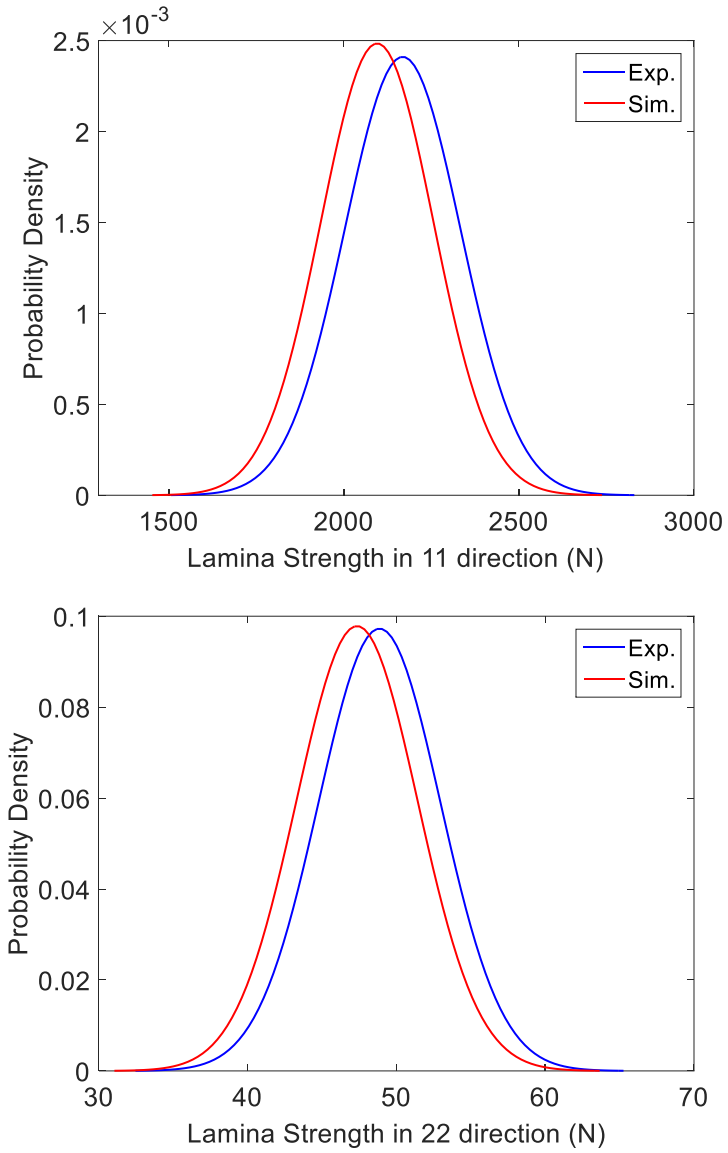

Figure 44 Lamina strength probability distribution: simulations versus experiment [88]

3.4.5.2 Unnotched Tensile (UNT) Laminate Test

Figure 45 depicts the geometry of the specimen consisting of 20 symmetric plies with the ply orientations $[45/0/-45/90/0/0/45/0/-45/0]_s$. This test measures the strength of the plate by fixing one end and pulling along the longitudinal direction at the other end.

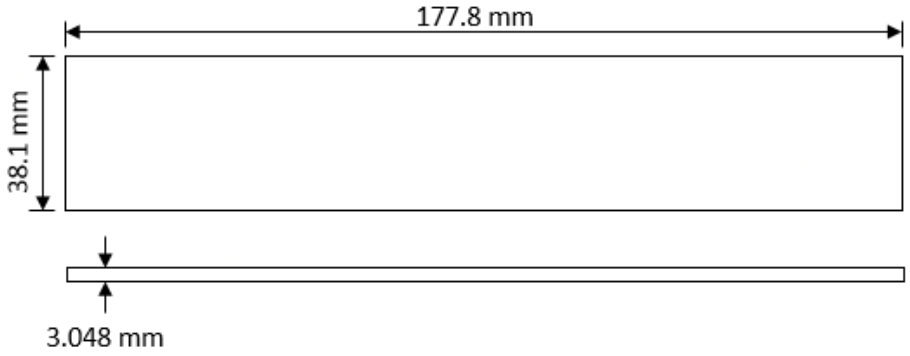

Figure 45 Unnotched tensile test specimen geometry

The finite element macro-model was constructed in FOOF [155, 156]. The finite element mesh consists of 36 twenty-node quadratic laminated elements in each of the 20 plies (Figure 46). To overcome the issue of convergence due to softening, an explicit algorithm in FOOF was employed.

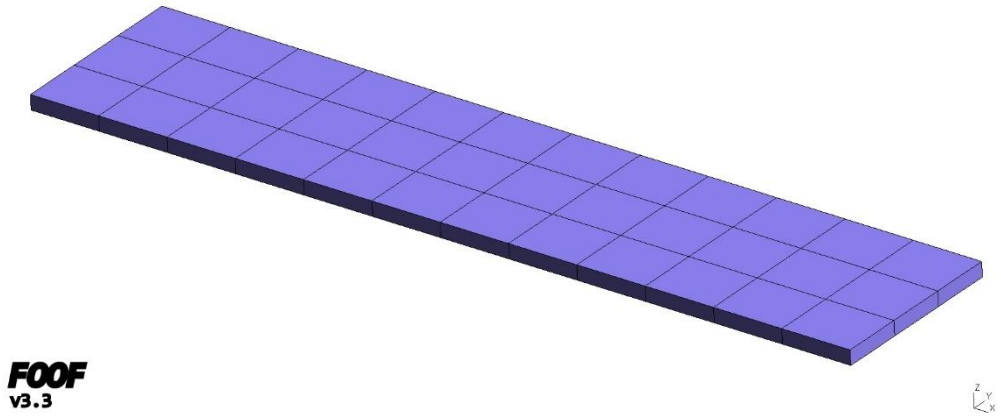

Figure 46 Finite element model of the unnotched tensile test

7169 realizations were carried out by the forward stochastic analysis [75]. Table 20 and Figure 47 compare the simulation results with the experimental data [88]. Figure 48 depicts a typical displacement-force curve for the cases of minimal and maximal reaction force where the cross marks indicate the peak values (strength).

Table 20 UNT test results

	Simulation	Experiment
Mean (N)	127708.48	131867.6
CV (%)	5.16	7.40

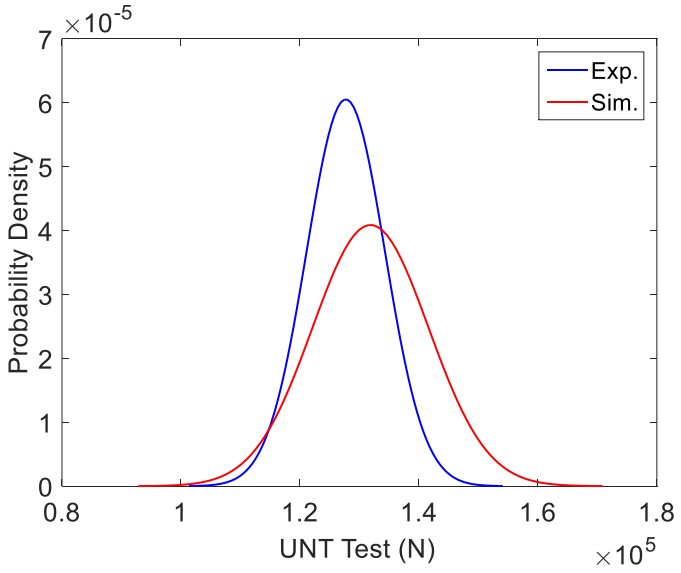

Figure 47 UNT - reaction force probability distribution: simulations versus experiment [88]

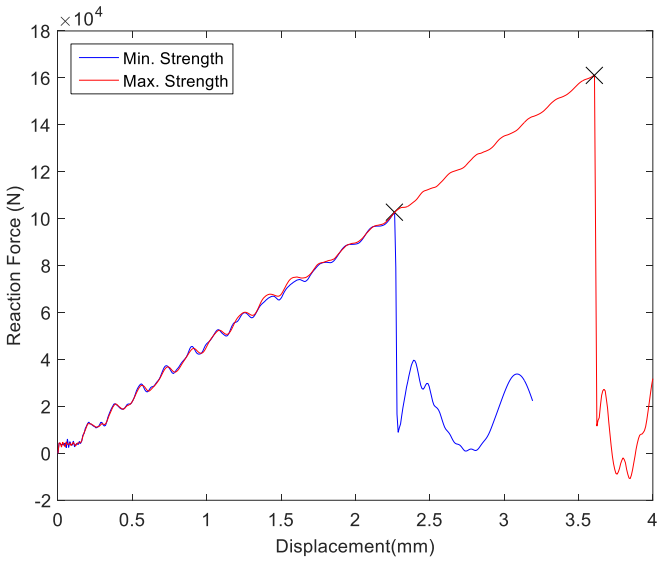

Figure 48 UNT - minimal and maximal reaction force: simulations versus experiment [88]

3.4.5.3 Open Hole Tensile (OHT) Test

Figure 49 depicts the open hole tensile test specimen considered in this study [88]. The plate consists of 24 plies with the following layup: $[(45/0/-45/90)_3]_s$. The specimen was clamped at one end and pulled at the other end in the longitudinal direction.

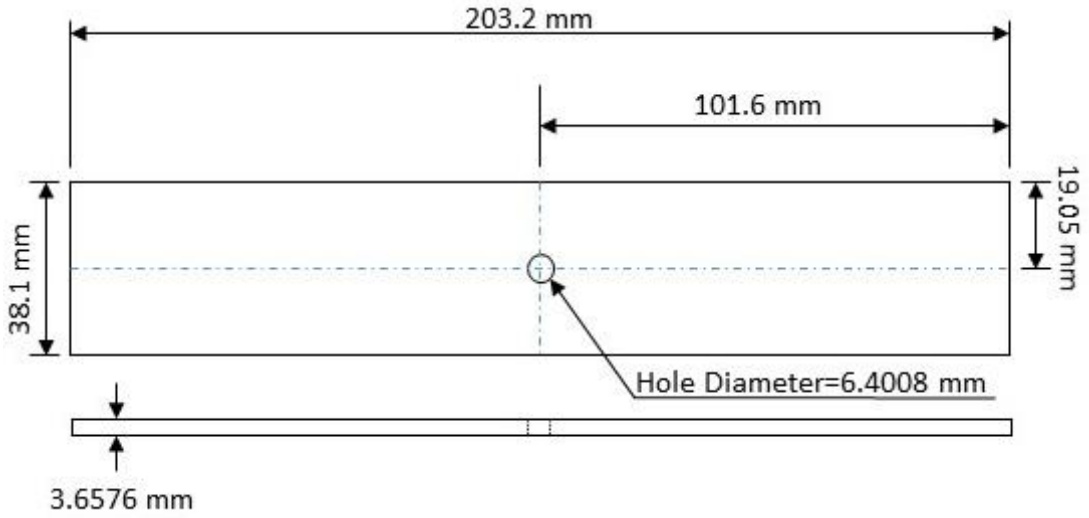

Figure 49 Notched tensile test dimensions

Figure 50 depicts the finite element mesh consisting of 212 twenty-node quadratic laminated elements in each of the 24 plies. The mesh was constructed in the way that the elements' characteristic length near the hole is about a quarter of the rest of the model. The macro finite element model was constructed in FOOF [155, 156] and the explicit algorithm was employed in the simulations.

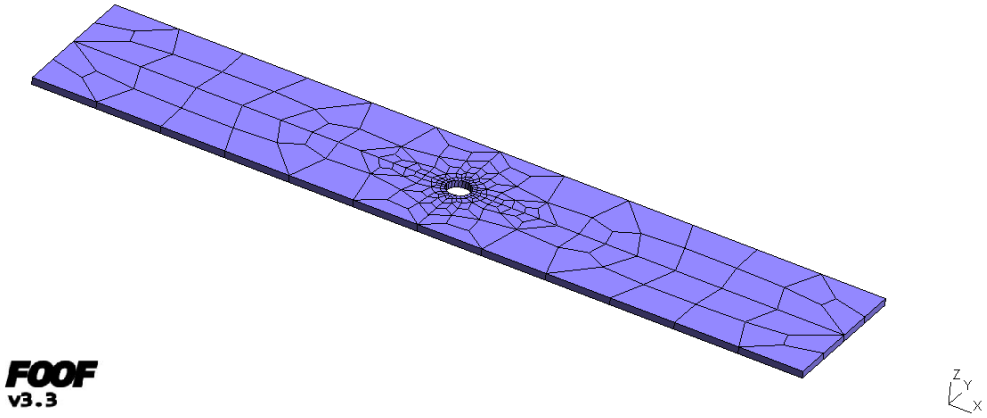

Figure 50 Open-hole tensile test finite element model

7169 realizations were performed by the forward stochastic analysis algorithm [75]. Results are summarized in Table 21 and Figure 51. The displacement-force curves corresponding to the minimal and maximal reaction forces are illustrated in Figure 52 with the cross marks indicating the peak values.

Table 21 OHT test results

	Simulation	Experiment
Mean (N)	46657.52	47560.4
CV (%)	3.72	4.23

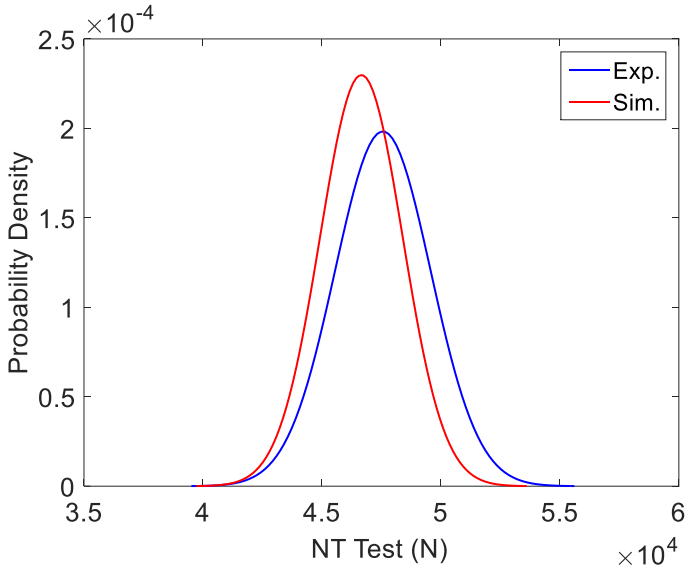

Figure 51 OHT- test reaction force probability distribution: simulations versus experiment [88]

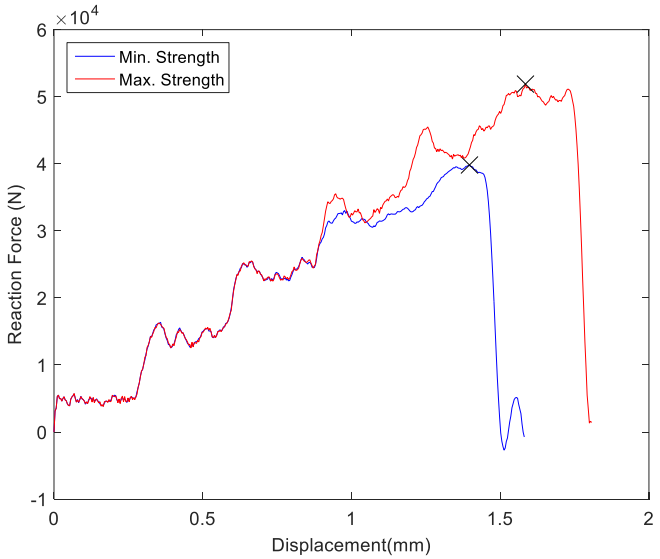

Figure 52 OHT - minimal and maximal strength: simulations versus experiment [88]

Chapter 4
Multiscale Modeling of Femur Fracture

In this chapter, an accelerated multiscale analysis of femur fracture was presented with the validation of reduced order homogenization (ROH). The method proposed takes advantages of the digital database created from ROH, which provides the single-scale model unknown material information, so that a more accurate and efficient simulation could be possible.

4.1 Multiscale Models of Femur

The two-scale finite element model of the proximal femur (macro level) [97] and cortical/trabecular structure (meso levels) is depicted in Figure 53. In the experimental setup, the distal end of the femur was embedded in a block of dental cement. Two nodes, in the center of dental cement fixture were attached with rigid beam elements to the distal end of the femur as shown in Figure 53. Displacements of trochanter surface were constrained in the vertical direction. A prescribed displacement was applied downwards in the femoral head surface. The above boundary conditions are consistent with a sideways fall on the hip.

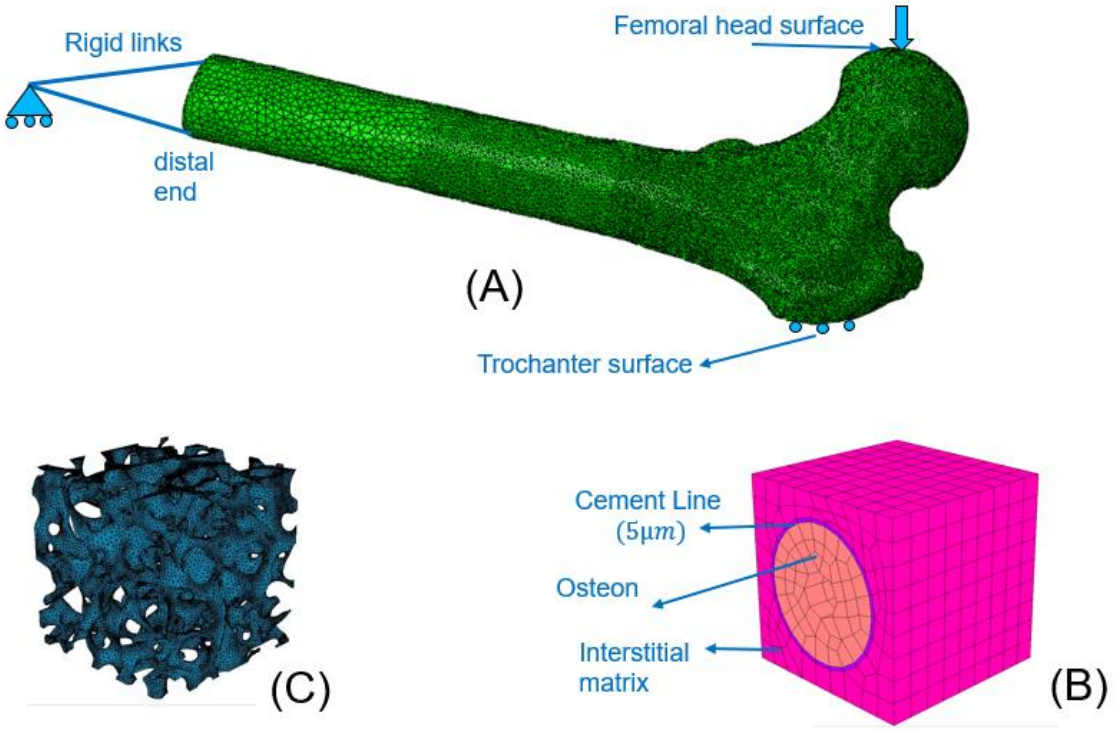

Figure 53 (A) Finite element model of proximal femur with schematics of load and boundary conditions; (B) Finite element model of periodic cortical bone mesostructure; (C) Finite element model of random trabecular bone mesostructure

We consider a strong form of the boundary value problem stated on the domain Ω^{ζ} comprising the bone structure

$$\sigma^{\zeta}_{ij,j}(\boldsymbol{x}) + b^{\zeta}_{i}(\boldsymbol{x}) = 0 \quad \boldsymbol{x} \in \Omega^{\zeta}, \tag{36}$$

$$\sigma^{\zeta}_{ij}(\boldsymbol{x}) = L^{\zeta}_{ijkl}(\boldsymbol{x})\left(\varepsilon^{\zeta}_{kl}(\boldsymbol{x}) - \mu^{\zeta}_{kl}(\boldsymbol{x})\right) \quad \boldsymbol{x} \in \Omega^{\zeta}, \tag{37}$$

$$\varepsilon^{\zeta}_{ij}(\boldsymbol{x}) = u^{\zeta}_{(i,j)}(\boldsymbol{x}) \equiv \frac{1}{2}\left(u^{\zeta}_{i,j} + u^{\zeta}_{j,i}\right) \quad \boldsymbol{x} \in \Omega^{\zeta}, \tag{38}$$

$$u^{\zeta}_{i}(\boldsymbol{x}) = \bar{u}^{\zeta}_{i}(\boldsymbol{x}) \quad \boldsymbol{x} \in \partial\Omega^{u\zeta}, \tag{39}$$

$$\sigma^{\zeta}_{ij}(\boldsymbol{x}) n^{\zeta}_{j}(\boldsymbol{x}) = \bar{t}^{\zeta}_{i}(\boldsymbol{x}) \quad \boldsymbol{x} \in \partial\Omega^{t\zeta}, \tag{40}$$

where the superscript ζ denotes meso-scale features; ε^{ζ}_{kl} and σ^{ζ}_{ij} the strain and stress components; L^{ζ}_{ijkl} the constitutive tensor; the total strain ε^{ζ}_{kl} is additively decomposed into

elastic strain and inelastic strain, more generally referred to as eigenstrains μ_{kl}^{ζ}. In the above, $\boldsymbol{n}^{\zeta}$ denotes the unit normal to the bone structure domain boundary $\partial\Omega^{\zeta}$ consisting of essential and natural boundaries denoted by $\partial\Omega^{u\zeta}$ and $\partial\Omega^{t\zeta}$. $\bar{u}_i^{\zeta}$ and $\bar{t}_i^{\zeta}$ are components of prescribed displacements and tractions, respectively, on corresponding boundaries; b_i^{ζ} is the body force.

Following two-scale asymptotic analysis where various fields are assumed to depend on the coarse-scale coordinate $\boldsymbol{x}$ and the unit cell coordinate $\boldsymbol{y} = \boldsymbol{x} / \zeta$, the strong form can be decomposed into the meso and macro problems. Following asymptotic analysis [10], the leading order equilibrium equations are:

Mesoscale problem

$$\begin{aligned}
&\sigma_{ij,y_j}^{f} = 0 \quad \boldsymbol{y} \in \Theta \\
&\sigma_{ij}^{f}(\boldsymbol{x},\boldsymbol{y}) = L_{ijkl}^{\zeta}(\boldsymbol{x},\boldsymbol{y})\left(\varepsilon_{kl}^{f}(\boldsymbol{x},\boldsymbol{y}) - \mu_{kl}^{f}(\boldsymbol{x},\boldsymbol{y})\right) \quad \boldsymbol{y} \in \Theta \\
&\varepsilon_{kl}^{f}(\boldsymbol{x},\boldsymbol{y}) = \varepsilon_{kl}^{c}(\boldsymbol{x}) + u_{(k,y_l)}^{(1)}(\boldsymbol{x},\boldsymbol{y}) \\
&u_i^{(1)}(\boldsymbol{x},\boldsymbol{y}) \text{ is periodic in } \partial\Theta
\end{aligned} \tag{41}$$

Macroscale problem

$$\begin{aligned}
&\sigma_{ij,x_j}^{c} + b_i^{c} = 0 \quad \boldsymbol{x} \in \Omega^{c} \\
&\varepsilon_{kl}^{c}(\boldsymbol{x}) = u_{(k,x_l)}^{c}(\boldsymbol{x}) \\
&\varepsilon_{ij}^{c} = \frac{1}{|\Theta|}\int_{\Theta} \varepsilon_{ij}^{f}\, d\Theta; \quad \sigma_{ij}^{c} = \frac{1}{|\Theta|}\int_{\Theta} \sigma_{ij}^{f}\, d\Theta; \quad b_i^{c} = \frac{1}{|\Theta|}\int_{\Theta} b_i^{\zeta}\, d\Theta \\
&BCs
\end{aligned} \tag{42}$$

where the superscript *c* and *f* denote the macro (proximal bone scale) and meso (trabecular and cortical bone structure) scale fields. Comma denotes spatial derivative at symmetric subscript brackets denote symmetric part. Θ is the unit cell domain (including the voids) and $|\Theta|$ its volume. The eigenstrain $\mu_{ij}^{f} \equiv \mu_{ij}^{\zeta}(\boldsymbol{\varepsilon}^{f}, \boldsymbol{\sigma}^{f}, \tilde{\boldsymbol{s}}^{f})$ depend on the constitutive

behavior of meso phases. In the present section they are assumed to follow continuum damage mechanics laws including regularization schemes in the form of staggered nonlocal formulation as described in [155, 158].

The primary objective of the two multiscale methods outlined below is on the effective solution of the mesoscale problem and the subsequent calculation of the coarse-scale stress required for full scale proximal bone analysis.

4.1.1 Reduced Order Homogenization (ROH) Model

In this section we briefly outline the formulation of the reduced order model [5, 10, 77, 78, 117-119] with focus on the specificities of the cortical and trabecular bone structure.

The salient feature of reduced order homogenization is that the mesoscale displacement field correction $u_i^{(1)}(\boldsymbol{x},\boldsymbol{y})$ to the smooth macroscale displacement $u_i^c(\boldsymbol{x})$ is constructed to satisfy the mesoscale equilibrium equation (42) a for arbitrary macroscale strain ε_{kl}^c, eigenstrains $\boldsymbol{\mu}_{ij}^f$, and eigenseparations $\delta_{\hat{n}}^f$, which describes the discontinuity at the interfaces of cement line, osteon and interstitial matrix in the cortical bone mesostructure (see Figure 53). $u_i^{(1)}(\boldsymbol{x},\boldsymbol{y})$ is constructed as follows

$$u_i^{(1)}(\boldsymbol{x},\boldsymbol{y}) = H_i^{kl}(\boldsymbol{y})\varepsilon_{kl}^c(\boldsymbol{x}) + \int_{\Theta} \tilde{h}_i^{kl}(\boldsymbol{y},\tilde{\boldsymbol{y}})\,\mu_{kl}^f(\boldsymbol{x},\tilde{\boldsymbol{y}})d\tilde{\Theta} + \int_S \breve{h}_i^{\breve{n}}(\boldsymbol{y},\breve{\boldsymbol{y}})\,\delta_{\breve{n}}^f(\boldsymbol{x},\breve{\boldsymbol{y}})d\breve{S} \qquad (43)$$

where H_i^{kl}, $\tilde{\boldsymbol{h}}_i^{kl}$, and $\breve{h}_i^{\breve{n}}$ are so-called transformation influence functions for the macrostrain, the eigenstrain, and the eigenseparation, respectively. The physical meaning of (43) is that the eigenstrain (or so-called transformation strain) $\mu_{kl}^f(\boldsymbol{x},\tilde{\boldsymbol{y}})$ introduces elastic deformation in the magnitude of $\tilde{h}_i^{kl}(\boldsymbol{y},\tilde{\boldsymbol{y}})$ due to volume and/or shape changes at an infinitesimal neighborhood of a point $\tilde{\boldsymbol{y}} \in \Theta$. The volume integral represents the

accumulative effect of all possible eigenstrains in the unit cell domain. Likewise, the eigenseparation $\delta_{\breve{n}}^{f}(\boldsymbol{x},\breve{\boldsymbol{y}})$ gives rise to elastic deformation equal to $\breve{h}_{i}^{\breve{n}}(\boldsymbol{y},\breve{\boldsymbol{y}})$ as a result of a debonding (or displacement jump) at an infinitesimal neighborhood of a point $\breve{\boldsymbol{y}} \in S$ at the mesoscale interface. Cohesive laws, such as those used in [159, 160], can be use to describe the traction-separation law in the cortical bone. The integral over all the interfaces in the unit cell represents an accumulative effect of all eigenseparations. In the present work we assume perfect interfaces, i.e. $\delta_{\breve{n}}^{f}(\boldsymbol{x},\breve{\boldsymbol{y}}) = 0$. Note that (43) holds for arbitrary eigenstrains as long as the strain follows the additive decomposition (37)c.

The salient feature of ROH is reduction of computational complexity of solving the mesoscale problem by discretizing eigenstrains μ_{ij}^{f} in (43) as

$$\mu_{ij}^{f}(\boldsymbol{x},\boldsymbol{y}) = \sum_{\alpha=1}^{M} N^{(\alpha)}(\boldsymbol{y})\mu_{ij}^{(\alpha)}(\boldsymbol{x}) \tag{44}$$

where $N^{(\alpha)}$ are eigenstrain shape functions are the number of phases in mesostructure. For trabecular bone mesostructure, *M = 1*. For cortical bone mesostructure, *M = 3*. The shape functions are selected as follows. Various eigenstrain modes are grouped into matrix (soft phase) or inclusion (stiff phase) dominated modes of deformation. The mode is considered to be matrix dominated if the overall property corresponding to that mode is of the same order of magnitude as that of the matrix; otherwise the mode is considered to be inclusion dominated.

For inclusion dominated mode the shape functions are assumed to be C^{-1} continuous with piecewise constant approximation

$$N^{(\alpha)}(\boldsymbol{y}) = \begin{cases} 1 & \boldsymbol{y} \in \Theta^{(\alpha)} \\ 0 & \boldsymbol{y} \in \Theta^{(\alpha)} \end{cases} \tag{45}$$

For the matrix dominated mode of deformation the shape functions are implicitly defined in such a way that when the unit cell is subjected to matrix dominated mode defamation, inclusion phases remain stress-free. For more details we refer to [10].

4.1.2 Accelerated Reduced Order Homogenization (AROH) Model

The primary goal of the accelerated reduced order homogenization (AROH) approach schematically depicted in Figure 3 is speed-up the multiscale simulations based on the ROH outlined in the previous section. AROH builds on the fact that ROH possesses considerably fewer material constants that need to be experimentally calibrated than a lower fidelity phenomenological anisotropic damage model. This is because each microphase in ROH is assumed to be isotropic with just two parameters describing inelastic behavior of a single phase. On the other hand, an anisotropic single-scale damage model [155, 158], which serves the basis for AROH, which has considerably more material constants that have to be calibrated against experimental data. Unfortunately, only limited patient-specific bone fracture data is available. Therefore, it is much easier to calibrate ROH to limited experimental data than a single-scale anisotropic damage model. Furthermore, the computational cost of ROH is significantly higher than of AROH since ROH requires solution of 18 equations with 18 unknowns (6 unknown eigenstrains components for each of the meso-phases in the cortical bone) at each quadrature point and at very increment. Once material constants have been identified, AROH is computationally superior to ROH and thus can be deployed for analysis of full-scale proximal femur model. It is this interplay between ROH and single-scale anisotropic damage model that is at the heart of the AROH. First, ROH is calibrated against limited test data. Consequently, the calibrated ROH model is subjected to triaxial loading conditions and a comprehensive

digital database is created to complement the limited test data (Figure 54), which is the used to identify model parameters of the single-scale anisotropic damage model.

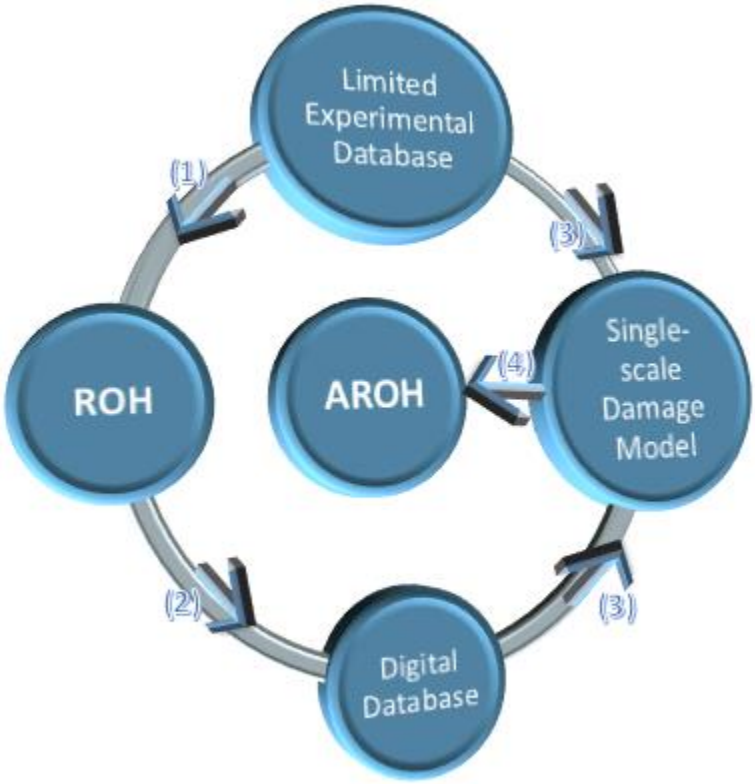

Figure 54 Accelerated Reduced Order Homogenization: (1) Limited experimental database is employed to calibrate the ROH; (2) The calibrated ROH is utilized to generate extensive digital database to compliment limited experimental database; (3) A single-scale damge model is calibrated against the integrated digital/experimental database; (4) The calibrated single-scale phenomenological damage model is used for bone analysis

4.2 Multiscale model construction

Let us first review the information we have and additional assumptions we need to make in order to fully characterize the multiscale model. The geometry of the bone is given from the quantitative computer tomography (QCT). The generation of the bone's geometry (and thereafter the FE mesh) is considered, to a large extent, as a solved problem [161].

While there is a certain amount of uncertainty regarding the precise modeling, load and boundary conditions, which have been discussed in [97], we consider hereafter it to be well defined and adopt the guidelines proposed in [97]. An adequate characterization of material properties, on the other hand, remains challenging due to inherent *heterogeneous*, *anisotropic*, and *inelastic* nature of the bone's tissue.

In order to characterize the heterogeneous, anisotropic and inelastic bone properties our goals are two-fold: (i) identify the elastic and inelastic properties of the cortical and trabecular mesostructure and (ii) determine the orientation of the mesostructure in various point (Gauss quadrature points) of the macro (proximal bone) finite element model (Figure 53A).

4.2.1 Identification of Mesostructural Orientation

For bone tissue orientation we employ an approach motivated by so called Wolff's law [162], which states that bone tissue orientation correlates well with principal strain direction [163] in the stance position. To determine the orientation of the mesoscale unit cells at various quadrature point in the macro-mesh, we employ the following three step approach. In Step 1, we assume that the bone material is isotropic and single-scale, with values of isotropic elastic properties and yield strains assigned to each finite element in the femur model based on estimated Hounsfield units (HU), which represent the measured grey levels in the QCT scans, and the power law (1) with the following values of parameters in Table 22 [164].

Table 22 Relation between density and mechanical properties

	a_E	b_E	a_σ	b_σ
Cortical bone - axial	2065	3.09	72.4	1.88
Cortical bone - transverse	2314	1.57	37	1.51
Trabecular bone[2]	1904	1.64	40.8	1.89

Other empirical relations between Young's modulus and bone density for cortical and trabecular bone have been proposed in [165, 166].

In Step 2, we conduct a linear single-scale finite element analysis of the femur bone model to determine the maximum principal strain directions at various Gauss points in the macro-mesh.

In Step 3, we determine the direction of the maximum overall stiffness at the mesoscale and align it with maximum principal direction of strain in the stance position. For the cortical bone, the maximum stiffness coincides with the direction of the osteon. An alternative approach by cortical bone mesostructure was positioned to follow the outer surface was discussed in [167].

Individual trabeculae segmentation (ITS)-based morphological analysis has been conducted for trabecular bone [168], which revealed its anisotropic elastic response. To find the maximum overall Young's modulus $E^{eff}_{\max}$ of the trabecular bone, we first compute the overall properties using linear homogenization L^{eff}_{ijkl}. We then seek for the rotation $\boldsymbol{\theta} = [\theta_1 \quad \theta_2 \quad \theta_3]$ that rotates L^{eff}_{ijkl} into

[2] The largest value reported in [111]

$$L^{eff}_{IJKL} = R_{Ii}(\theta)R_{Jj}(\theta)R_{Kk}(\theta)R_{Ll}(\theta)L^{eff}_{ijkl} \tag{46}$$

such that the effective Young's modulus is maximized. In Eq. (46), $R_{Ii}(\theta)$ is the rotation matrix.

4.2.2 Identification of Mesostructural Properties

To identify elastic and inelastic phase properties at the mesoscale we make the following assumption: the Young's modulus and compressive strength defined in Eq. (1) with parameter values given in Table 22 correspond to the *average effective* Young's modulus and compressive strength. Each meso-phase will be assumed as either isotropic or transverse isotropic with subscripts *a* and *t* denoting axial and transverse isotropic properties. For instance, $E_a^{(\alpha)}$ and $E_t^{(\alpha)}$, denote the compressive Young's modulus of meso-phase α in the axial and transverse directions, respectively. The inelastic behavior of each phase is based on continuum damage mechanics [155, 158] assuming either bilinear or trilinear damage evolution law depicted in Figure 55.

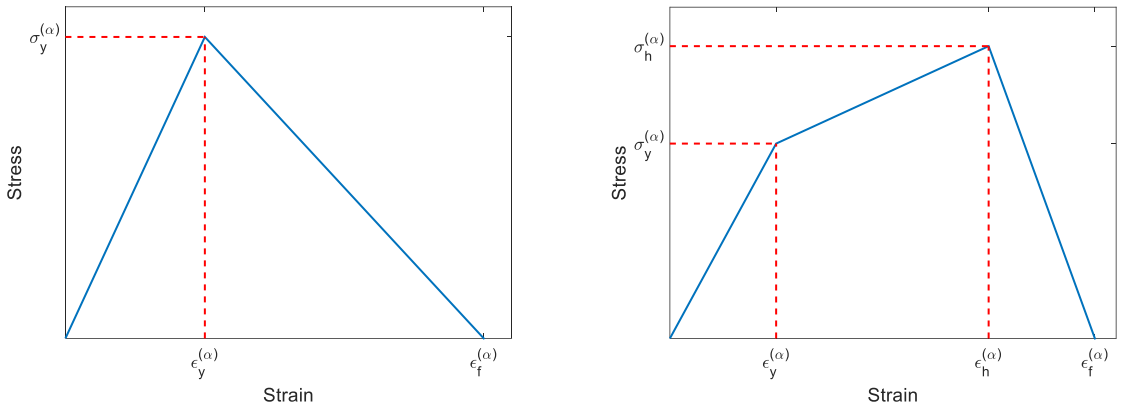

(a) (b)

Figure 55 (a) Bilinear damage law; (b) Trilinear damage law

For trabecular bone, we lump trabecular plates (p) and rods (r) into a single meso-phase. We assume that the trabecular bone meso-phase is isotropic and its inelastic behavior follows the trilinear damage law. Assuming Poisson ratio $\nu^{(pr)} = 0.3$, its remaining model parameters $\left(E^{(\mathrm{pr})}, \sigma_y^{(\mathrm{pr})}, \sigma_h^{(\mathrm{pr})}, \varepsilon_h^{(\mathrm{pr})}, \varepsilon_f^{(\mathrm{pr})}\right)$ are identified as follows. First, elastic modulus $E^{(\mathrm{pr})}$ is calibrated to match the largest homogenized modulus of the trabecular bone unit cell defined by equation (1) with parameter values summarized in

Table 23. Given the calibrated elastic modulus $E^{(\mathrm{pr})}$, model reductions is performed to reduce the computational complexity of the mesoscale unit cell. Finally, the values of $\left(\sigma_y^{(\mathrm{pr})}, \sigma_h^{(\mathrm{pr})}, \varepsilon_h^{(\mathrm{pr})}, \varepsilon_f^{(\mathrm{pr})}\right)$ are identified to match the maximum overall stress-strain behavior of the trabecular bone unit cell as described in Section 4.2.

For the calibration of cortical bone three meso-phases, cement line (c), osteon (o) and interstitial matrix (i), we have to our disposal two experiments, one in the axial direction and one in the transverse direction based on Eq. (1) and parameter values given in Table 22. In solving the identification problem, which is a constrained optimization

problem, we will assume initial properties of meso-phases based on the nanoindentation tests conducted in [169] where the average Young's modulus for the osteon was E = 22.4 GPa and E = 25.8 GPa for interstitial lamellae with corresponding standard deviations of 1.3 GPa and 0.7 GPa. We assume meso-phases (osteon and matrix) to be transverse isotropic [170]. The exact nature and composition of the cement line remains a subject of current research, it is usually considered to be much more compliant than that of osteon [171]. The Poisson's ratio of the cement line has been reported to be 25% higher than that of the osteon [172]. In the present study we will assume the value of the Young's modulus equal to half of the axial modulus of the osteon.

4.3 Bone Fracture Simulations

4.3.1 Finite Element Model

The finite element mesh of the femur depicted in Figure 56 consists of 650,000 tetrahedral elements. The reaction force was computed from the set of nodes on the femoral head surface defined in Figure 53 where prescribed displacement equal to 5mm was applied downward. Based on the density measurements by the quantitative computer tomography, material properties have been discretized into 42 piecewise constant values. To further reduce computational complexity, nonlinear properties were only considered in the neck region (shown in red in Figure 56), which is where fractures are most often expected, whereas the remaining femur domain is assumed to be elastic.

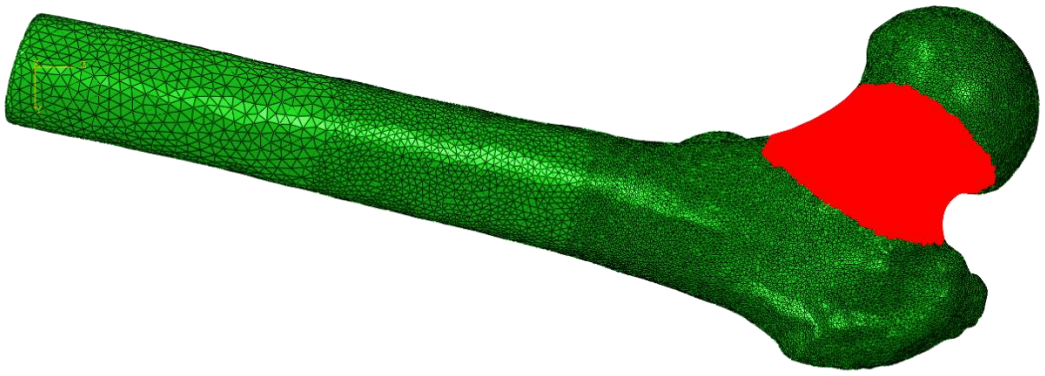

Figure 56 Finite element model of femur. Material properties in the region shown in red are assumed to be nonlinear

Using a single-scale linear analysis of the femur in stance position (Figure 57), local orientations of each Gauss point were identified. Figure 58 illustrates the orientations assigned to select quadrature points in the neck region. The red arrow points in the direction of the maximum principal direction in the trabecular and cortical bone. It can be seen that in the cortical bone, the maximum principal direction is tangential to the femur surface.

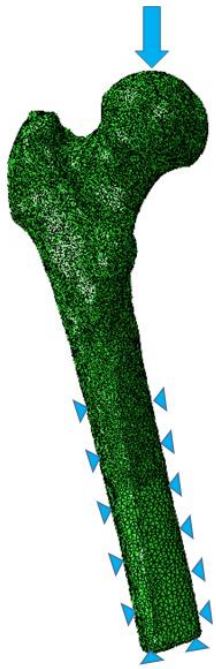

Figure 57 Stance position used to determine local material orientations

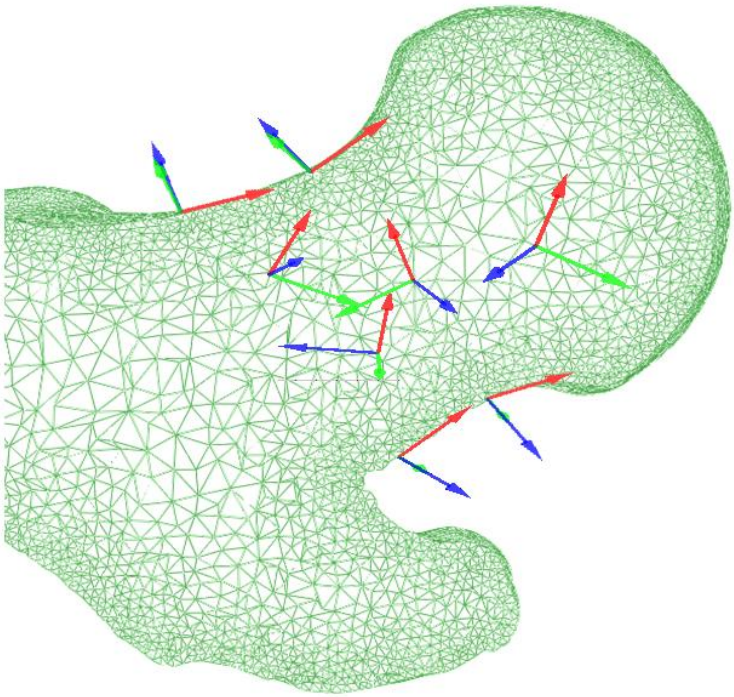

Figure 58 Local orientations shown in selected points

4.3.2 Calibration of the Reduced Order Model and Generation of Digital Database

Each meso-phase in the cortical and trabecular bone is modeled by bilinear damage and trilinear damage law, respectively. Meso-phase properties have identified for 42 different unit cells. The identified meso-phase properties of the trabecular bone mesostructure corresponding to ρ_{app} = 0.41 g/cm^3 are summarized in

Table 23. The identified meso-phase properties of the cortical bone mesostructure corresponding to ρ_{app} = 2.09 g/cm^3 are summarized in

Table 24 with the subscription *a* and *t* denoting the axial and transverse directions, respectively. Figure 59 and Figure 60 depict a typical calibration of the ROH model for the cortical bone mesostructure in the axial (osteon) and transverse compression. Once the ROH model has been calibrated, a digital database is generated for calibration of AROH. Figure 61 and Figure 62 depict the digital database for the cortical bone in two shear directions.

Table 23 Calibrated elastic material properties of the trabecular bone (ρ_{app} = 0.41 g/cm^3)

Bone Type	Parameter	Calibrated Value
Trabecular	$E^{(pr)}$	2155.9 MPa
	$n^{(pr)}$	0.3
	$s_y^{(pr)}$	37.1 MPa
	$s_h^{(pr)}$	37.1 MPa
	$e_h^{(pr)}$	0.034
	$e_f^{(pr)}$	0.052

Table 24 Calibrated elastic material properties of the cortical bone (ρ_{app} = 2.09 g/cm^3)

Bone Type	Parameter	Calibrated Value
Osteon	$E_t^{(o)}$	8500.0 MPa
	$E_a^{(o)}$	17000.0 MPa
	$n_t^{(o)}$	0.3
	$n_a^{(o)}$	0.3
	$G_a^{(o)}$	9000.0 MPa
	$s_{yt}^{(o)}$	100.45 MPa
	$e_{ft}^{(o)}$	0.013
	$s_{ya}^{(o)}$	244.8 MPa
	$e_{fa}^{(o)}$	0.0158
Cement	$E^{(c)}$	8500.0 MPa
	$n^{(c)}$	0.3
	$s_y^{(c)}$	122.40 MPa
	$e_f^{(c)}$	0.0158
Matrix	$E_t^{(m)}$	12269.7 MPa
	$E_a^{(m)}$	24539.3 MPa

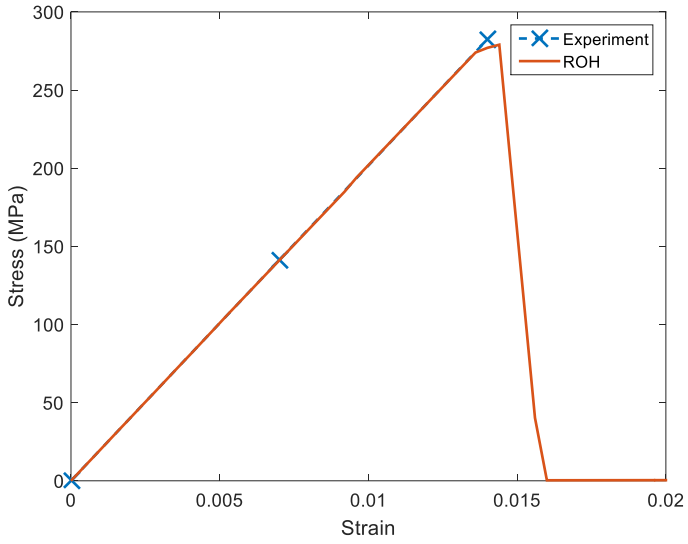

Figure 59 ROH calibration in axial compression for the cortical bone (ρ_{app} = 2.09 g/cm^3)

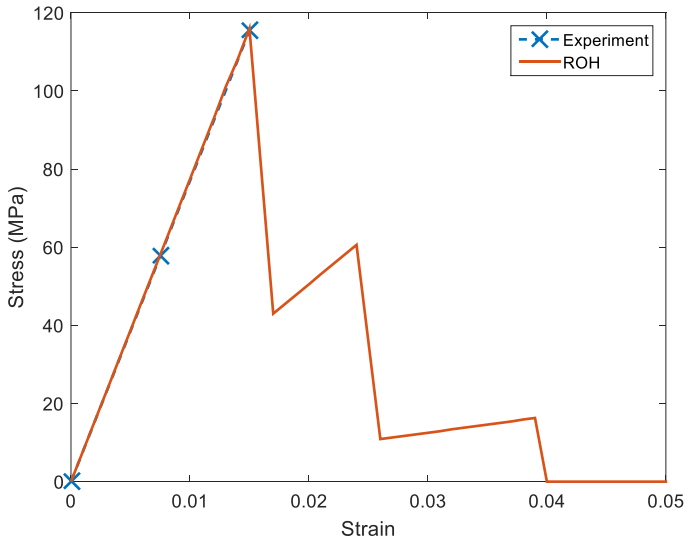

Figure 60 ROH calibration in transverse compression for the cortical bone (ρ_{app} = 2.09 g/cm^3)

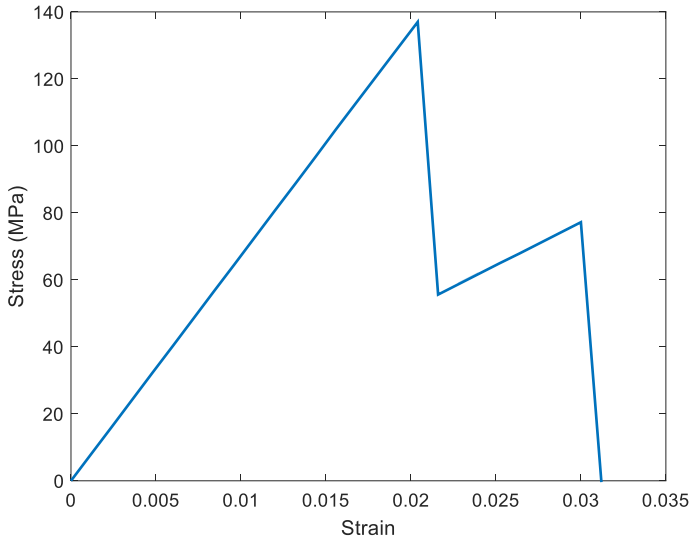

Figure 61 Digital database in axial shear for the cortical bone (ρ_{app} = 2.09 g/cm^3)

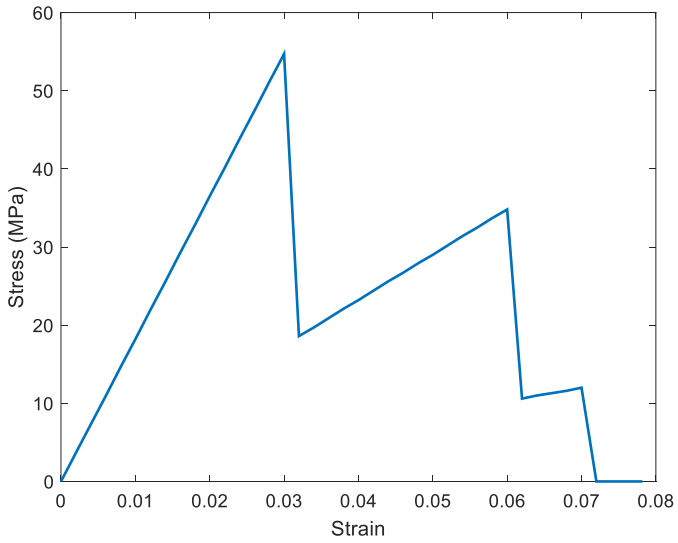

Figure 62 Digital database in transverse shear for the cortical bone (ρ_{app} = 2.09 g/cm^3)

Figure 63 depicts calibration of the ROH model for the trabecular bone mesostructure corresponding to ρ_{app} = 0.41 g/cm^3 to the overall compression defined by equation (1). Since only a single unit cell of the trabecular bone was available in this study,

phase properties of trabecular plates and rods were calibrated to be consistent with the prescribed porosity. Following the inelastic response of trabecular bone reported in [173], we set $\varepsilon_h = 2\varepsilon_y$ and $\varepsilon_f = 3\varepsilon_y$. Figure 65 plots the database created in four directions for trabecular bone.

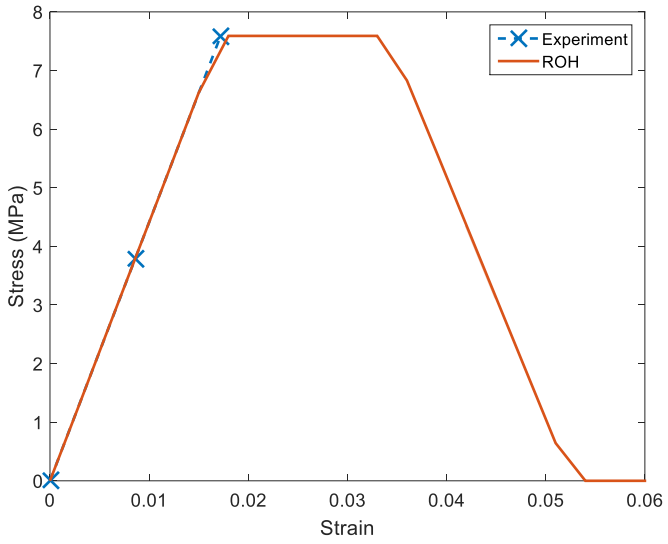

Figure 63 ROH calibration for the trabecular bone in 11 mode (ρ_{app} = 0.41 g/cm^3)

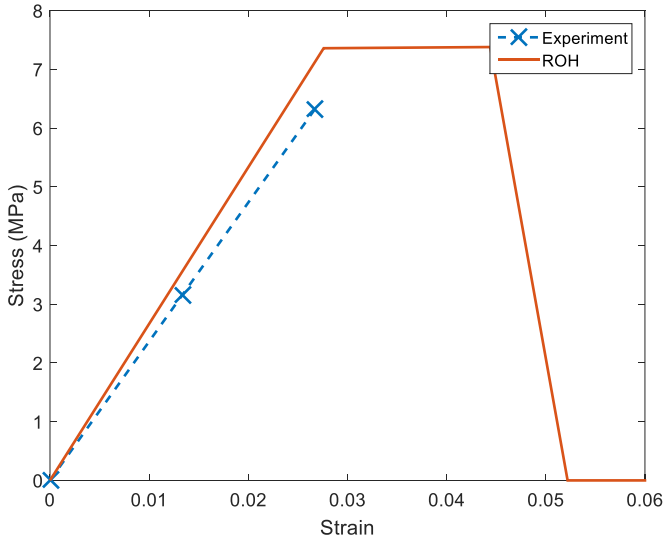

Figure 64 ROH calibration for the trabecular bone in 33 mode (ρ_{app} = 0.41 g/cm^3)

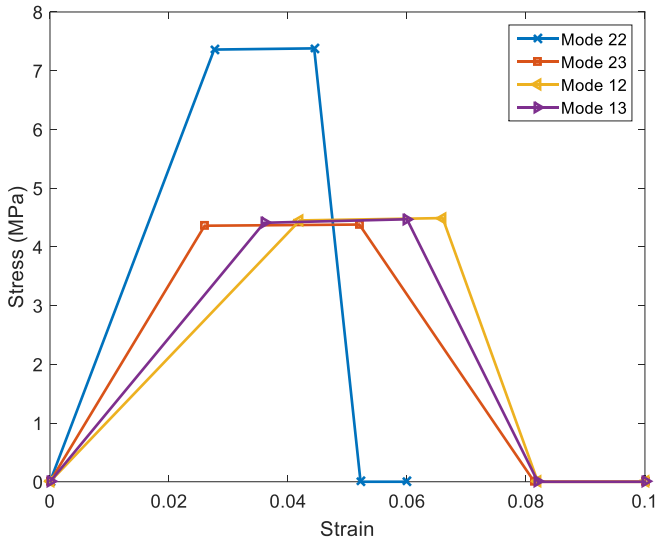

Figure 65 Digital database in four deformation modes for the trabecular bone (ρ_{app} = 0.41 g/cm^3)

4.3.3 Calibration of AROH to hybrid experimental-digital database

The trilinear orthotropic damage law were employed to calibrate the simulation results in Section 4.3.2. Table 25 and

Table 26 list the typical calibrated AROH material parameters for cortical and trabecular bone. Figure 66 - Figure 75 depict the typical calibration results for different loading conditions for both bone types.

Table 25 Cortical bone AROH material parameters (ρ_{app} = 2.09 g/cm^3)

Parameter	Value
E_t, E_a	7743.3, 20158.2 MPa
n_t, n_a	0.3
G_a	1823.2 MPa
s_{yt}, s_{ya}	116.3, 279.7 MPa
s_{ht}, s_{ha}	25.0, 285.0 MPa
e_{ht}, e_{ha}	0.032, 0.0144
e_{ft}, e_{fa}	0.04, 0.016

Table 26 Trabecular bone AROH material parameters (ρ_{app} = 0.41 g/cm^3)

Parameter	Value
E_1, E_2, E_3	266.5, 395.8, 441.1 MPa
n_1, n_2, n_3	0.3
G_{23}, G_{13}, G_{12}	167.4, 122.5, 112.7 MPa
s_{y1}, s_{y2}, s_{y3}	7.4 MPa
s_{h1}, s_{h2}, s_{h3}	7.4 MPa
e_{h1}, e_{h2}, e_{h3}	0.0444, 0.034, 0.051
e_{f1}, e_{f2}, e_{f3}	0.051

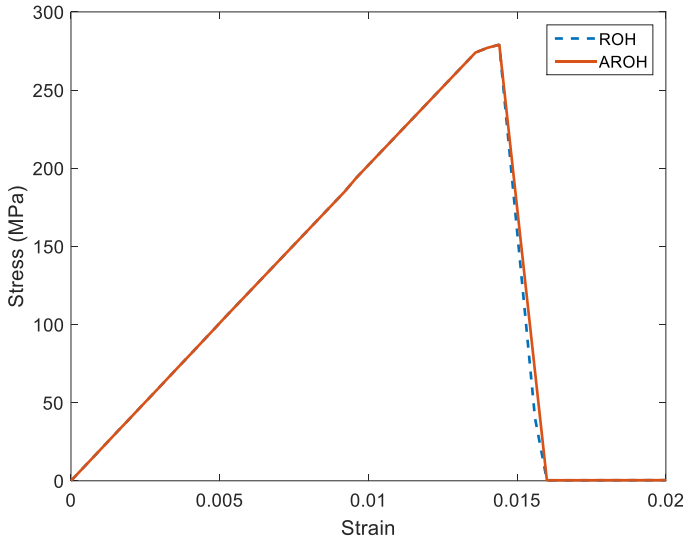

Figure 66 AROH calibration in axial compression for the cortical bone (ρ_{app} = 2.09 g/cm^3)

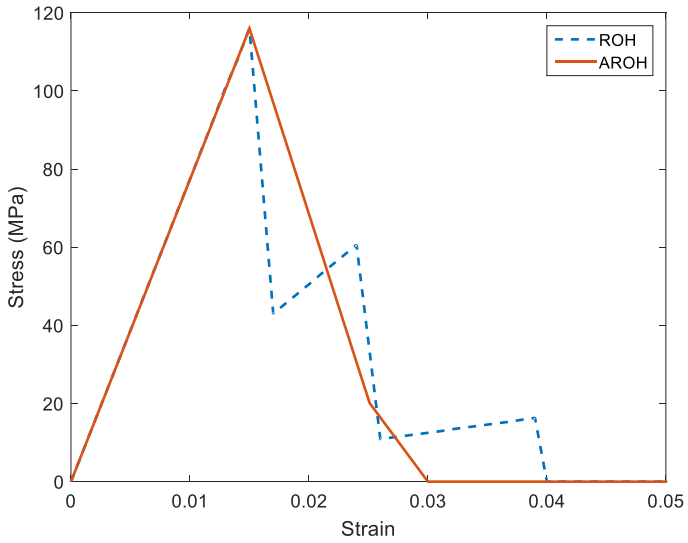

Figure 67 AROH calibration in transverse compression for the cortical bone (ρ_{app} = 2.09 g/cm^3)

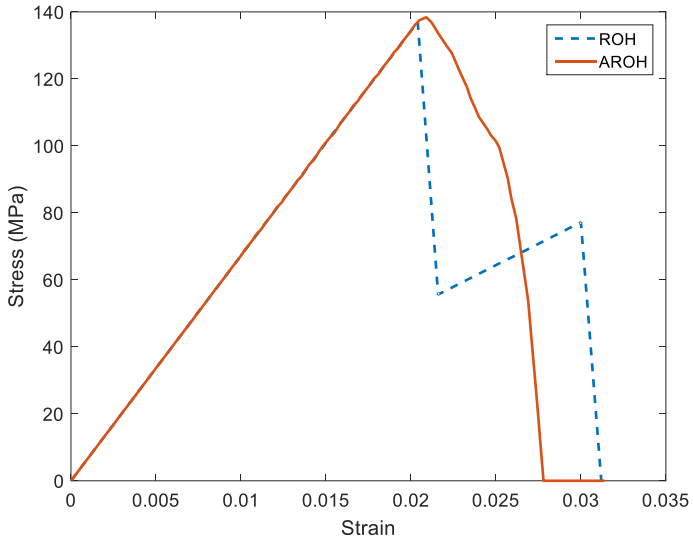

Figure 68 AROH calibration in axial shear for the cortical bone (ρ_{app} = 2.09 g/cm^3)

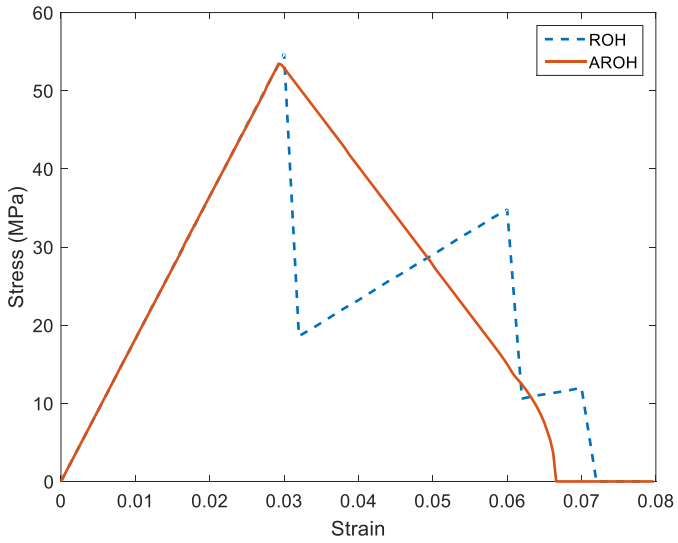

Figure 69 AROH calibration in transverse shear for the cortical bone (ρ_{app} = 2.09 g/cm^3)

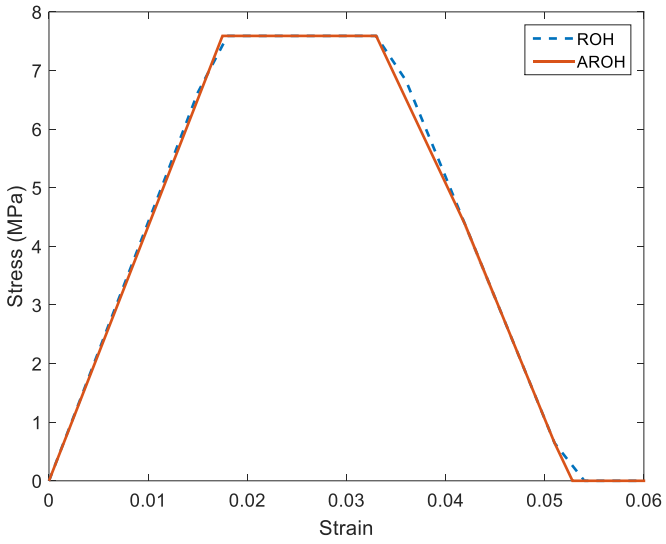

Figure 70 AROH calibration for the trabecular bone in 11 mode (ρ_{app} = 0.41 g/cm^3)

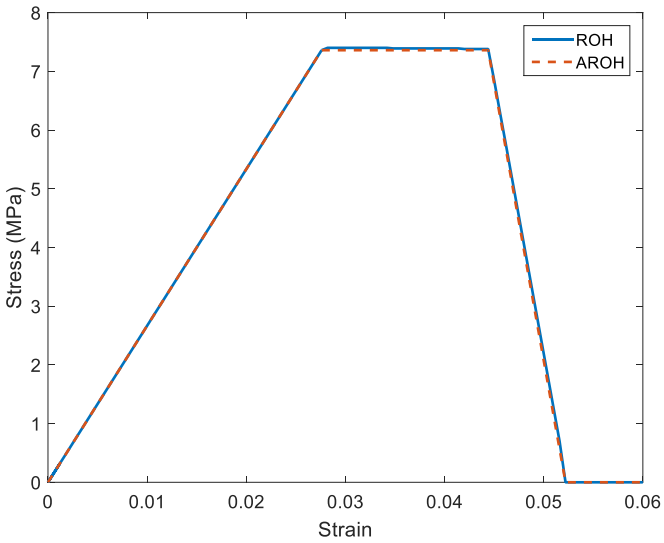

Figure 71 AROH calibration for the trabecular bone in 22 mode (ρ_{app} = 0.41 g/cm^3)

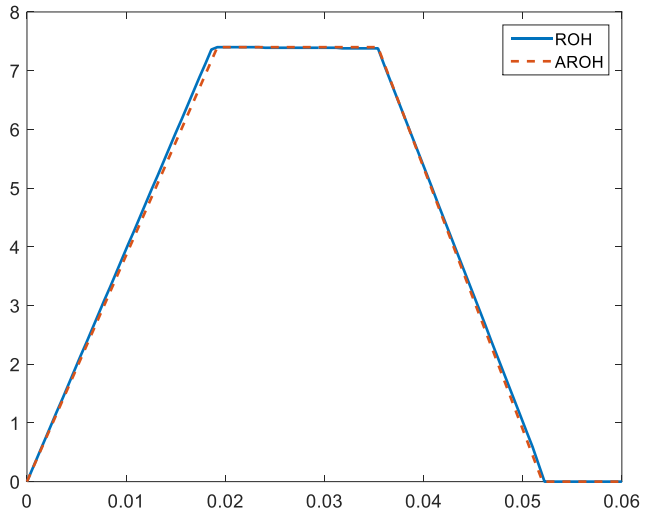

Figure 72 AROH calibration for the trabecular bone in 33 mode (ρ_{app} = 0.41 g/cm^3)

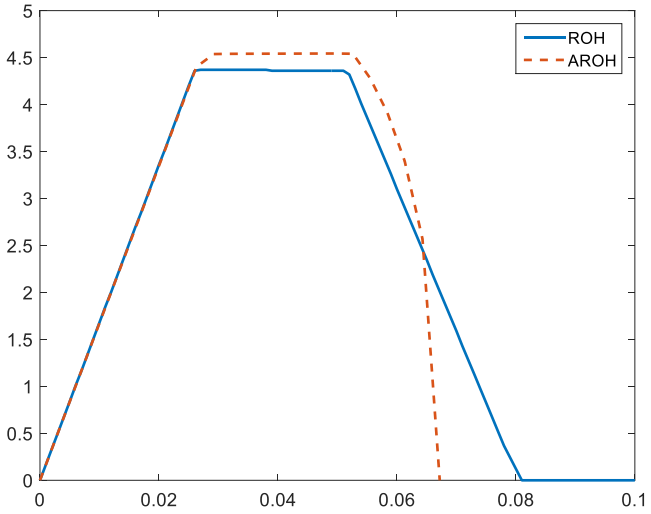

Figure 73 AROH calibration for the trabecular bone in 23 mode (ρ_{app} = 0.41 g/cm^3)

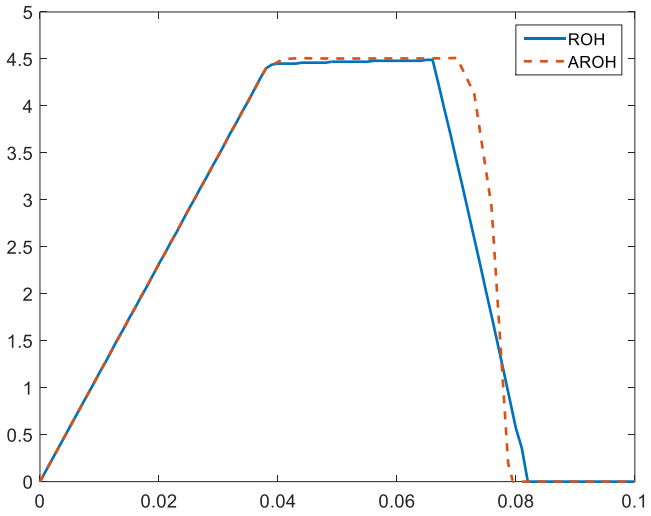

Figure 74 AROH calibration for the trabecular bone in 12 mode (ρ_{app} = 0.41 g/cm^3)

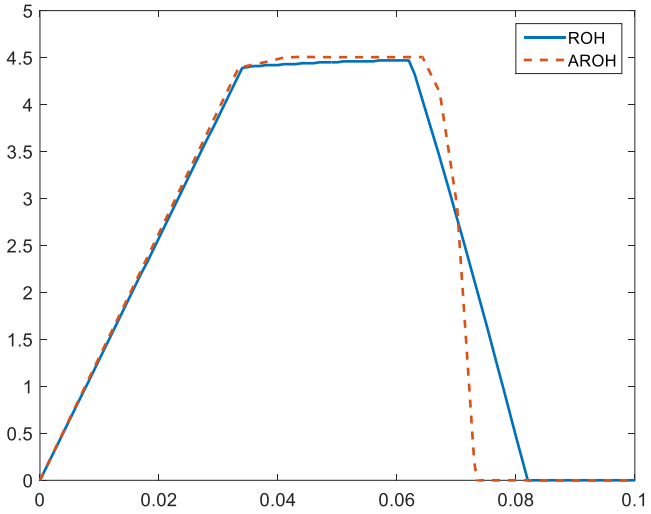

Figure 75 AROH calibration for the trabecular bone in 13 mode (ρ_{app} = 0.41 g/cm^3)

4.3.4 Bone Fracture Simulations and Validation

AROH simulations were performed with Abaqus on a 48-core 2.3 GHz Dell server with 128 GB RAM memory. The simulations had a computing time of 6 hours. To verify the accuracy of AROH simulation, we also performed ROH simulation on the same

machine. The ROH simulation had a computing time of 29 hours. Figure 76 compares the ROH macroscale simulation and the corresponding AROH simulation with the calibrated material parameters. It can be seen that AROH simulation results are in good agreement with the ROH simulations.

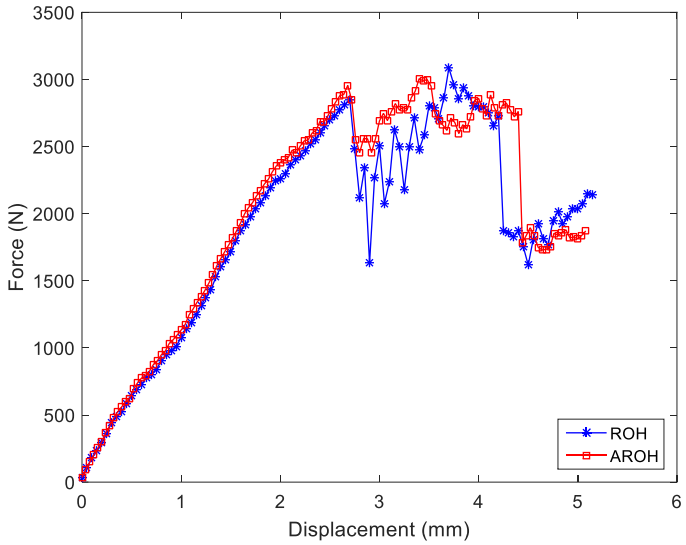

Figure 76 Comparison of AROH and ROH simulations of femur sideways fall

In [174], it has been observed that once peak bone mass is reached, the loss of bone mass follows slow first-order degradation rate, such the loss of bone density is 11% per decade for the trabecular bone and 3% for the cortical bone. We next study the influence of loss of bone density on the stiffness and the peak load of a human femur in a sideways fall situation. For each femur sideways fall simulation, the 42 ROH models and 42 AROH models were calibrated following the procedures outlined in Section 4.2 and Section 4.3. The simulation results are presented in Figure 77 together with a typical displacement-reaction force curve reported in [175, 176]. It can be seen, that the simulations provide reasonable stiffness and peak load of an osteoporosis femur.

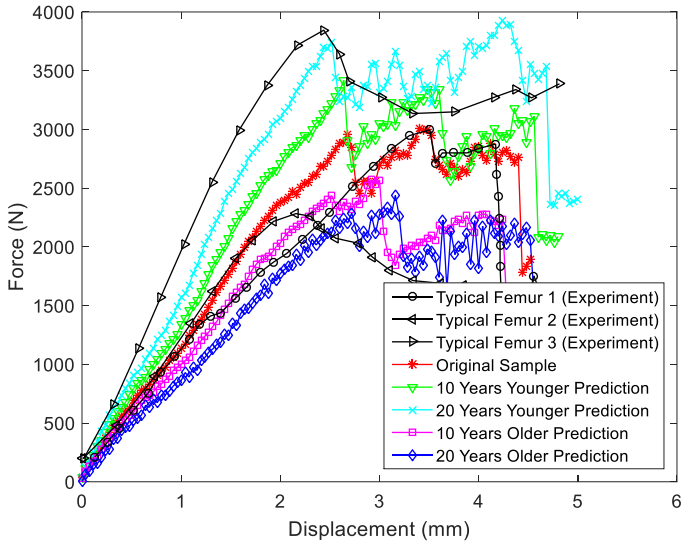

Figure 77 Femur sideways fall on the hip AROH simulation with prediction and experiment results

Figure 78 and Figure 79 depict the intertrochanteric fracture and subcapital neck damage with both ROH and AROH simulation. We compare the fracture pattern with what was reported in the open literature in Figure 80.

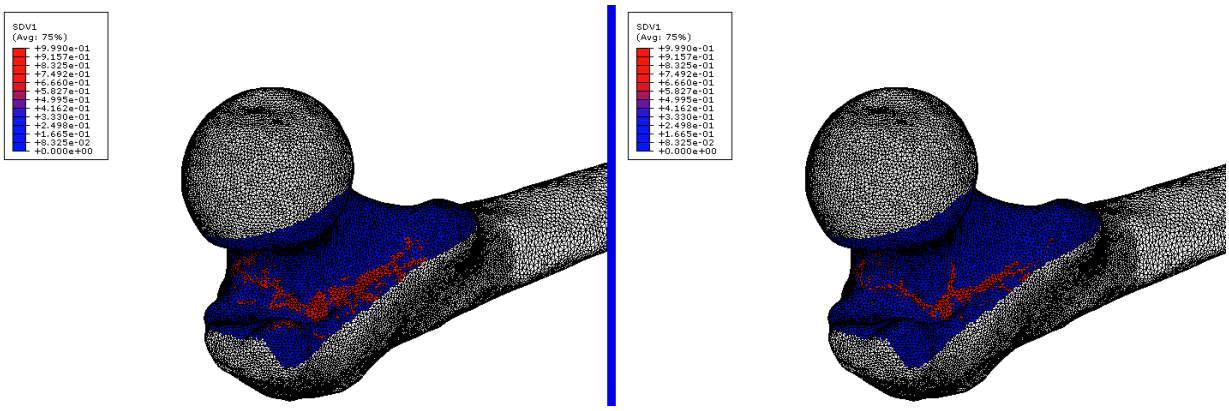

Figure 78 Fracture pattern view 1 (left: ROH, right: AROH)

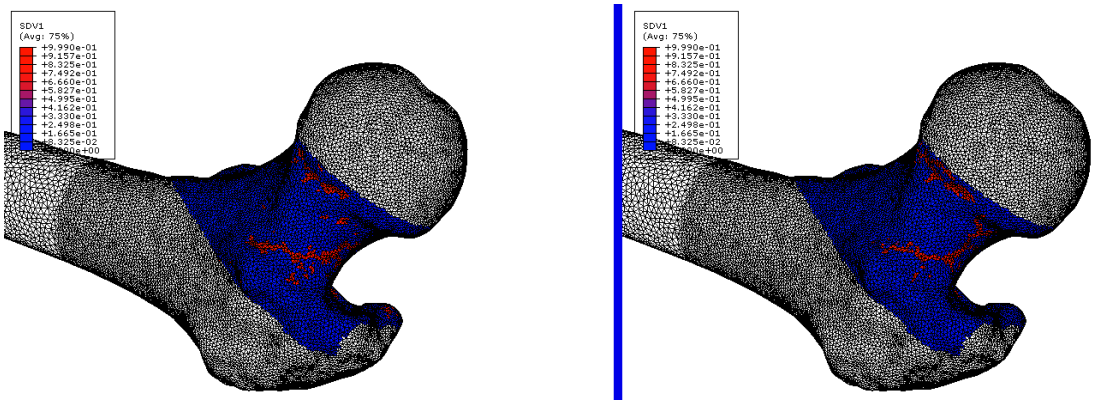

Figure 79 Fracture pattern view 2 (left: ROH, right: AROH)

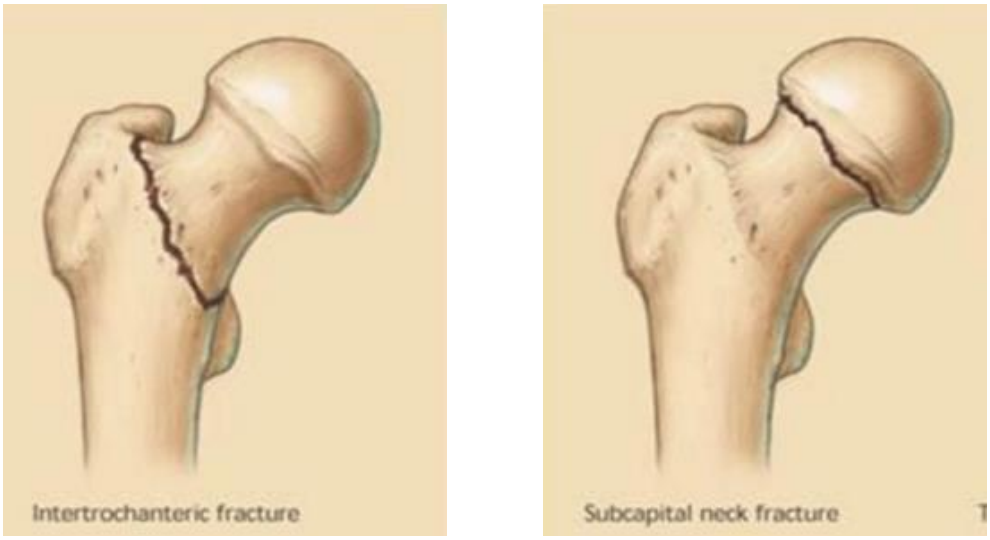

Figure 80 Typical Proximal Femur Fractures [177]

Chapter 5
Conclusions

Multiscale analysis of composite materials and structures well into their nonlinear regime is a challenging problem on its own due to considerable computational complexity involved. Adding an optimization layer on top of inelastic multiscale analysis with design variables at three scales magnifies the computational complexity by several orders of magnitude. We show that despite the seemingly intractable problem, it can be indeed simulated in one to two days on a 20-core machine. In addition to utilizing reduced order homogenization technology developed elsewhere, several new elements have contributed to this feat. First, we perfected the ant colony optimization (ACO) algorithm, by developing a methodology that gives rise to uniform sampling of the design space at multiple scales resulting in superior performance of the ACO. Secondly, we replaced unstructured meshing of RVE geometry that does not permit sensitivity analysis especially for coarse meshes by mapping of so-called base RVE mesh. Finally, we employed a multilevel optimization procedure that takes advantage of possible weak coupling of scales.

To study the stochasticity of the micro properties of composite material. A complete test data of the TORAY T700GC-12K-31E and Epoxy #2510 material system from the NIAR report has been employed to validate the proposed adaptive nonintrusive stochastic inverse algorithm. Given the micro-geometry definition, mechanical test data in the axial tension, transverse tension and shearing, microscale mechanical properties have been identified using the proposed adaptive nonintrusive stochastic inverse algorithm. Once the stochastic properties of model parameters have been identified, the adaptive nonintrusive

stochastic inverse algorithm has been validated by considering various unnotched and open-hole laminates tests. In all validation tests, the error in the mean was less than 5%. In the UNT lamina test, the error in the standard deviation was less than 10%. In the UNT laminate test and in the open-hole test, the error in the standard deviation was as high as 20% in some cases.

And while 10% error in the mean and 20% in the standard deviation are acceptable from the practical point of view, it is instructive to point out to the possible causes of error that can be attributed to one or more approximations made:

i) neglecting the variation in the fiber-volume fraction, lamina thickness, and elastic constants;

ii) neglecting the cross-correlation, which may exist between the random parameters considered;

iii) assuming that model parameters are random variables as opposed to random fields; and

iv) neglecting free edge effects in the deterministic multiscale solver that may lead to delamination.

The above approximations (ii) and (iii) were primarily made due to lack of experimental data. The second assumption is supported by the work of Graham and Deodatis [178] who demonstrated that the cross-correlation effects do not affect significantly the response variability when static problems are considered.

In our future studies, the effect of random fields given limited experimental data should be investigated. Karhunen-Loeve (KL) expansion to discretize the random fields in terms of a small set of denumerable random variables [60] is a viable option. Finally, the

issue of accuracy and computational efficiency of the deterministic nonlinear multiscale solvers, which has not been addressed in the previous chapter, remains an important research area on its own.

Chapter 4 presents an attempt to devise a generic (non-patient-specific) framework for inelastic multiscale analysis of femur fracture. The generic multiscale framework utilizes limited experimental data such as: (i) a single QCT scan of full scale femur and (ii) a single QCT scan of the mesostructure. The proposed multiscale framework takes advantage of existing models that relate the overall elastic and inelastic properties of the cortical and trabecular bone microstructure to bone density estimated from the Hounsfield units that represent the measured grey levels in the quantitative computer tomography (QCT) scans. Mesostructural properties are reverse engineered (identified) from these overall properties and Wolff's law is employed to orient the cortical and trabecular bone unit cells. Various perturbations from a single sample of the osteoporosis patient QCT scan are obtained by perturbing bone densities assuming that cortical and trabecular bone densities reduce by 3% and 11% over a single decade, respectively.

The simulation results suggest that the proposed multiscale framework is both efficient and predictive. The model efficiency has been demonstrated by analyzing full scale femur in less than 6 hours. The model is predictive in the sense that the observed femur fracture in sideways fall is within the range simulations that employ bone densities perturbed by one decade from a single QCT scan used in the simulations.

Nevertheless, confidence or validity bounds of the proposed multiscale framework requires extensive clinical testing, which was not available in this study. The proposed

model could be substantially improved by taking advantage of statistical analysis of such an extensive clinical data.

References

1. Babuska, I., *Homogenization and its application. Mathematical and computational problems.* Numerical solution of partial differential equations, 1976: p. 89-115.

2. Papanicolau, G., A. Bensoussan, and J. Lions, *Asymptotic Analysis for Periodic Structures.* 1978.

3. Sánchez-Palencia, E. *Non-homogeneous media and vibration theory*. in *Non-homogeneous media and vibration theory*. 1980.

4. Yuan, Z. and J. Fish, *Multiple scale eigendeformation-based reduced order homogenization.* Computer Methods in Applied Mechanics and Engineering, 2009. **198**(21-26): p. 2016-2038.

5. Oskay, C. and J. Fish, *Eigendeformation-based reduced order homogenization for failure analysis of heterogeneous materials.* Computer Methods in Applied Mechanics and Engineering, 2007. **196**(7): p. 1216-1243.

6. Kouznetsova, V., M.G. Geers, and W.M. Brekelmans, *Multi‐scale constitutive modelling of heterogeneous materials with a gradient‐enhanced computational homogenization scheme.* International Journal for Numerical Methods in Engineering, 2002. **54**(8): p. 1235-1260.

7. Fish, J. and K. Shek, *Multiscale analysis of composite materials and structures.* Composites Science and Technology, 2000. **60**(12–13): p. 2547-2556.

8. Fish, J. and A. Wagiman, *Multiscale finite element method for a locally nonperiodic heterogeneous medium.* Computational Mechanics, 1993. **12**(3): p. 164-180.

9. Hou, T.Y. and X.-H. Wu, *A Multiscale Finite Element Method for Elliptic Problems in Composite Materials and Porous Media.* Journal of Computational Physics, 1997. **134**(1): p. 169-189.

10. Fish, J., *Practical multiscaling*. 2013: John Wiley & Sons.

11. MDS. *Multiscale Design System*. 2015; Available from: http://multiscale.biz/.

12. Haftka, R.T. and J.L. Walsh, *Stacking-sequence optimization for buckling of laminated plates by integer programming.* AIAA journal, 1992. **30**(3): p. 814-819.

13. Le Riche, R. and R.T. Haftka, *Optimization of laminate stacking sequence for buckling load maximization by genetic algorithm.* AIAA Journal, 1993. **31**(5): p. 951-956.

14. Miki, M. and Y. Sugiyamat, *Optimum design of laminated composite plates using lamination parameters.* AIAA journal, 1993. **31**(5): p. 921-922.

15. Gürdal, Z., R.T. Haftka, and P. Hajela, *Design and optimization of laminated composite materials*. 1999: John Wiley & Sons.

16. Wu, J. and R. Burgueno, *An integrated approach to shape and laminate stacking sequence optimization of free-form FRP shells.* Computer Methods in Applied Mechanics and Engineering, 2006. **195**(33-36): p. 4106-4123.

17. Omkar, S.N., et al., *Artificial Bee Colony (ABC) for multi-objective design optimization of composite structures.* Applied Soft Computing, 2011. **11**(1): p. 489-499.

18. Sebaey, T.A., et al., *Ant Colony Optimization for dispersed laminated composite panels under biaxial loading.* Composite Structures, 2011. **94**(1): p. 31-36.

19. Bendsoe, M.P., *Optimization of structural topology, shape, and material*. 2013: Springer Science & Business Media.

20. Sigmund, O. and S. Torquato. *Design of materials with extreme thermal expansion using a three-phase topology optimization method*. in *Smart Structures and Materials' 97*. 1997. International Society for Optics and Photonics.

21. Eschenauer, H.A. and N. Olhoff, *Topology optimization of continuum structures: A review*.* Applied Mechanics Reviews, 2001. **54**(4): p. 331-390.

22. Duysinx, P. and M.P. Bendsøe, *Topology optimization of continuum structures with local stress constraints.* International journal for numerical methods in engineering, 1998. **43**(8): p. 1453-1478.

23. Sigmund, O. and S. Torquato, *Design of smart composite materials using topology optimization.* Smart Materials and Structures, 1999. **8**(3): p. 365.

24. Bendsøe, M.P. and O. Sigmund, *Material interpolation schemes in topology optimization.* Archive of applied mechanics, 1999. **69**(9-10): p. 635-654.

25. Danfelt, E.L., S.A. Hewes, and T.-W. Chou, *Optimization of composite flywheel design.* International Journal of Mechanical Sciences, 1977. **19**(2): p. 69-78.

26. Saravanos, D.A. and C. Chamis, *Multiobjective shape and material optimization of composite structures including damping.* AIAA journal, 1992. **30**(3): p. 805-813.

27. Pai, N., A. Kaw, and M. Weng, *Optimization of laminate stacking sequence for failure load maximization using Tabu search.* Composites Part B: Engineering, 2003. **34**(4): p. 405-413.

28. Lund, E., *Buckling topology optimization of laminated multi-material composite shell structures.* Composite Structures, 2009. **91**(2): p. 158-167.

29. Lund, E. and J. Stegmann, *On structural optimization of composite shell structures using a discrete constitutive parametrization.* Wind Energy, 2005. **8**(1): p. 109-124.

30. Aymerich, F. and M. Serra, *Optimization of laminate stacking sequence for maximum buckling load using the ant colony optimization (ACO) metaheuristic.* Composites Part A: Applied Science and Manufacturing, 2008. **39**(2): p. 262-272.

31. Maier, H.R., et al., *Ant colony optimization distribution for design of water systems.* Journal of Water Resources Planning and Management-Asce, 2003. **129**(3): p. 200-209.

32. Parpinelli, R.S., H.S. Lopes, and A. Freitas, *Data mining with an ant colony optimization algorithm.* Evolutionary Computation, IEEE Transactions on, 2002. **6**(4): p. 321-332.

33. Merkle, D., M. Middendorf, and H. Schmeck, *Ant colony optimization for resource-constrained project scheduling.* Evolutionary Computation, IEEE Transactions on, 2002. **6**(4): p. 333-346.

34. Liang, Y.-C. and A.E. Smith, *An ant colony optimization algorithm for the redundancy allocation problem (RAP).* Reliability, IEEE Transactions on, 2004. **53**(3): p. 417-423.

35. Di Caro, G., *Ant Colony Optimization and its application to adaptive routing in telecommunication networks*. 2004, PhD thesis, Faculté des Sciences Appliquées, Université Libre de Bruxelles, Brussels, Belgium.

36. Camp, C.V. and B.J. Bichon, *Design of space trusses using ant colony optimization.* Journal of Structural Engineering, 2004. **130**(5): p. 741-751.

37. Abbaspour, K., R. Schulin, and M.T. Van Genuchten, *Estimating unsaturated soil hydraulic parameters using ant colony optimization.* Advances in water resources, 2001. **24**(8): p. 827-841.

38. Tian, J., W. Yu, and S. Xie. *An ant colony optimization algorithm for image edge detection*. in *Evolutionary Computation, 2008. CEC 2008.(IEEE World Congress on Computational Intelligence). IEEE Congress on*. 2008. IEEE.

39. Kim, D.H., A. Abraham, and J.H. Cho, *A hybrid genetic algorithm and bacterial foraging approach for global optimization.* Information Sciences, 2007. **177**(18): p. 3918-3937.

40. Plevris, V. and M. Papadrakakis, *A Hybrid Particle Swarm-Gradient Algorithm for Global Structural Optimization.* Computer-Aided Civil and Infrastructure Engineering, 2010.

41. Xia, W. and Z. Wu, *An effective hybrid optimization approach for multi-objective flexible job-shop scheduling problems.* Computers & Industrial Engineering, 2005. **48**(2): p. 409-425.

42. Wang, L. and D.-Z. Zheng, *An effective hybrid optimization strategy for job-shop scheduling problems.* Computers & Operations Research, 2001. **28**(6): p. 585-596.

43. Vicini, A. and D. Quagliarella, *Airfoil and wing design through hybrid optimization strategies.* AIAA journal, 1999. **37**(5): p. 634-641.

44. Zahara, E., S.-K.S. Fan, and D.-M. Tsai, *Optimal multi-thresholding using a hybrid optimization approach.* Pattern Recognition Letters, 2005. **26**(8): p. 1082-1095.

45. Chaparro, B., et al., *Material parameters identification: Gradient-based, genetic and hybrid optimization algorithms.* Computational Materials Science, 2008. **44**(2): p. 339-346.

46. Okamoto, M., et al., *Nonlinear numerical optimization with use of a hybrid genetic algorithm incorporating the modified Powell method.* Applied Mathematics and Computation, 1998. **91**(1): p. 63-72.

47. Crain, T., et al., *Interplanetary flyby mission optimization using a hybrid global-local search method.* Journal of Spacecraft and Rockets, 2000. **37**(4): p. 468-474.

48. Lin, C.-C. and Y.-J. Lee, *Stacking sequence optimization of laminated composite structures using genetic algorithm with local improvement.* Composite structures, 2004. **63**(3): p. 339-345.

49. Kim, C., et al., *Stacking sequence optimization of laminated plates.* Composite Structures, 1997. **39**(3): p. 283-288.

50. Matsuzaki, R. and A. Todoroki, *Stacking-sequence optimization using fractal branch-and-bound method for unsymmetrical laminates.* Composite Structures, 2007. **78**(4): p. 537-550.

51. Park, J., et al., *Stacking sequence design of composite laminates for maximum strength using genetic algorithms.* Composite Structures, 2001. **52**(2): p. 217-231.

52. Soremekun, G., et al., *Stacking sequence blending of multiple composite laminates using genetic algorithms.* Composite Structures, 2002. **56**(1): p. 53-62.

53. Ghiasi, H., et al., *Optimum stacking sequence design of composite materials Part II: Variable stiffness design.* Composite Structures, 2010. **93**(1): p. 1-13.

54. Bruyneel, M., et al., *Stacking sequence optimization for constant stiffness laminates based on a continuous optimization approach.* Structural and Multidisciplinary Optimization, 2012. **46**(6): p. 783-794.

55. Bendsøe, M.P., *Optimal shape design as a material distribution problem.* Structural optimization, 1989. **1**(4): p. 193-202.

56. Der Kiureghian, A. and J.-B. Ke, *The stochastic finite element method in structural reliability.* Probabilistic Engineering Mechanics, 1988. **3**(2): p. 83-91.

57. Shinozuka, M. and G. Deodatis, *Response variability of stochastic finite element systems.* Journal of Engineering Mechanics, 1988. **114**(3): p. 499-519.

58. Yamazaki, F., et al., *Neumann expansion for stochastic finite element analysis.* Journal of Engineering Mechanics, 1988. **114**(8): p. 1335-1354.

59. Haldar, A. and S. Mahadevan, *Reliability assessment using stochastic finite element analysis*. 2000: John Wiley & Sons.

60. Ghanem, R.G. and P.D. Spanos, *Stochastic finite elements: a spectral approach*. 2003: Courier Corporation.

61. Stefanou, G., *The stochastic finite element method: past, present and future.* Computer Methods in Applied Mechanics and Engineering, 2009. **198**(9): p. 1031-1051.

62. Ghanem, R.G. and P.D. Spanos, *Spectral stochastic finite-element formulation for reliability analysis.* Journal of Engineering Mechanics, 1991. **117**(10): p. 2351-2372.

63. Di Sciuva, M. and D. Lomario, *A comparison between Monte Carlo and FORMs in calculating the reliability of a composite structure.* Composite Structures, 2003. **59**(1): p. 155-162.

64. Der Kiureghian, A., H.-Z. Lin, and S.-J. Hwang, *Second-order reliability approximations.* Journal of Engineering Mechanics, 1987. **113**(8): p. 1208-1225.

65. Hohenbichler, M. and R. Rackwitz, *Improvement of second-order reliability estimates by importance sampling.* Journal of Engineering Mechanics, 1988. **114**(12): p. 2195-2199.

66. Kamiński, M. and M. Kleiber, *Perturbation based stochastic finite element method for homogenization of two-phase elastic composites.* Computers & Structures, 2000. **78**(6): p. 811-826.

67. Kaminski, M., *The stochastic perturbation method for computational mechanics*. 2013: John Wiley & Sons.

68. Hiriyur, B., H. Waisman, and G. Deodatis, *Uncertainty quantification in homogenization of heterogeneous microstructures modeled by XFEM.* International Journal for Numerical Methods in Engineering, 2011. **88**(3): p. 257-278.

69. Dwaikat, M.M.S., C. Spitas, and V. Spitas, *Effect of the stochastic nature of the constituents parameters on the predictability of the elastic properties of fibrous nano-composites.* Composites Science and Technology, 2012. **72**(15): p. 1882-1891.

70. Sriramula, S. and M.K. Chryssanthopoulos, *Quantification of uncertainty modelling in stochastic analysis of FRP composites.* Composites Part a-Applied Science and Manufacturing, 2009. **40**(11): p. 1673-1684.

71. Sakata, S.-i., F. Ashida, and K. Enya, *Stochastic Analysis of Microscopic Stress in Fiber Reinforced Composites Considering Uncertainty in a Microscopic Elastic Property.* Journal of Solid Mechanics and Materials Engineering, 2010. **4**(5): p. 568-577.

72. Chamis, C.C., *Probabilistic simulation of multi-scale composite behavior.* Theoretical and Applied Fracture Mechanics, 2004. **41**(1–3): p. 51-61.

73. Tootkaboni, M. and L. Graham‐Brady, *A multi‐scale spectral stochastic method for homogenization of multi‐phase periodic composites with random material properties.* International journal for numerical methods in engineering, 2010. **83**(1): p. 59-90.

74. Chen, N.-Z. and C. Guedes Soares, *Spectral stochastic finite element analysis for laminated composite plates.* Computer Methods in Applied Mechanics and Engineering, 2008. **197**(51–52): p. 4830-4839.

75. Fish, J. and W. Wu, *A nonintrusive stochastic multiscale solver.* International Journal for Numerical Methods in Engineering, 2011. **88**(9): p. 862-879.

76. Gerstner, T. and M. Griebel, *Numerical integration using sparse grids*. Numerical algorithms, 1998. **18**(3-4): p. 209-232.

77. Yuan, Z. and J. Fish, *Hierarchical model reduction at multiple scales.* International Journal for Numerical Methods in Engineering, 2009. **79**(3): p. 314-339.

78. Yuan, Z. and J. Fish, *Multiple scale eigendeformation-based reduced order homogenization.* Computer Methods in Applied Mechanics and Engineering, 2009. **198**(21–26): p. 2016-2038.

79. Sakata, S.-i., F. Ashida, and Y. Shimizu, *Inverse stochastic homogenization analysis for a particle-reinforced composite material with the Monte Carlo simulation.* International Journal for Multiscale Computational Engineering, 2011. **9**(4).

80. Bogdanor, M.J., C. Oskay, and S.B. Clay, *Multiscale modeling of failure in composites under model parameter uncertainty.* Computational Mechanics, 2015. **56**(3): p. 389-404.

81. Bogdanor, M.J., S. Mahadevan, and C. Oskay, *UNCERTAINTY QUANTIFICATION IN DAMAGE MODELING OF HETEROGENEOUS MATERIALS.* 2013. **11**(3): p. 289-307.

82. Crouch, R.D., S.B. Clay, and C. Oskay, *Experimental and computational investigation of progressive damage accumulation in CFRP composites.* Composites Part B: Engineering, 2013. **48**: p. 59-67.

83. Liu, Y., W. Sun, and J. Fish, *Determining Material Parameters for Critical State Plasticity Models Based on Multilevel Extended Digital Database.* Journal of Applied Mechanics, 2015. **83**(1): p. 011003-011003.

84. Breidt, J., T. Butler, and D. Estep, *A Measure-Theoretic Computational Method for Inverse Sensitivity Problems I: Method and Analysis.* Siam Journal on Numerical Analysis, 2011. **49**(5): p. 1836-1859.

85. Butler, T., D. Estep, and J. Sandelin, *A Computational Measure Theoretic Approach to Inverse Sensitivity Problems Ii: A Posteriori Error Analysis.* Siam Journal on Numerical Analysis, 2012. **50**(1): p. 22-45.

86. Wyss, G.D. and K.H. Jorgensen, *A user's guide to LHS: Sandia's Latin hypercube sampling software.* 1997.

87. Hu, N. and J. Fish, *Enhanced ant colony optimization for multiscale problems.* Comput. Mech., 2016. **57**(3): p. 447-463.

88. Tomblin, J., et al., *A-Basis and B-Basis Design Allowables for Epoxy–Based Prepreg TORAY T700GC-12K-31E/# 2510 Unidirectional Tape [US Units]*. 2002, Wichita, KS: National Institute for Aviation Research.

89. Fuller, G.F., *Falls in the elderly.* American family physician, 2000. **61**(7): p. 2159-68, 2173-4.

90. Melton 3rd, L. and S. Cummings, *Heterogeneity of age-related fractures: implications for epidemiology.* Bone and mineral, 1987. **2**(4): p. 321-331.

91. Cummings, S.R. and L.J. Melton, *Epidemiology and outcomes of osteoporotic fractures.* The Lancet, 2002. **359**(9319): p. 1761-1767.

92. Hamed, E., Y. Lee, and I. Jasiuk, *Multiscale modeling of elastic properties of cortical bone.* Acta Mechanica, 2010. **213**(1-2): p. 131-154.

93. Taya, M. and T.-W. Chou, *On two kinds of ellipsoidal inhomogeneities in an infinite elastic body: an application to a hybrid composite.* International Journal of Solids and Structures, 1981. **17**(6): p. 553-563.

94. Keyak, J.H., et al., *Automated 3-Dimensional Finite-Element Modeling of Bone - a New Method.* Journal of Biomedical Engineering, 1990. **12**(5): p. 389-397.

95. Martelli, S., et al., *Accuracy of subject specific finite-element models of long bones from CT data: an in vitro study.* Proc. ICCB II, 2005. **1**: p. 251-265.

96. Trabelsi, N., Z. Yosibash, and C. Milgrom, *Validation of subject-specific automated p-FE analysis of the proximal femur.* Journal of biomechanics, 2009. **42**(3): p. 234-241.

97. Rossman, T., V. Kushvaha, and D. Dragomir-Daescu, *QCT/FEA predictions of femoral stiffness are strongly affected by boundary condition modeling.* Computer methods in biomechanics and biomedical engineering, 2016. **19**(2): p. 208-216.

98. Dawson-Hughes, B., et al., *Clinician's guide to prevention and treatment of osteoporosis.* National Osteoporosis Foundation, Washington DC, 2008.

99. Dalle Carbonare, L. and S. Giannini, *Bone microarchitecture as an important determinant of bone strength.* Journal of endocrinological investigation, 2004. **27**(1): p. 99-105.

100. Genant, H., et al., *Advanced imaging of bone macro and micro structure.* Bone, 1999. **25**(1): p. 149-152.

101. Bettamer, A., et al., *Using visual image measurements to validate a novel finite element model of crack propagation and fracture patterns of proximal femur.* Computer Methods in Biomechanics and Biomedical Engineering: Imaging & Visualization, 2015: p. 1-12.

102. Niebur, G.L., et al., *High-resolution finite element models with tissue strength asymmetry accurately predict failure of trabecular bone.* Journal of biomechanics, 2000. **33**(12): p. 1575-1583.

103. Nawathe, S., et al., *Microstructural failure mechanisms in the human proximal femur for sideways fall loading.* Journal of bone and mineral research, 2014. **29**(2): p. 507-515.

104. Nawathe, S., F. Juillard, and T.M. Keaveny, *Theoretical bounds for the influence of tissue-level ductility on the apparent-level strength of human trabecular bone.* Journal of biomechanics, 2013. **46**(7): p. 1293-1299.

105. Bessho, M., et al., *Prediction of proximal femur strength using a CT-based nonlinear finite element method: differences in predicted fracture load and site with changing load and boundary conditions.* Bone, 2009. **45**(2): p. 226-231.

106. Keyak, J., *Improved prediction of proximal femoral fracture load using nonlinear finite element models.* Medical engineering & physics, 2001. **23**(3): p. 165-173.

107. Den Buijs, J.O. and D. Dragomir-Daescu, *Validated finite element models of the proximal femur using two-dimensional projected geometry and bone density.* Computer methods and programs in biomedicine, 2011. **104**(2): p. 168-174.

108. Dragomir-Daescu, D., et al., *Robust QCT/FEA models of proximal femur stiffness and fracture load during a sideways fall on the hip.* Annals of biomedical engineering, 2011. **39**(2): p. 742-755.

109. Materialise. *Materialise Mimics*. 2016; Available from: http://biomedical.materialise.com/mimics.

110. Synopsys, I., *Simpleware.* 2016.

111. Computing, N.N.C.f.I.B., *Seg3D.* 2016.

112. Computing, N.N.C.f.I.B., *Cleaver - A MultiMaterial Tetrahedral Meshing Library and Application.* 2016.

113. Doblaré, M., J.M. García, and M.J. Gómez, *Modelling bone tissue fracture and healing: a review.* Engineering Fracture Mechanics, 2004. **71**(13–14): p. 1809-1840.

114. Vashishth, D., *Hierarchy of bone microdamage at multiple length scales.* International journal of fatigue, 2007. **29**(6): p. 1024-1033.

115. Jang, I.G. and I.Y. Kim, *Computational simulation of simultaneous cortical and trabecular bone change in human proximal femur during bone remodeling.* Journal of Biomechanics, 2010. **43**(2): p. 294-301.

116. Hambli, R., H. Katerchi, and C.-L. Benhamou, *Multiscale methodology for bone remodelling simulation using coupled finite element and neural network computation.* Biomechanics and Modeling in Mechanobiology, 2011. **10**(1): p. 133-145.

117. Fish, J., et al., *Computational plasticity for composite structures based on mathematical homogenization: Theory and practice.* Computer Methods in Applied Mechanics and Engineering, 1997. **148**(1): p. 53-73.

118. Fish, J., Q. Yu, and K. Shek, *Computational damage mechanics for composite materials based on mathematical homogenization.* International journal for numerical methods in engineering, 1999. **45**(11): p. 1657-1679.

119. Jacob Fish, Z.Y., *N-Scale Model Reduction Theory*, in *Multiscale Methods: Bridging the Scales in Science and Engineering*. 2009, Oxford University Press.

120. Mulvihill, B.M. and P.J. Prendergast, *Mechanobiological regulation of the remodelling cycle in trabecular bone and possible biomechanical pathways for osteoporosis.* Clinical Biomechanics, 2010. **25**(5): p. 491-498.

121. Martin, R., *Toward a unifying theory of bone remodeling.* Bone, 2000. **26**(1): p. 1-6.

122. Ciarelli, T., et al., *Variations in three‐dimensional cancellous bone architecture of the proximal femur in female hip fractures and in controls.* Journal of Bone and Mineral Research, 2000. **15**(1): p. 32-40.

123. Kennedy, J., *Particle swarm optimization*, in *Encyclopedia of machine learning*. 2011, Springer. p. 760-766.

124. Karaboga, D. and B. Basturk, *A powerful and efficient algorithm for numerical function optimization: artificial bee colony (ABC) algorithm.* Journal of global optimization, 2007. **39**(3): p. 459-471.

125. Bonabeau, E., M. Dorigo, and G. Theraulaz, *Swarm intelligence: from natural to artificial systems*. 1999: Oxford university press.

126. Dorigo, M., *Optimization, Learning and Natural Algorithms.* Ph.D. Thesis, Politecnico di Milano, Italy, 1992.

127. Dorigo, M. and L.M. Gambardella, *Ant colonies for the travelling salesman problem.* Biosystems, 1997. **43**(2): p. 73-81.

128. Dorigo, M. and T. Stutzle, *The Ant Colony Optimization Metaheuristic.* Ant Colony Optimization, 2004: p. 25-64.

129. Socha, K. and M. Dorigo, *Ant colony optimization for continuous domains.* European journal of operational research, 2008. **185**(3): p. 1155-1173.

130. Socha, K., *ACO for continuous and mixed-variable optimization*, in *Ant colony optimization and swarm intelligence*. 2004, Springer. p. 25-36.

131. Schlüter, M., J.A. Egea, and J.R. Banga, *Extended ant colony optimization for non-convex mixed integer nonlinear programming.* Computers & Operations Research, 2009. **36**(7): p. 2217-2229.

132. Blum, C., *Ant colony optimization: Introduction and recent trends.* Physics of Life reviews, 2005. **2**(4): p. 353-373.

133. Dorigo, M., *Ant Colony Optimization and Swarm Intelligence: 5th International Workshop, ANTS 2006, Brussels, Belgium, September 4-7, 2006, Proceedings*. Vol. 4150. 2006: Springer Science & Business Media.

134. Stützle, T. and H.H. Hoos, *MAX–MIN ant system.* Future generation computer systems, 2000. **16**(8): p. 889-914.

135. Stützle, T.G., *Local search algorithms for combinatorial problems: analysis, improvements, and new applications*. Vol. 220. 1999: Infix Sankt Augustin, Germany.

136. Stutzle, T. and H. Hoos, *MAX-MIN Ant System and local search for the traveling salesman problem.* Proceedings of 1997 Ieee International Conference on Evolutionary Computation (Icec '97), 1997: p. 309-314.

137. Stutzle, T. and H. Hoos. *MAX-MIN Ant System and local search for the traveling salesman problem.* in *Evolutionary Computation, 1997., IEEE International Conference on*. 1997.

138. Plevris, V. and M. Papadrakakis, *A hybrid particle swarm—gradient algorithm for global structural optimization.* Computer‐Aided Civil and Infrastructure Engineering, 2011. **26**(1): p. 48-68.

139. Renders, J.-M. and S.P. Flasse, *Hybrid methods using genetic algorithms for global optimization.* Systems, Man, and Cybernetics, Part B: Cybernetics, IEEE Transactions on, 1996. **26**(2): p. 243-258.

140. Zhang, J.-R., et al., *A hybrid particle swarm optimization–back-propagation algorithm for feedforward neural network training.* Applied Mathematics and Computation, 2007. **185**(2): p. 1026-1037.

141. Gambardella, M., M.B.A. Martinoli, and R.P.T. Stützle. *Ant Colony Optimization and Swarm Intelligence*. in *5th International Workshop*. 2006. Springer.

142. Hajimirsadeghi, G.H., M. Nabaee, and B. Araabi, *Ant Colony Optimization with a Genetic Restart Approach toward Global Optimization*, in *Advances in Computer Science and Engineering*, H. Sarbazi-Azad, et al., Editors. 2009, Springer Berlin Heidelberg. p. 9-16.

143. Torquato, S., T.M. Truskett, and P.G. Debenedetti, *Is random close packing of spheres well defined?* Physical review letters, 2000. **84**(10): p. 2064.

144. Shimada, K. and D.C. Gossard, *Bubble mesh: automated triangular meshing of non-manifold geometry by sphere packing*, in *Proceedings of the third ACM symposium on Solid modeling and applications*. 1995, ACM: Salt Lake City, Utah, USA. p. 409-419.

145. Li, X.Y., S.H. Teng, and A. Üngör, *Biting: Advancing front meets sphere packing.* International Journal for Numerical Methods in Engineering, 2000. **49**(1 - 2): p. 61-81.

146. Haftka, R.T. and Z. Gürdal, *Elements of structural optimization*. Vol. 11. 2012: Springer Science & Business Media.

147. McKay, M.D., R.J. Beckman, and W.J. Conover, *A comparison of three methods for selecting values of input variables in the analysis of output from a computer code.* Technometrics, 2000. **42**(1): p. 55-61.

148. Eglajs, V.A.P., *New approach to the design of multifactor experiments.* Problems of Dynamics and Strengths, 1977. **2**: p. 104-107.

149. Iman, R.L., J. Campbell, and J. Helton, *An approach to sensitivity analysis of computer models. I- Introduction, input, variable selection and preliminary variable assessment.* Journal of quality technology, 1981. **13**: p. 174-183.

150. Rubinstein, R.Y. and D.P. Kroese, *Simulation and the Monte Carlo method*. Vol. 707. 2011: John Wiley & Sons.

151. Adams, B.M., et al., *Dakota, a multilevel parallel object-oriented framework for design optimization, parameter estimation, uncertainty quantification, and sensitivity analysis: Version 5.0 user's manual.* Sandia National Laboratories, Tech. Rep. SAND2010-2183, 2009.

152. Helton, J.C. and F.J. Davis, *Latin hypercube sampling and the propagation of uncertainty in analyses of complex systems.* Reliability Engineering & System Safety, 2003. **81**(1): p. 23-69.

153. Ma, X. and N. Zabaras, *An adaptive hierarchical sparse grid collocation algorithm for the solution of stochastic differential equations.* Journal of Computational Physics, 2009. **228**(8): p. 3084-3113.

154. TORAY CARBON FIBERS AMERICA, I., *TORAYCA T700S DATA SHEET*. 2015.

155. Liu, Y., et al., *A regularized phenomenological multiscale damage model.* International Journal for Numerical Methods in Engineering, 2014. **99**(12): p. 867-887.

156. Yuan, Z. and J. Fish, *Nonlinear multiphysics finite element code architecture in object oriented Fortran environment.* Finite Elements in Analysis and Design, 2015. **99**: p. 1-15.

157. Altair. *Multiscale Designer*. 2016; Available from: http://www.altairhyperworks.com/product/Multiscale-Designer.

158. Zifeng Yuan, J.F., *Are the cohesive zone models necessary for delamination analysis?* 2016, Columbia University.

159. Jonvaux, J., T. Hoc, and É. Budyn, *Analysis of micro fracture in human Haversian cortical bone under compression.* International journal for numerical methods in biomedical engineering, 2012. **28**(9): p. 974-998.

160. Ural, A. and S. Mischinski, *Multiscale modeling of bone fracture using cohesive finite elements.* Engineering Fracture Mechanics, 2013. **103**: p. 141-152.

161. Liao, S.-H., R.-F. Tong, and J.-X. Dong, *Anisotropic finite element modeling for patient-specific mandible*. computer methods and programs in biomedicine, 2007. **88**(3): p. 197-209.

162. Wolff, J., *The Law of Bone Remodeling*. 1892 ed. 1986, Berlin: Springer.

163. Heřt, J., P. Fiala, and M. Petrtýl, *Osteon orientation of the diaphysis of the long bones in man.* Bone, 1994. **15**(3): p. 269-277.

164. Lotz, J.C., T.N. Gerhart, and W.C. Hayes, *Mechanical properties of metaphyseal bone in the proximal femur.* Journal of biomechanics, 1991. **24**(5): p. 317327-325329.

165. Keyak, J.H. and Y. Falkinstein, *Comparison of in situ and in vitro CT scan-based finite element model predictions of proximal femoral fracture load.* Medical engineering & physics, 2003. **25**(9): p. 781-787.

166. Doblaré, M., J. Garcıa, and M. Gómez, *Modelling bone tissue fracture and healing: a review*. Engineering Fracture Mechanics, 2004. **71**(13): p. 1809-1840.

167. Trabelsi, N. and Z. Yosibash, *Patient-specific finite-element analyses of the proximal femur with orthotropic material properties validated by experiments*. Journal of biomechanical engineering, 2011. **133**(6): p. 061001.

168. Liu, X.S., et al., *Complete volumetric decomposition of individual trabecular plates and rods and its morphological correlations with anisotropic elastic moduli in human trabecular bone.* Journal of Bone and Mineral Research, 2008. **23**(2): p. 223-235.

169. Rho, J.-Y., T.Y. Tsui, and G.M. Pharr, *Elastic properties of human cortical and trabecular lamellar bone measured by nanoindentation.* Biomaterials, 1997. **18**(20): p. 1325-1330.

170. Budyn, E., T. Hoc, and J. Jonvaux, *Fracture strength assessment and aging signs detection in human cortical bone using an X-FEM multiple scale approach.* Computational Mechanics, 2008. **42**(4): p. 579-591.

171. Hogan, H.A., *Micromechanics modeling of Haversian cortical bone properties.* Journal of Biomechanics, 1992. **25**(5): p. 549-556.

172. Sabelman, E., et al. *Collagen/hyaluronic acid matrices for connective tissue repair*. in *First Smith and Nephew international Symposium: Advances in Tissues Engineering and Biomaterials*. 1997.

173. Hambli, R., *Micro-CT finite element model and experimental validation of trabecular bone damage and fracture.* Bone, 2013. **56**(2): p. 363-374.

174. O'Flaherty, E.J., *Modeling normal aging bone loss, with consideration of bone loss in osteoporosis.* Toxicological Sciences, 2000. **55**(1): p. 171-188.

175. Dragomir-Daescu, D., et al., *Robust QCT/FEA Models of Proximal Femur Stiffness and Fracture Load During a Sideways Fall on the Hip.* Annals of Biomedical Engineering, 2011. **39**(2): p. 742-755.

176. Kinzl, M., U. Wolfram, and D. Pahr, *Identification of a crushable foam material model and application to strength and damage prediction of human femur and vertebral body.* Journal of the mechanical behavior of biomedical materials, 2013. **26**: p. 136-147.

177. Martin-Brownlie, D.J. *Hip Joint Pain That Is From A Fracture...* Available from: http://www.drjoexplains.com/

178. Graham, L. and G. Deodatis, *Response and eigenvalue analysis of stochastic finite element systems with multiple correlated material and geometric properties.* Probabilistic Engineering Mechanics, 2001. **16**(1): p. 11-29.